

Finite deformation hyperplasticity theory for crushable, cemented granular materials

Kateryna Oliynyk^a & Claudio Tamagnini^a

^a Department of Civil and Environmental Engineering, University of Perugia, Italy.

Published

16th November 2020

<https://doi.org/10.5802/ogeo.8>

Edited by

Benjy Marks
School of Civil Engineering
The University of Sydney
Australia

Reviewed by

Arghya Das
Department of Civil Engineering
Indian Institute of Technology Kanpur
India

One anonymous reviewer

Correspondence

Kateryna Oliynyk & Claudio Tamagnini
University of Perugia
Dept. of Civil and Env. Engng.
via G. Duranti, 93 – 06125 Perugia
Italy
kateryna.olinyk@icloud.com



This article is licensed under the Creative Commons Attribution NonCommercial ShareAlike 4.0 License.



Open Geomechanics is member of the Centre Mersenne for Open Scientific Publishing

Abstract.

The work is focused on the formulation of a thermodynamically-based constitutive theory for granular, cemented geomaterials, often characterized by an open structure with high porosity and voids of large diameter. Upon mechanical degradation processes such as bond rupture and grain crushing, these material undergo large volumetric and shear strains, and in some cases the deformations are so large that the usual assumption of linearized kinematics may be not applicable. In the first part of this work, the theory of hyperplasticity is extended to the finite deformation regime by adopting a multiplicative split of the deformation gradient into an elastic and a plastic part, under the assumption of material isotropy. Grain breakage and bond damage processes are accounted for through two micromechanically-inspired internal variables. A specific constitutive model for carbonatic cemented sands and calcarenites is proposed as a relevant example of application. In the second part, an implicit stress-point algorithm has been developed which is amenable to closed form linearization, for the implementation of the model into standard FE platforms. A series of numerical tests have demonstrated the accuracy and efficiency of the proposed algorithm. The simulation of plane strain biaxial tests, modeled as boundary-value problems, has highlighted the role played by geometric non-linearity in determining the evolution of the specimen deformation upon reaching a bifurcation condition.

Keywords. Hard soils, Soft rocks, Hyperplasticity, Breakage mechanics, Finite deformations, Multiplicative plasticity, Stress-point algorithm, Consistent linearization

1. Introduction

Since the early '90s a significant body of experimental and theoretical research activities has been addressed to the study of natural geomaterials – typically classified as hard soils–soft rocks (HSSR) – which are characterized by a rock–like mechanical behavior at low stress levels, and a soil–like response at medium to high stress levels.

These studies have been motivated by the need of obtaining a better understanding of the mechanical response of such materials as observed in a number of practical applications, such as the evaluation of pile bearing capacity of offshore platforms [McLelland, 1988, King and Lodge, 1988, Jardine et al., 2018], the subsidence phenomena associated to hydrocarbon extraction [Potts et al., 1988], the evaluation of the stability conditions of underground excavations and sub–vertical cuts in open pit quarries [Evangelista et al., 2000, Bianchi Fasani et al., 2011].

In particular, a number of experimental studies have been conducted on two classes of commonly found HSSR deposits, namely: natural cemented carbonatic sands and calcarenites [see, e.g. Uriel and Serrano, 1975, Airey, 1993, Coop and Atkinson, 1993, Lagioia and Nova, 1995, Cuccovillo and Coop, 1999], and pyroclastic deposits of tuffs and lapillistone, known in Italy with the local name of “pozzolana” stone [Aversa and Evangelista, 1998, Cecconi and Viggiani, 2001].

Notwithstanding the large differences in the mineralogical composition of the constituents of those deposits, they presents a number of common features, such as: a high initial porosity and void ratio; high compressibility after yield under isotropic or oedometric compression; frictional behavior under shear, with typically high values of the friction angle; fragile and mildly dilatant response under deviatoric loading at low stress levels; ductile and strongly contractant behavior in shear at medium to high stress levels, with peak strength attained at large to very large strain levels, often greater than 20%.

The reasons for such peculiar behavior is to be found in the particular microstructure of such materials, characterized by the presence relatively weak grains (made of calcite or amorphous silica) and of intergranular bonds of various origin, which allow the solid skeleton to be stable with a relatively large porosity, and impart to the material a higher stiffness and strength than the corresponding unbonded granular soil. Depending on the stress levels, a mechanical loading process can produce a progressive degradation of intergranular bonds and crushing of the individual grains, which can occur even at relatively moderate stress levels. Evidences of grain crushing in those materials have been reported, among others, by Coop [1990] and Cecconi and Viggiani [2001].

Constitutive modeling of cemented granular materials undergoing mechanical degradation processes has been addressed mainly within the framework of the theory of hardening plasticity. Starting from the pioneering works of Nova [1992], a number of works incorporate in the plasticity formulation some suitable “bonding–related” internal variables, monotonously decaying with the accumulation

of plastic deformations in order to deal with the effects of intergranular bond rupture [see, e.g. Gens and Nova, 1993, Kavvadas, 1994, Lagioia and Nova, 1995, Rouainia and Wood, 2000, Liu and Carter, 2002, Tamagnini et al., 2002, Nova et al., 2003, Ciantia and di Prisco, 2016, Tamagnini and Ciantia, 2016].

The description of the effects of grain crushing from a purely phenomenological point of view has been attempted by Cecconi et al. [2002] and DeSimone and Tamagnini [2005], who linked the effects of grain crushing to the decay of the critical friction angle of the material. In DeSimone and Tamagnini [2005], the formulation of the elastoplastic model has been derived from the principles of thermomechanics of continuous media, starting from available experimental stress–dilatancy data. More recently, Kikumoto et al. [2010] proposed a modification of the Severn–Trent model [Gajo and Wood, 1999] by incorporating a dependence of the critical state line in $e:p$ space and of the crushing yield surface in stress space on a scalar *grading state index*, the evolution of which is controlled by plastic volumetric strains.

A significant progress in the understanding and modeling of the effects of grain breakage on the behavior of uncemented granular materials has been provided by the theory of *breakage mechanics* proposed by Einav [2007a, 2007b]. In this approach, the macroscopic evolution equations for the material are derived from thermodynamics principles, starting from two potentials, the free energy function and the dissipation function. The key point is that the effects of grain crushing are related to the changes of a micromechanically–inspired internal variable derived from the microscale via statistical homogenization. Later, Tengattini et al. [2014] and Das et al. [2014] extended the principles of breakage mechanics to cemented granular soils, incorporating a second micromechanical internal variable accounting for bond damage, see Sect. 2.1 for details. It is worth noting that, while the internal variables in question are amenable to direct measurement from micromechanical data, the plasticity models developed within the framework of breakage mechanics cannot be considered true multiscale models such as those developed from upscaling procedures of various kind, see for example the monography of Fish [2014].

All the aforementioned constitutive models have been developed under the assumption of linearized kinematics. However, given the high deformability showed by cemented soils with crushable grains under medium to high stress levels, geometric non–linearity may play an important role in some practical applications such as the modeling of offshore foundations, piled foundations and underground excavations. Furthermore, the accurate modeling of strain localization processes, either in the form of shear or compaction bands, as well as of the post–localization behavior of geotechnical structures may require finite deformation kinematics. For these reasons, Rubin and Einav [2011] have derived a large deformation version of the breakage model for granular materials and, more recently, Monforte et al. [2019] have extended to finite deformations a Modified Cam–Clay model for bonded granular materials, capable of dealing with the pathological mesh sensitivity typically

observed in presence of strain localization effects by means of a non–local formulation of the hardening laws.

The first objective of this work, is to extend the thermodynamically–based approach of the theory of hyperplasticity – as defined by Houlsby and Puzrin [2007] – to the finite deformation regime by adopting a multiplicative split of the deformation gradient into an elastic and a plastic part and incorporating the concepts of breakage and damage into the constitutive functions. In the derivation of the theory, we will restrict ourselves to the case of isotropic materials, an assumption consistent with the scalar nature of the degradation–related internal variables. This choice may appear rather restrictive in some cases, but can be justified by the fact that the nature of the intergranular bonds is often characterized by a rather non–directional character, [Kavvasdas et al., 1993, Kavvasdas, 1994]. In addition, isotropy allows to keep the mathematical structure of the constitutive equations to an acceptable level of complexity in view of the practical application of this approach to advanced geotechnical engineering practice, while preserving its ability of reproducing most of the relevant features of the materials under study. A specific finite–deformation hyperplastic model for cemented sands and weak arenaceous rocks is proposed as an example of application of the general theory, starting from the works of Tengattini et al. [2014], Das et al. [2014].

In the solution of practical boundary value problems, the availability of an accurate and efficient *stress–point algorithm* for the local integration of the constitutive equations in rate–form is of primary importance. As pointed out, for example, by Hughes [1984], the integration of the constitutive equation at the local level is the central problem of computational plasticity, since in this procedure the constitutive equation plays its main role. In addition, the accuracy of the stress–point algorithm has a direct impact on the overall results of the numerical simulation.

Many different stress–point algorithms have been proposed for the finite element implementation of finite deformation plasticity models, see, e.g. , Simo and Hughes [1998] or de Souza Neto et al. [2011] for a general overview. In the second part of this work we adopt a fully implicit predictor–corrector algorithm based on the exponential mapping [Simo, 1992], previously adopted in computational geomechanics by Borja and Tamagnini [1998], Callari et al. [1998], Sanavia et al. [2002] among others. The peculiar feature of the proposed algorithm is that it is entirely formulated in the product space of elastic logarithmic principal strains and internal state variables, thus allowing to circumvent the need to express the yield function in stress space. Moreover the proposed algorithm is amenable to closed form linearization and therefore allows to fully exploit the quadratic convergence of the Newton algorithm in the global equilibrium iterations.

The outline of the paper is as follows. In Sect. 2, the degradation processes occurring in natural deposits of cemented granular materials are illustrated and the approach of breakage mechanics for obtaining the macroscopic internal variables quantifying the effects of grain breakage and bond damage is briefly summarized. As a motivation

for the subsequent developments, in the same section the small–strain formulation of the theory of hyperplasticity with internal variables is presented in general form. In Sect. 3 the infinitesimal theory is extended to the finite deformation regime adopting a multiplicative decomposition of the deformation gradient. In Sect. 4, an existing hyperplastic model for cemented granular materials with grain crushing is chosen as a suitable candidate to for the extension to finite deformations. In view of practical applications, a fully implicit stress–point algorithm is proposed for the local integration of the evolution equations. The algorithm and its consistent linearization are presented in Sects. 5 and 6, respectively. Some representative numerical simulations, both at the element and at the boundary value problem level, showing the importance of geometric non–linearity and the capabilities of the stress–point algorithm are provided in Sect. 7. Finally, some concluding remarks and suggestions for further developments are provided in Sect. 8.

Notation

In line with Terzaghi’s principle of effective stress, in the following developments all stresses and stress–related quantities are effective, unless otherwise stated. The usual sign convention of soil mechanics (compression positive) is adopted throughout. Both direct and index notations will be used to represent vector and tensor quantities according to convenience. Following standard notation, for any two vectors $\mathbf{v}, \mathbf{w} \in \mathbb{R}^3$ the dot product is defined as: $\mathbf{v} \cdot \mathbf{w} = v_i w_i$, and the dyadic product as: $[\mathbf{v} \otimes \mathbf{w}]_{ij} = v_i w_j$. For any two second–order tensors $\mathbf{X}, \mathbf{Y} \in \mathbb{L}$ we define $\mathbf{X} \cdot \mathbf{Y} = X_{ij} Y_{ij}$ and $[\mathbf{X} \otimes \mathbf{Y}]_{ijkl} = X_{ij} Y_{kl}$. The quantity $\|\mathbf{X}\| = \sqrt{\mathbf{X} \cdot \mathbf{X}}$ denotes the Euclidean norm of the second order tensor \mathbf{X} . The symbol $\nabla \mathbf{v}$ denotes the spatial gradient of the (spatial) vector field \mathbf{v} , while $\nabla^s \mathbf{v}$ represents its symmetric part. The symbol $\nabla_X \mathbf{V}$ denotes the material gradient of the (material) vector field \mathbf{V} defined on the reference configuration. The symmetric and antisymmetric parts of a second–order tensor \mathbf{A} are denoted with $\text{sym}(\mathbf{A})$ and $\text{skw}(\mathbf{A})$, respectively. When needed, any symmetric second–order tensor \mathbf{T} will be represented in its *spectral form*, given by:

$$\mathbf{T} = \sum_{A=1}^3 T_A \mathbf{n}^{(A)} \otimes \mathbf{n}^{(A)}$$

where T_A (with $A = 1, 2, 3$) are the principal values of \mathbf{T} and $\mathbf{n}^{(A)}$ the corresponding principal directions. According to standard notations [see, e.g. , Simo and Hughes, 1998], we denote the push–forward of a material vector or tensor quantity to the spatial configuration with the operator $\phi_*(\cdot)$, and the pull–back of a spatial vector or tensor quantity to the reference configuration with the operator $\phi^*(\cdot)$.

2. Fundamentals of infinitesimal hyperplasticity for crushable, cemented granular materials

2.1. Degradation processes in coarse-grained soils and weak rocks

The mechanical behavior of natural sand deposits and weak sedimentary rocks such as sandstones can be affected by both mechanical and physical degradation processes occurring at the grain scale. Among the first, we mention:

- grain fracture and crushing;
- mechanical degradation of intergranular bonds (or soil *destruction*, as sometimes this process is referred to in the geotechnical literature).

When the minerals constituting the grains and the intergranular bonds are sensitive to chemical aggression – i.e., when dissolution phenomena can occur in relatively short times, comparable to the typical lifetimes of civil engineering structures – degradation due to “weathering” may occur in the form of:

- dissolution of weak *depositional bonds* by wetting of the initially unsaturated solid skeleton;
- dissolution of strong *diagenetic bonds* formed by mineral precipitation at the intergranular contacts;
- dissolution of the grains.

see Ciantia and Hueckel [2013], Ciantia et al. [2014, 2015].

Depositional bonds are formed by a mixture of very small grains and seawater salts that precipitate into a meniscus-shaped bond when water evaporates. They are present only if the soil is non-saturated, and break when the precipitated salt is dissolved by pore water (short-term debonding). Diagenetic bonds typically originate from the precipitation of crystals (say, calcite) at the intergranular contacts due to changes in water pressure, temperature and pH, or by pressure solution of grain minerals at the intergranular contacts. Their mechanical and chemical degradation is more difficult than in the case of depositional bonds, and require significantly higher stress levels, as well as appropriate chemical composition of the pore water (long-term debonding).

All the aforementioned processes affect both the strength and the deformation behavior of the material and may induce irreversible strains associated to permanent rearrangements of the grains in the solid skeleton. In addition, grain dissolution may be responsible for chemically-induced volumetric strains [Ciantia et al., 2014, Tamagnini and Ciantia, 2016]. In this work, the attention will be focused on mechanical degradation processes only, considering the solid skeleton as fully saturated or perfectly dry.

The quantitative description of the effects of grain breakage and mechanical debonding at the macroscopic scale can be tackled on physically-based grounds by approximating, at the microscopic level, the grains as equivalent ideal spheres and the bonds as ideal cylinders of cement material, connecting the grains one another. Under those fairly standard assumptions, both degradation processes can be quantified at the microscopic level by the changes

induced on the probability density distributions of grain sizes and bond diameters by the imposed mechanical loads.

For non-cemented granular materials, this observation is the starting point of the theory of *breakage mechanics* introduced by Einav [2007a,b]. In breakage mechanics, the evolution of the probability density for each granulometric class is provided by the non-dimensional *fractional breakage* index:

$$B := \frac{P(x_g) - P_0(x_g)}{P_u(x_g) - P_0(x_g)} \quad B \in [0, 1] \quad (1)$$

where $P_0(x_g)$, $P(x_g)$ and $P_u(x_g)$ are the initial, current and ultimate probability densities associated to grains of diameter x_g , respectively.

A key point in breakage mechanics is the assumption of *fractional independence* of B : although the three functions P_0 , P and P_u depend on x_g , the index B is independent of grain diameter. This assumption has been verified by Einav [2007a]. The upscaling of soil properties from micro- to macroscale is based on the concept of *statistical homogenization*, according to which the evaluation of macroscopic properties is carried out using the probability density distribution of grain sizes as the weighting function of the averaging process.

In view of the development of a macroscopic constitutive theory for materials undergoing grain crushing, an important application of the above concept is the case in which the property in question is the Helmholtz free energy function of the particle class of size x_g : $\psi^g = \psi^g(x_g, \boldsymbol{\epsilon}^e)$. This function is considered as the product of a reference free energy depending on elastic strain, $\psi_r^g(\boldsymbol{\epsilon}^e)$ and of an *energy split* function, $f_\psi(x_g)$, assumed by Einav [2007a] to be a quadratic function of the grain size.

Statistical homogenization leads to the following macroscopic Helmholtz free energy function:

$$\psi(\boldsymbol{\epsilon}^e, B) = v_g(1 - \theta^g B)\psi_r^g(\boldsymbol{\epsilon}^e) \quad (2)$$

where v_g is the volume fractions of the grains and θ^g , known as grading index, is a material constant defined by:

$$\theta^g := 1 - \frac{\int_{x_{gm}}^{x_{gM}} x_g^2 P_u(x_g) d(x_g)}{\int_{x_{gm}}^{x_{gM}} x_g^2 P_0(x_g) d(x_g)} \quad (3)$$

see Einav [2007a,b] for details. Note that, being the free energy of the grains of size x_g defined per unit volume of grains, its macroscopic counterpart, defined per unit volume of the porous medium, must include the volume fraction of the grains as weighting factor.

In presence of intergranular bonds with given probability density distributions $P_0^b(x_b)$ (initial), $P^b(x_b)$ (current) and $P_u^b(x_b)$ (ultimate), Tengattini et al. [2014] have extended the above concepts introducing a second scalar variable, the *bond damage* index, given by:

$$D := \frac{P^b(x_b) - P_0^b(x_b)}{P_u^b(x_b) - P_0^b(x_b)} \quad D \in [0, 1] \quad (4)$$

The adoption of the assumption of fractional independence of D and the use of the statistical homogenization over the

bond population lead to the following contribution of bonds to the total free energy of the granular material:

$$\Delta_b \psi(\boldsymbol{\epsilon}^e, D) = \nu_b(1 - D)\psi_r^b(\boldsymbol{\epsilon}^e) \quad (5)$$

in which $\Delta_b \psi$ is the increment of the material free energy due to the presence of bonds and ν_b their volume fraction. In eq. (5) there is no counterpart for the grading index θ^g of grains because, for a fully debonded material, $P_u^b(x_b) = 0$ for all $x_b > 0$.

Based on the results of eqs. (2) and (5), the two scalar quantities B and D are the macroscopic state variables which quantify the mechanical effects of grain crushing and mechanical bond damage in a cemented granular material. Provided that the initial, current and ultimate cumulative grain and bond size distributions are known, both these quantities can be computed. With the current progresses made in the “in-situ” measurements of the geometric features of solid grains and intergranular bonds at the microscale by means of X-ray tomography [see, e.g., Viggiani and Hall, 2012, and references therein] B and D are actually measurable quantities throughout the entire deformation process.

Note that the (macroscopic) elastic strain appearing in the (microscopic) reference free energy functions ψ_r^g and ψ_r^b can be considered the same for both grains and bonds by virtue of the assumption of strain compatibility introduced in Tengattini et al. [2014], Tengattini [2015]. In these works, $\boldsymbol{\epsilon}^e$ is the infinitesimal macroscopic elastic strain. The extension of this approach to the finite deformation regime is addressed in Sect. 3.

2.2. Thermodynamics-based approach to the theory of plasticity

The attempts to derive the evolution equations of the infinitesimal theory of rate-independent plasticity from basic thermodynamics principles can be traced back to the early works of the French school [Moreau, 1970, Halphen and Nguyen, 1975, Germain et al., 1983]. Important contributions to the understanding of the thermo-mechanics of structural materials have been provided, e.g., by Ziegler [1983], Ziegler and Wehrli [1987], Maugin [1992], Reddy and Martin [1993], Han and Reddy [1999]. The advantages of ensuring thermodynamic consistency when dealing with the inelastic behavior of geomaterials have been emphasized by Houlsby [1981] and Collins and Houlsby [1997], in view of the potential drawbacks associated with purely phenomenological modeling of materials featuring stress-dependent stiffness, non-associative behavior and dilatant plastic flow. Significant contributions to the development of infinitesimal elastoplastic models for soils within the framework of continuum thermo-mechanics have been given, for example, by Modaresi et al. [1994], Houlsby and Puzrin [2000], Puzrin and Houlsby [2001], Collins and Kelly [2002], Collins and Hilder [2002], Collins and Muhunthan [2003], Einav and Puzrin [2004], DeSimone and Tamagnini [2005], Einav et al. [2007].

A detailed account of the approach to plasticity theory based on thermodynamic principles, with particular reference to the *theory of hyperplasticity*, in which all the

evolution equations for the state variables are derived from two potential functions (free energy function and dissipation function) is given in the monograph of Houlsby and Puzrin [2007]. In this section, the key points of the application of infinitesimal hyperplasticity to the modeling of crushable, cemented granular materials incorporating micromechanically-based internal variables (as defined in Sect. 2) are briefly summarized.

2.3. Free energy function

In the framework of infinitesimal elastoplasticity, we assume the customary additive decomposition of the total strain tensor into an elastic, reversible part and an inelastic part:

$$\boldsymbol{\epsilon}^e = \boldsymbol{\epsilon} - \boldsymbol{\epsilon}^p \quad (6)$$

By limiting the set of state variables, \mathcal{S} , to the elastic strain tensor $\boldsymbol{\epsilon}^e$, the breakage index B and the damage index D , we postulate the existence of a Helmholtz free energy function per unit volume of the form:

$$\begin{aligned} \psi(\mathcal{S}) &= \psi(\boldsymbol{\epsilon}^e, B, D) \\ &= \nu_g(1 - \theta^g B)\psi_r^g(\boldsymbol{\epsilon}^e) + \nu_b(1 - D)\psi_r^b(\boldsymbol{\epsilon}^e) \end{aligned} \quad (7)$$

obtained by adding the contributions of grains and bonds given by eqs. (2) and (5).

As a consequence of the principle of material frame indifference [see, e.g., Simo and Hughes, 1998], the functions ψ_r^g and ψ_r^b must depend on $\boldsymbol{\epsilon}^e$ only through its invariants. Choosing the principal values ϵ_A^e (with $A = 1, 2, 3$) of $\boldsymbol{\epsilon}^e$ as a suitable set of 3 independent invariant quantities, we have:

$$\psi_r^g(\boldsymbol{\epsilon}^e) = \hat{\psi}_r^g(\epsilon_A^e) \quad \psi_r^b(\boldsymbol{\epsilon}^e) = \hat{\psi}_r^b(\epsilon_A^e) \quad (A = 1, 2, 3) \quad (8)$$

As an alternative, the volumetric and deviatoric elastic strains, defined as:

$$\epsilon_v^e := \text{tr}(\boldsymbol{\epsilon}^e) \quad \epsilon_s^e := \sqrt{\frac{2}{3} \|\text{dev}(\boldsymbol{\epsilon}^e)\|^2} \quad \text{dev}(\boldsymbol{\epsilon}^e) := \boldsymbol{\epsilon}^e - \frac{1}{3} \epsilon_v^e \mathbf{1}$$

can be chosen as arguments of ψ_r^g and ψ_r^b , assuming that there is no dependence of ψ on the third invariant of $\boldsymbol{\epsilon}^e$, see, e.g., Houlsby and Puzrin [2007, Ch. 9].

2.4. Dissipation function

For isothermal processes, the second principle of thermodynamics requires that the dissipation function \mathcal{D} , defined as:

$$\mathcal{D} := \boldsymbol{\sigma} \cdot \dot{\boldsymbol{\epsilon}} - \dot{\psi} \geq 0 \quad (9)$$

is non-negative. Taking into account the definition of free energy function given in the previous section, and introducing the set of *generalized stresses* $\overline{\boldsymbol{\chi}} = \{\overline{\boldsymbol{\chi}}, \overline{\chi}_B, \overline{\chi}_D\}$, defined as:

$$\overline{\boldsymbol{\chi}} = \frac{\partial \psi}{\partial \boldsymbol{\epsilon}^e} \quad \overline{\chi}_B = -\frac{\partial \psi}{\partial B} \quad \overline{\chi}_D = -\frac{\partial \psi}{\partial D} \quad (10)$$

we have:

$$\begin{aligned} \mathcal{D} &= \boldsymbol{\sigma} \cdot \dot{\boldsymbol{\epsilon}} - \{\overline{\boldsymbol{\chi}} \cdot (\dot{\boldsymbol{\epsilon}} - \dot{\boldsymbol{\epsilon}}^p) - \overline{\chi}_B \dot{B} - \overline{\chi}_D \dot{D}\} \\ &= (\boldsymbol{\sigma} - \overline{\boldsymbol{\chi}}) \cdot \dot{\boldsymbol{\epsilon}} + \overline{\boldsymbol{\chi}} \cdot \dot{\boldsymbol{\epsilon}}^p + \overline{\chi}_B \dot{B} + \overline{\chi}_D \dot{D} \geq 0 \end{aligned} \quad (11)$$

For this inequality to hold for any possible non-dissipative processes, for which $\dot{\boldsymbol{\epsilon}}^p = \mathbf{0}$, $\dot{B} = 0$ and $\dot{D} = 0$, we must have:

$$\boldsymbol{\sigma} = \overline{\boldsymbol{\chi}} = \frac{\partial \psi}{\partial \boldsymbol{\epsilon}^e} \quad (12)$$

and the following reduced dissipation inequality must hold:

$$\mathcal{D} = \boldsymbol{\sigma} \cdot \dot{\boldsymbol{\epsilon}}^p + \bar{\chi}_B \dot{B} + \bar{\chi}_D \dot{D} \geq 0 \quad (13)$$

Eq. (13) suggests the following functional dependence for the dissipation function \mathcal{D} on both the set \mathcal{S} of the state variables and the set of dissipative flows $\mathcal{F} := \{\dot{\boldsymbol{\epsilon}}^p, \dot{B}, \dot{D}\}$:

$$\mathcal{D}(\mathcal{S}, \mathcal{F}) = \mathcal{D}(\boldsymbol{\epsilon}^e, B, D, \dot{\boldsymbol{\epsilon}}^p, \dot{B}, \dot{D}) \quad (14)$$

To describe the behavior of a rate-independent material, we postulate that the dissipation function \mathcal{D} is homogeneous of degree one in the elements of \mathcal{F} . Euler's theorem for homogeneous functions then requires that:

$$\mathcal{D} = \frac{\partial \mathcal{D}}{\partial \dot{\boldsymbol{\epsilon}}^p} \cdot \dot{\boldsymbol{\epsilon}}^p + \frac{\partial \mathcal{D}}{\partial \dot{B}} \dot{B} + \frac{\partial \mathcal{D}}{\partial \dot{D}} \dot{D} \quad (15)$$

By introducing the set of *generalized dissipative stresses* $\mathcal{X} := \{\boldsymbol{\chi}, \chi_B, \chi_D\}$, defined as:

$$\boldsymbol{\chi} = \frac{\partial \mathcal{D}}{\partial \dot{\boldsymbol{\epsilon}}^p} \quad \chi_B = \frac{\partial \mathcal{D}}{\partial \dot{B}} \quad \chi_D = \frac{\partial \mathcal{D}}{\partial \dot{D}} \quad (16)$$

eq. (15) can be rewritten as:

$$\mathcal{D} = \boldsymbol{\chi} \cdot \dot{\boldsymbol{\epsilon}}^p + \chi_B \dot{B} + \chi_D \dot{D} \quad (17)$$

Comparing eqs. (13) and (17) we observe that generalized stresses and generalized dissipative stresses must fulfill the following relation:

$$(\boldsymbol{\chi} - \bar{\boldsymbol{\chi}}) \cdot \dot{\boldsymbol{\epsilon}}^p + (\chi_B - \bar{\chi}_B) \dot{B} + (\chi_D - \bar{\chi}_D) \dot{D} = 0 \quad (18)$$

This equality is trivially satisfied if Ziegler's orthogonality conditions [Houlsby and Puzrin, 2007] are assumed:

$$\boldsymbol{\chi} = \bar{\boldsymbol{\chi}} \quad \chi_B = \bar{\chi}_B \quad \chi_D = \bar{\chi}_D \quad (19)$$

Eq. (19) is a sufficient condition for eq. (18) to hold, but not a necessary one. Therefore, Ziegler's orthogonality condition must be considered as a (weak) restrictive constitutive assumption, yet compatible with realistic descriptions of many classes of granular materials characterized by frictional dissipation, see e.g., Collins and Houlsby [1997], Houlsby and Puzrin [2007].

2.5. Yield function and evolution equations

Eq. (17) requires that the (degenerate) partial Legendre transformation of \mathcal{D} with respect to the arguments in \mathcal{F} is a function y , defined *yield function*, such that:

$$\dot{y}(\mathcal{S}, \mathcal{X}) := \boldsymbol{\chi} \cdot \dot{\boldsymbol{\epsilon}}^p + \chi_B \dot{B} + \chi_D \dot{D} - \mathcal{D} = 0 \quad (20)$$

for dissipative processes, i.e., when the elements of \mathcal{F} are non-zero. In the left-hand side of eq. (20), the scalar $\dot{y} \geq 0$ is the *plastic multiplier*. The set:

$$\mathbb{E} := \{(\boldsymbol{\epsilon}^e, B, D, \boldsymbol{\chi}, \chi_B, \chi_D) \in \mathcal{S} \times \mathcal{X} \mid y(\boldsymbol{\epsilon}^e, B, D, \boldsymbol{\chi}, \chi_B, \chi_D) < 0\}$$

is the *elastic domain* of the material, where the plastic multiplier is zero and all the processes are non-dissipative ($\dot{\boldsymbol{\epsilon}}^p = \mathbf{0}$, $\dot{B} = 0$, $\dot{D} = 0$). The boundary of \mathbb{E} :

$$\partial \mathbb{E} := \{(\boldsymbol{\epsilon}^e, B, D, \boldsymbol{\chi}, \chi_B, \chi_D) \in \mathcal{S} \times \mathcal{X} \mid y(\boldsymbol{\epsilon}^e, B, D, \boldsymbol{\chi}, \chi_B, \chi_D) = 0\}$$

is the *yield surface*, on which \dot{y} may be positive and irreversible processes may occur.

From eq. (20) the following *evolution equations* for the elements of \mathcal{F} can be obtained:

$$\dot{\boldsymbol{\epsilon}}^p = \dot{y} \frac{\partial y}{\partial \boldsymbol{\chi}}(\mathcal{S}, \mathcal{X}) = \dot{y} \mathbf{Q}_\sigma(\mathcal{S}, \mathcal{X}) \quad (21a)$$

$$\dot{B} = \dot{y} \frac{\partial y}{\partial \chi_B}(\mathcal{S}, \mathcal{X}) = \dot{y} Q_B(\mathcal{S}, \mathcal{X}) \quad (21b)$$

$$\dot{D} = \dot{y} \frac{\partial y}{\partial \chi_D}(\mathcal{S}, \mathcal{X}) = \dot{y} Q_D(\mathcal{S}, \mathcal{X}) \quad (21c)$$

Eq. (21a) is the standard (associative) flow rule for the plastic strain rate, while eqs. (21b) and (21c) provide the (associative) hardening laws for the internal variables B and D . It is worth noting that the associativity of the flow rule (21a) holds in the generalized dissipative stress space. Thus, this result does not prevent the possibility of modeling non-associative plastic flow in standard Cauchy stress space, see Collins and Houlsby [1997], Houlsby and Puzrin [2007].

The yield function, y , and the flow directions, \mathbf{Q}_σ , Q_B and Q_D , are functions of the state variables and of generalized dissipative stresses. By exploiting Ziegler's orthogonality principle (19) and the constitutive equations (10), providing the elements of \mathcal{X} as functions of the state variables \mathcal{S} , we can define the counterparts of the yield function and of the flow directions in the state variable space as follows:

$$y(\mathcal{S}, \mathcal{X}) = y[\mathcal{S}, \bar{\mathcal{X}}(\mathcal{S})] = y^*(\mathcal{S}) \quad (22a)$$

$$\mathbf{Q}_\sigma(\mathcal{S}, \mathcal{X}) = \mathbf{Q}_\sigma[\mathcal{S}, \bar{\mathcal{X}}(\mathcal{S})] = \mathbf{Q}_\sigma^*(\mathcal{S}) \quad (22b)$$

$$Q_B(\mathcal{S}, \mathcal{X}) = Q_B[\mathcal{S}, \bar{\mathcal{X}}(\mathcal{S})] = Q_B^*(\mathcal{S}) \quad (22c)$$

$$Q_D(\mathcal{S}, \mathcal{X}) = Q_D[\mathcal{S}, \bar{\mathcal{X}}(\mathcal{S})] = Q_D^*(\mathcal{S}) \quad (22d)$$

The corresponding evolution equations for the state variables $\boldsymbol{\epsilon}^e$, B and D are given by:

$$\dot{\boldsymbol{\epsilon}}^e = \dot{\boldsymbol{\epsilon}} - \dot{y} \mathbf{Q}_\sigma^*(\boldsymbol{\epsilon}^e, B, D) \quad (23a)$$

$$\dot{B} = \dot{y} Q_B^*(\boldsymbol{\epsilon}^e, B, D) \quad (23b)$$

$$\dot{D} = \dot{y} Q_D^*(\boldsymbol{\epsilon}^e, B, D) \quad (23c)$$

Given the history of the total strain, and thus of $\dot{\boldsymbol{\epsilon}}$, eqs. (23) can be integrated in time to provide the time histories of the state variables at each material point. Then, the stress tensor $\boldsymbol{\sigma}$ and the generalized stresses $\bar{\chi}_B$ and $\bar{\chi}_D$ can be obtained from eqs. (10) by simple function evaluation.

3. Extension to finite deformation multiplicative plasticity

3.1. Strain decomposition

Let \mathbf{X} be the position of a macroscopic material point – an REV containing a sufficient number of grains to be representative of the macroscopic behavior of the material – in the reference configuration \mathcal{B} of the body at time $t = 0$ and let:

$$\mathbf{x}(\mathbf{X}, t) = \boldsymbol{\phi}(\mathbf{X}, t) \quad (24)$$

be the position occupied by the same material point in the spatial configuration \mathcal{S}_t occupied by the body at time $t > 0$. The key point in finite deformation multiplicative plasticity

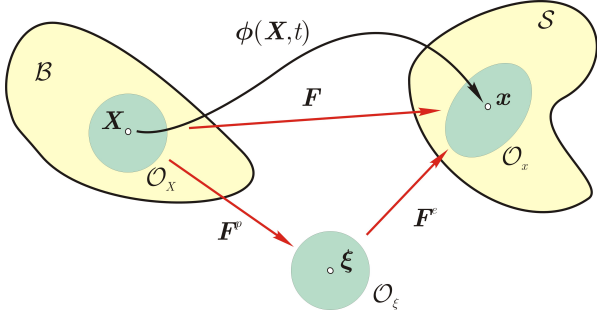


Figure 1. Multiplicative decomposition and intermediate configuration.

is the assumption of a *product decomposition* of the deformation gradient:

$$\mathbf{F} := \nabla_X \phi(\mathbf{X}, t) = \frac{\partial \phi}{\partial \mathbf{X}} \quad (25)$$

into a reversible (elastic) part, \mathbf{F}^e and an irreversible (plastic) part, \mathbf{F}^p , in the form:

$$\mathbf{F} = \mathbf{F}^e \mathbf{F}^p \quad (26)$$

see, e.g., Lee [1968], Simo and Hughes [1998], Borja [2013].

An essential feature of the assumption (26) is the introduction of the concept of *intermediate configuration*, relative to which the elastic response of the material is defined, see Fig. 1. From a phenomenological point of view, $(\mathbf{F}^e)^{-1}$ can be interpreted as the *local* deformation which occurs to the neighborhood \mathcal{O}_x of \mathbf{x} when the material is unloaded back to the reference stress state. It is worth noting that the local configurations for each material point of \mathcal{B} are, in general, not compatible. In addition, the decomposition (26) is not unique as an arbitrary rigid body rotation can be superposed on the intermediate configuration without altering the total deformation gradient. However, the orientation of the (local) intermediate configuration is not relevant if we restrict our theory to isotropic materials.

3.2. Free energy function

Due to the assumption of isotropy, the set \mathcal{S} of state variables is given by the reversible part of the deformation via the left elastic Cauchy–Green deformation tensor:

$$\mathbf{b}^e := \mathbf{F}^e \mathbf{F}^{eT} = \sum_{A=1}^3 b_A^e \mathbf{n}^{(A)} \otimes \mathbf{n}^{(A)} = \sum_{A=1}^3 (\lambda_A^e)^2 \mathbf{n}^{(A)} \otimes \mathbf{n}^{(A)} \quad (27)$$

the grain breakage index B and the bond damage index D :

$$\mathcal{S} := \{\mathbf{b}^e, B, D\}$$

In eq. (27), \mathbf{b}^e is represented in its spectral decomposition, where the eigenvectors $\mathbf{n}^{(A)}$ ($A = 1, 2, 3$) provide the principal directions of \mathbf{b}^e while $b_A^e = (\lambda_A^e)^2$ are the corresponding principal values. The quantities λ_A^e , known as *principal elastic stretches*, are the principal values of \mathbf{F}^e .

The *free energy function* per unit reference volume is then assumed as:

$$\psi(\mathcal{S}) = n_g(1 - \theta^g B) \psi_r^g(\mathbf{b}^e) + n_b(1 - D) \psi_r^b(\mathbf{b}^e) \quad (28)$$

where $n_g = J\nu_g$ and $n_b = J\nu_b$ are the Lagrangian volume fractions of grains and bonds, respectively, and $J = \det(\mathbf{F})$ is the Jacobian determinant of the deformation.

As a consequence of the principle of material frame indifference and the assumption of isotropy, the functions ψ_r^g and ψ_r^b must depend on \mathbf{b}^e only through its invariants. Choosing the principal values b_A^e of \mathbf{b}^e as a suitable set of 3 independent invariant quantities, we have:

$$\psi_r^g(\mathbf{b}^e) = \hat{\psi}_r^g(b_A^e) \quad \psi_r^b(\mathbf{b}^e) = \hat{\psi}_r^b(b_A^e) \quad (A = 1, 2, 3) \quad (29)$$

In view of the following derivations, it is useful to evaluate the objective time rate of the free energy function ψ as provided by eq. (28). We have:

$$\dot{\psi} = \frac{\partial \psi}{\partial \mathbf{b}^e} \cdot \dot{\mathbf{b}}^e + \frac{\partial \psi}{\partial B} \dot{B} + \frac{\partial \psi}{\partial D} \dot{D} \quad (30)$$

Considering that, by the multiplicative decomposition, $\mathbf{F}^e = \mathbf{F} \mathbf{F}^{p-1}$ and defining the plastic right Cauchy–Green deformation tensor as $\mathbf{C}^p := \mathbf{F}^{pT} \mathbf{F}^p$, it follows that:

$$\mathbf{b}^e = \mathbf{F} \mathbf{C}^{p-1} \mathbf{F}^T = \phi_* (\mathbf{C}^{p-1}) \quad (31)$$

i.e., \mathbf{b}^e is the push-forward to the spatial configuration of the inverse of \mathbf{C}^p . Exploiting the identity (31), we have the following important result, [see Simo, 1992, for details]:

$$\dot{\mathbf{b}}^e = \mathbf{l} \mathbf{b}^e + \mathbf{b}^e \mathbf{l}^T + \mathcal{L}_v[\mathbf{b}^e] \quad (32)$$

where $\mathbf{l} = \dot{\mathbf{F}} \mathbf{F}^{-1} = \nabla \mathbf{v}$ is the spatial velocity gradient, and:

$$\mathcal{L}_v[\mathbf{b}^e] = \mathbf{F} \left\{ \frac{d}{dt} (\mathbf{C}^{p-1}) \right\} \mathbf{F}^T = \phi_* \left\{ \frac{d}{dt} (\phi^* \mathbf{b}^e) \right\}$$

is the Lie derivative of the elastic left Cauchy–Green tensor.

It is easy to show that $\mathcal{L}_v[\mathbf{b}^e]$ is related to the time rate of plastic deformations. Let the elastic and plastic velocity gradients be defined as:

$$\mathbf{l}^e := \dot{\mathbf{F}}^e \mathbf{F}^{e-1} \quad \bar{\mathbf{l}}^p := \dot{\mathbf{F}}^p \mathbf{F}^{p-1} \quad (33)$$

and let the spatial plastic velocity gradient \mathbf{l}^p be the push-forward to the spatial configuration of the tensor $\bar{\mathbf{l}}^p$, defined on the intermediate configuration:

$$\mathbf{l}^p = \mathbf{F}^e \bar{\mathbf{l}}^p \mathbf{F}^{e-1} = \mathbf{l} - \mathbf{l}^e \quad (34)$$

Then, the following relation holds between $\mathcal{L}_v[\mathbf{b}^e]$ and \mathbf{l}^p [see Simo, 1998, Ch. 36]:

$$\mathcal{L}_v[\mathbf{b}^e] = -2 \text{sym}(\mathbf{l}^p \mathbf{b}^e) \quad (35)$$

Hence, the third term in the expression for the time rate of \mathbf{b}^e in eq. (32) accounts for the changes of \mathbf{b}^e induced by the development of inelastic deformations.

The definition of \mathbf{l}^p in (34) leads naturally to the following notions of *plastic rate of deformation*, \mathbf{d}^p , and *plastic spin*, $\hat{\mathbf{w}}^p$ tensors:

$$\mathbf{d}^p := \text{sym}(\mathbf{l}^p) \quad \hat{\mathbf{w}}^p := \text{skw}(\mathbf{l}^p) \quad (36)$$

In order to construct a plasticity theory, both components of the plastic velocity gradients need to be specified by suitable flow rules. In view of the isotropic nature of the material behavior, we will assume in the following that the plastic spin is always equal to zero, and $\mathbf{l}^p = \mathbf{d}^p$.

Inserting eqs. (32) and (35) in eq. (30), and considering that:

$$\frac{\partial \psi}{\partial \mathbf{b}^e} \cdot \text{sym}(\mathbf{d}^p \mathbf{b}^e) = \frac{\partial \psi}{\partial \mathbf{b}^e} \cdot (\mathbf{d}^p \mathbf{b}^e)$$

due to the symmetry of $\partial\psi/\partial\mathbf{b}^e$, and that:

$$\frac{\partial\psi}{\partial\mathbf{b}^e} \cdot (\mathbf{l}\mathbf{b}^e) + \frac{\partial\psi}{\partial\mathbf{b}^e} \cdot (\mathbf{b}^e\mathbf{l}^T) = \left(2 \frac{\partial\psi}{\partial\mathbf{b}^e} \mathbf{b}^e\right) \cdot \left(\frac{\mathbf{l} + \mathbf{l}^T}{2}\right)$$

since the two tensors \mathbf{b}^e and $\partial\psi/\partial\mathbf{b}^e$ commute as a consequence of material isotropy, we obtain:

$$\dot{\psi} = \left(2 \frac{\partial\psi}{\partial\mathbf{b}^e} \mathbf{b}^e\right) \cdot \mathbf{d} - \left(2 \frac{\partial\psi}{\partial\mathbf{b}^e} \mathbf{b}^e\right) \cdot \mathbf{d}^p + \frac{\partial\psi}{\partial\dot{B}} \dot{B} + \frac{\partial\psi}{\partial\dot{D}} \dot{D} \quad (37)$$

where $\mathbf{d} = \text{sym}(\mathbf{l})$ is the rate of deformation tensor.

3.3. Dissipation function

For isothermal processes, the second principle of thermodynamics requires that the dissipation function \mathcal{D} per unit reference volume, is non-negative:

$$\mathcal{D} := \boldsymbol{\tau} \cdot \mathbf{d} - \dot{\psi} \geq 0 \quad (38)$$

In the above equation, the tensor $\boldsymbol{\tau} := J\boldsymbol{\sigma}$ is the *Kirchhoff stress tensor*. Taking into account the result of eq. (37) and introducing the set of *generalized stresses* $\overline{\mathcal{K}} = \{\overline{\boldsymbol{\chi}}, \overline{\chi}_B, \overline{\chi}_D\}$, defined as:

$$\overline{\boldsymbol{\chi}}_\tau = 2 \frac{\partial\psi}{\partial\mathbf{b}^e} \mathbf{b}^e \quad \overline{\chi}_B = -\frac{\partial\psi}{\partial\dot{B}} \quad \overline{\chi}_D = -\frac{\partial\psi}{\partial\dot{D}} \quad (39)$$

we have:

$$\mathcal{D} = (\boldsymbol{\tau} - \overline{\boldsymbol{\chi}}_\tau) \cdot \mathbf{d} + \overline{\boldsymbol{\chi}}_\tau \cdot \mathbf{d}^p + \overline{\chi}_B \dot{B} + \overline{\chi}_D \dot{D} \geq 0 \quad (40)$$

For this inequality to hold for any possible non-dissipative processes, for which $\mathbf{d}^p = \mathbf{0}$, $\dot{B} = 0$ and $\dot{D} = 0$, we must have:

$$\boldsymbol{\tau} = \overline{\boldsymbol{\chi}}_\tau = 2 \frac{\partial\psi}{\partial\mathbf{b}^e} \mathbf{b}^e \quad (41)$$

and the following reduced dissipation inequality must hold:

$$\mathcal{D} = \boldsymbol{\tau} \cdot \mathbf{d}^p + \overline{\chi}_B \dot{B} + \overline{\chi}_D \dot{D} \geq 0 \quad (42)$$

This equation suggests the following functional dependence for the dissipation function \mathcal{D} on both the set \mathcal{S} of the state variables and the set of dissipative flows $\mathcal{F} := \{\mathbf{d}^p, \dot{B}, \dot{D}\}$:

$$\mathcal{D}(\mathcal{S}, \mathcal{F}) = \mathcal{D}(\mathbf{b}^e, B, D, \mathbf{d}^p, \dot{B}, \dot{D}) \quad (43)$$

Again, to describe the behavior of a rate-independent material, we postulate that the dissipation function \mathcal{D} is homogeneous of degree one in the elements of \mathcal{F} . Thus, Euler's theorem for homogeneous functions requires that:

$$\mathcal{D} = \frac{\partial\mathcal{D}}{\partial\mathbf{d}^p} \cdot \mathbf{d}^p + \frac{\partial\mathcal{D}}{\partial\dot{B}} \dot{B} + \frac{\partial\mathcal{D}}{\partial\dot{D}} \dot{D} \quad (44)$$

By introducing the set of *generalized dissipative stresses* $\overline{\mathcal{K}} := \{\boldsymbol{\chi}_\tau, \chi_B, \chi_D\}$, defined as:

$$\boldsymbol{\chi}_\tau = \frac{\partial\mathcal{D}}{\partial\mathbf{d}^p} \quad \chi_B = \frac{\partial\mathcal{D}}{\partial\dot{B}} \quad \chi_D = \frac{\partial\mathcal{D}}{\partial\dot{D}} \quad (45)$$

eq. (44) can be rewritten as:

$$\mathcal{D} = \boldsymbol{\chi}_\tau \cdot \mathbf{d}^p + \chi_B \dot{B} + \chi_D \dot{D} \quad (46)$$

Comparing eqs. (42) and (46) we observe that generalized stresses and generalized dissipative stresses must fulfill the following relation:

$$(\boldsymbol{\chi}_\tau - \overline{\boldsymbol{\chi}}_\tau) \cdot \mathbf{d}^p + (\chi_B - \overline{\chi}_B) \dot{B} + (\chi_D - \overline{\chi}_D) \dot{D} = 0 \quad (47)$$

This equality is trivially satisfied if Ziegler's orthogonality conditions are assumed:

$$\boldsymbol{\chi}_\tau = \overline{\boldsymbol{\chi}}_\tau \quad \chi_B = \overline{\chi}_B \quad \chi_D = \overline{\chi}_D \quad (48)$$

as in the small deformation case, see eq. (19) and the associated remarks.

3.4. Yield function and evolution equations

The homogeneity of degree one of the dissipation function in the elements of \mathcal{F} , implies that, as in the linearized kinematics setting, the (degenerate) partial Legendre transformation of \mathcal{D} with respect to \mathbf{d}^p , \dot{B} and \dot{D} provides the *yield function* of the material in the generalized dissipative stresses space:

$$\dot{\gamma} y(\mathcal{S}, \overline{\mathcal{K}}) := \boldsymbol{\chi}_\tau \cdot \mathbf{d}^p + \chi_B \dot{B} + \chi_D \dot{D} - \mathcal{D} = 0 \quad (49)$$

As in eq. (20), the scalar $\dot{\gamma} \geq 0$ is the plastic multiplier. The set:

$$\mathbb{E} := \{(\mathbf{b}^e, B, D, \boldsymbol{\chi}_\tau, \chi_B, \chi_D) \in \mathcal{S} \times \overline{\mathcal{K}} \mid y(\mathbf{b}^e, B, D, \boldsymbol{\chi}_\tau, \chi_B, \chi_D) < 0\}$$

is the elastic domain of the material, where the plastic multiplier is zero and all the processes are non-dissipative ($\mathbf{d}^p = \mathbf{0}$, $\dot{B} = 0$, $\dot{D} = 0$). The boundary of \mathbb{E} :

$$\partial\mathbb{E} := \{(\mathbf{b}^e, B, D, \boldsymbol{\chi}_\tau, \chi_B, \chi_D) \in \mathcal{S} \times \overline{\mathcal{K}} \mid y(\mathbf{b}^e, B, D, \boldsymbol{\chi}_\tau, \chi_B, \chi_D) = 0\}$$

is the yield surface, on which $\dot{\gamma}$ may be positive and irreversible processes may occur.

From eq. (49), a standard argument provides the associative flow rule for \mathbf{d}^p and the associative hardening laws for B and D :

$$\mathbf{d}^p = \dot{\gamma} \frac{\partial y}{\partial\boldsymbol{\chi}_\tau}(\mathcal{S}, \overline{\mathcal{K}}) = \dot{\gamma} \mathbf{Q}_\tau(\mathcal{S}, \overline{\mathcal{K}}) \quad (50a)$$

$$\dot{B} = \dot{\gamma} \frac{\partial y}{\partial\chi_B}(\mathcal{S}, \overline{\mathcal{K}}) = \dot{\gamma} Q_B(\mathcal{S}, \overline{\mathcal{K}}) \quad (50b)$$

$$\dot{D} = \dot{\gamma} \frac{\partial y}{\partial\chi_D}(\mathcal{S}, \overline{\mathcal{K}}) = \dot{\gamma} Q_D(\mathcal{S}, \overline{\mathcal{K}}) \quad (50c)$$

The result of eq. (35) and the flow rule (50a) provide the expression of the Lie derivative of \mathbf{b}^e consistent with the assumed yield function:

$$\mathcal{L}_v[\mathbf{b}^e] = -2 \text{sym}(\mathbf{d}^p \mathbf{b}^e) = -2\dot{\gamma} \text{sym}(\mathbf{Q}_\tau \mathbf{b}^e) \quad (51)$$

It is worth noting that – as for the small deformations case – the associativity of the flow rule, eq. (50a), holds in the generalized dissipative stress space. Thus, this result does not prevent the possibility of modeling non-associative plastic flow in Kirchhoff or Cauchy stress spaces. This represents a significant improvement with respect to the isotropic finite deformation plasticity theory derived by Simo [1992] starting from the principle of maximum dissipation, which imposes the associativity of plastic flow in Kirchhoff stress space.

The yield function, y , and the flow directions, \mathbf{Q}_τ , Q_B and Q_D , are functions of the state variables and of generalized dissipative stresses. By exploiting Ziegler's orthogonality principle (48) and the constitutive equations (39), providing the elements of $\overline{\mathcal{K}}$ as functions of the state variables \mathcal{S} , we

can define the counterparts of the yield function and of the flow directions in the state variable space as follows:

$$y(\mathcal{S}, \mathcal{H}) = y[\mathcal{S}, \overline{\mathcal{H}}(\mathcal{S})] = y^*(\mathcal{S}) \quad (52a)$$

$$\mathbf{Q}_\tau(\mathcal{S}, \mathcal{H}) = \mathbf{Q}_\tau[\mathcal{S}, \overline{\mathcal{H}}(\mathcal{S})] = \mathbf{Q}_\tau^*(\mathcal{S}) \quad (52b)$$

$$Q_B(\mathcal{S}, \mathcal{H}) = Q_B[\mathcal{S}, \overline{\mathcal{H}}(\mathcal{S})] = Q_B^*(\mathcal{S}) \quad (52c)$$

$$Q_D(\mathcal{S}, \mathcal{H}) = Q_D[\mathcal{S}, \overline{\mathcal{H}}(\mathcal{S})] = Q_D^*(\mathcal{S}) \quad (52d)$$

The corresponding evolution equations for the state variables \mathbf{b}^e , B and D are given by:

$$\dot{\mathbf{b}}^e = \mathbf{l}\mathbf{b}^e + \mathbf{b}^e \mathbf{l}^T - 2\dot{\gamma} \mathbf{Q}_\tau^*(\mathbf{b}^e, B, D) \mathbf{b}^e \quad (53a)$$

$$\dot{B} = \dot{\gamma} Q_B^*(\mathbf{b}^e, B, D) \quad (53b)$$

$$\dot{D} = \dot{\gamma} Q_D^*(\mathbf{b}^e, B, D) \quad (53c)$$

In the RHS of eq. (53a) the isotropy of the yield function and of the elastic constitutive equation allows to replace the term $\text{sym}\{\mathbf{Q}_\tau^* \mathbf{b}^e\}$ with $\mathbf{Q}_\tau^* \mathbf{b}^e$, since \mathbf{Q}_τ^* and \mathbf{b}^e commute.

As in the small deformation setting, given the deformation of the body \mathcal{B} , eqs. (53) can be integrated in time to provide the time histories of the state variables at each material point. Then, the Kirchhoff stress tensor $\boldsymbol{\tau}$ and the generalized stresses $\bar{\chi}_B$ and $\bar{\chi}_D$ can be obtained from the constitutive equations (39) by simple function evaluation.

4. Application: a frictional hyperplastic finite deformation model for natural geomaterials

In this section, the general expressions for the hyperplastic constitutive equations derived in Sect. 3 are specialized to a specific class of natural geomaterials, namely, cemented granular materials such as weakly cemented sands, sandstones or calcarenites.

In developing the different constitutive functions, the works of Einav and coworkers on breakage mechanics of granular materials [Einav, 2007a,b, Nguyen and Einav, 2009] as well as the more recent contributions of Tengattini et al. [2014] and Das et al. [2014] have been used as a starting point.

4.1. Free energy function and generalized stresses

In the general expression (28) for the free energy function, the effects of grain breakage B and bond damage D are accounted for by the coefficients $(1 - \theta^g B)$ and $(1 - D)$ originating from statistical homogenization. The dependence of ψ on the elastic deformations is concentrated in the two reference functions $\psi_r^g(\mathbf{b}^e)$ and $\psi_r^b(\mathbf{b}^e)$, which depend on \mathbf{b}^e through its invariants.

Rather than using the principal values of \mathbf{b}^e as suggested by eq. (29), it is expedient to adopt as arguments of the reference free energy functions the three invariants provided by the *logarithmic elastic principal stretches*, defined as:

$$\varepsilon_A^e := \ln(\lambda_A^e) \quad (A = 1, 2, 3) \quad (54)$$

The rationale for this choice will be provided in the forthcoming Sect. 5.

Splitting additively the volumetric and deviatoric contributions to the reference free energies for both grains and bonds, we can write:

$$\psi_r^g(\varepsilon_A^e) = \psi_{r,v}^g(\varepsilon_v^e) + \psi_{r,s}^g(\varepsilon_s^e) \quad (55a)$$

$$\psi_r^b(\varepsilon_A^e) = \psi_{r,v}^b(\varepsilon_v^e) + \psi_{r,s}^b(\varepsilon_s^e) \quad (55b)$$

in which ε_v^e and ε_s^e are the elastic logarithmic volumetric and deviatoric strains defined as:

$$\varepsilon_v^e := \hat{\boldsymbol{\varepsilon}}^e \cdot \boldsymbol{\delta} \quad \varepsilon_s^e := \sqrt{\frac{2}{3} \hat{\boldsymbol{\varepsilon}}^e \cdot \hat{\boldsymbol{\varepsilon}}^e} \quad (56)$$

with:

$$\hat{\boldsymbol{\varepsilon}}^e := \begin{Bmatrix} \varepsilon_1^e \\ \varepsilon_2^e \\ \varepsilon_3^e \end{Bmatrix} \quad \boldsymbol{\delta} := \begin{Bmatrix} 1 \\ 1 \\ 1 \end{Bmatrix} \quad \hat{\boldsymbol{\varepsilon}}^e := \hat{\boldsymbol{\varepsilon}}^e - \frac{1}{3} \varepsilon_v^e \boldsymbol{\delta} = \begin{Bmatrix} \varepsilon_1^e - \varepsilon_v^e/3 \\ \varepsilon_2^e - \varepsilon_v^e/3 \\ \varepsilon_3^e - \varepsilon_v^e/3 \end{Bmatrix}$$

In the choice of the functions $\psi_{r,v}^g$, $\psi_{r,s}^g$, $\psi_{r,v}^b$ and $\psi_{r,s}^b$ different approaches have been proposed. For unbonded or weakly bonded granular materials, whose stiffness is significantly affected by the mean effective stress, a power law can be assumed for the functions $\psi_{r,v}^g(\varepsilon_v^e)$ and $\psi_{r,v}^b(\varepsilon_v^e)$, see, for example, Einav [2007b], Nguyen and Einav [2009].

For weak rocks such as sandstones and calcarenites, whose elastic stiffness is affected by the stress state to a much lesser degree, a convenient choice is to adopt quadratic functions for the volumetric components of the reference free energies, of the form:

$$\psi_{r,v}^g = \frac{1}{2} K^g (\varepsilon_v^e)^2 \quad \psi_{r,v}^b = \frac{1}{2} K^b (\varepsilon_v^e)^2 \quad (57)$$

see Nguyen and Einav [2009]. These quadratic expressions give rise to a linear dependence of the mean Kirchhoff effective stress on the logarithmic volumetric strain. In eq. (57), K^g and K^b are two material constants representing the bulk stiffnesses of grains and of intergranular bond bridges, respectively. Consistently with this choice, we adopt quadratic expressions also for the deviatoric components of the reference free energies, as, for example, in Das et al. [2014]:

$$\psi_{r,s}^g = \frac{3}{2} G^g (\varepsilon_s^e)^2 \quad \psi_{r,s}^b = \frac{3}{2} G^b (\varepsilon_s^e)^2 \quad (58)$$

where G^g and G^b are two additional material constants representing the shear stiffnesses of grains and of intergranular bond bridges, respectively.

Using the expressions (28), (57) and (58), the constitutive equation (41) yields:

$$\boldsymbol{\tau} = \sum_{A=1}^3 \tau_A \mathbf{n}^{(A)} \otimes \mathbf{n}^{(A)} = \sum_{A=1}^3 \frac{\partial \psi}{\partial \varepsilon_A^e} \mathbf{n}^{(A)} \otimes \mathbf{n}^{(A)} \quad (59)$$

where:

$$\tau_A = \frac{\partial \psi}{\partial \varepsilon_A^e} = \bar{K}^{gb} \varepsilon_v^e + 2\bar{G}^{gb} \left(\varepsilon_A^e - \frac{1}{3} \varepsilon_v^e \right) \quad (60)$$

is the A -th principal value of $\boldsymbol{\tau}$, and:

$$\bar{K}^{gb}(B, D) := n_g(1 - \theta^g B) K^g + n_b(1 - D) K^b \quad (61a)$$

$$\bar{G}^{gb}(B, D) := n_g(1 - \theta^g B) G^g + n_b(1 - D) G^b \quad (61b)$$

represent the volume-averaged bulk and shear stiffnesses of the granular medium, decreasing monotonically as grain breakage and bond damage evolve towards the final damage state with $B = D = 1$. The details of the derivation of eq. (59) are provided in Appendix A.

Eq. (59) shows that the principal directions of $\boldsymbol{\tau}$ are, as expected for isotropic elasticity, the same of the elastic left Cauchy–Green tensor \mathbf{b}^e , and that the relations between the principal values of Kirchhoff stress and the principal elastic logarithmic strains, provided by eq. (60), are strikingly similar to the elastic constitutive equations between $\boldsymbol{\sigma}$ and $\boldsymbol{\epsilon}^e$ of an isotropic material in the small deformation setting.

By introducing the vector $\hat{\boldsymbol{\tau}} := \{\tau_1, \tau_2, \tau_3\}^T$ of principal Kirchhoff stresses, eq. (60) can be rewritten in a more compact vector form as:

$$\hat{\boldsymbol{\tau}} = \bar{K}^{gb} \boldsymbol{\epsilon}_v^e \boldsymbol{\delta} + 2\bar{G}^{gb} \hat{\boldsymbol{\epsilon}}^e = \hat{\mathbf{D}}^e \hat{\boldsymbol{\epsilon}}^e \quad (62)$$

where the elastic stiffness matrix in principal stress space, $\hat{\mathbf{D}}^e$, is given by:

$$\hat{\mathbf{D}}^e := \left(\bar{K}^{gb} - \frac{2}{3} \bar{G}^{gb} \right) \boldsymbol{\delta} \otimes \boldsymbol{\delta} + 2\bar{G}^{gb} \mathbf{I}_3 \quad (63)$$

in which \mathbf{I}_3 is the 3×3 identity matrix and $\boldsymbol{\delta} := \{1, 1, 1\}^T$.

Finally, from eqs. (28), (39), (57) and (58), we obtain the following expressions for the generalized stresses $\bar{\chi}_B$ and $\bar{\chi}_D$:

$$\bar{\chi}_B = n_g \theta^g \left\{ \frac{1}{2} K^g (\boldsymbol{\epsilon}_v^e)^2 + \frac{2}{3} G^g (\boldsymbol{\epsilon}_s^e)^2 \right\} \quad (64)$$

$$\bar{\chi}_D = n_b \left\{ \frac{1}{2} K^b (\boldsymbol{\epsilon}_v^e)^2 + \frac{2}{3} G^b (\boldsymbol{\epsilon}_s^e)^2 \right\} \quad (65)$$

Note that being ψ a linear function of B and D , $\bar{\chi}_B$ and $\bar{\chi}_D$ depend only on \mathbf{b}^e through its logarithmic elastic strain invariants $\boldsymbol{\epsilon}_v^e$ and $\boldsymbol{\epsilon}_s^e$.

4.2. Dissipation and yield functions

A suitable choice for the dissipation function \mathcal{D} for an isotropic cohesive–frictional material is provided by the work of Tengattini et al. [2014]. In this work, we adapt this dissipation function to the finite deformation regime, replacing Cauchy mean stress with Kirchhoff mean stress $p := \text{tr}(\boldsymbol{\tau})/3$:

$$\mathcal{D} = \sqrt{\mathcal{D}_{p,v}^2 + \mathcal{D}_{p,s}^2 + \mathcal{D}_B^2 + \mathcal{D}_D^2} \quad (66)$$

where:

$$\mathcal{D}_{p,v} = (p + p_t) \sqrt{\frac{E_{BC}}{\bar{\chi}_B}} \frac{1}{(1-B) \sin \omega_B} d_v^p \quad (67a)$$

$$\mathcal{D}_{p,s} = M \left\{ p + p_t(1-D) \right\} d_s^p \quad (67b)$$

$$\mathcal{D}_B = \frac{\sqrt{E_{BC} \bar{\chi}_B}}{(1-B) \cos \omega_B} \dot{B} \quad (67c)$$

$$\mathcal{D}_D = \frac{\sqrt{E_{DC} \bar{\chi}_D}}{(1-D)} \dot{D} \quad (67d)$$

are the components of the dissipation function associated to the plastic volumetric deformation, plastic distortional deformation, grain breakage and bond damage, respectively.

In eqs. (67a) and (67b), the invariant quantities:

$$d_v^p := \text{tr}(\mathbf{d}^p) \quad d_s^p := \sqrt{\frac{2}{3} \text{dev}(\mathbf{d}^p) \cdot \text{dev}(\mathbf{d}^p)}$$

are the volumetric and deviatoric components of the plastic rate of deformation tensor \mathbf{d}^p . The scalar coefficients p_t , M , E_{BC} , E_{DC} and ω_B are material constants, whose physical interpretation is discussed in Sect. 4.5. As compared to the original dissipation function of Tengattini et al. [2014], the only minor difference is in the function $\mathcal{D}_{p,v}$, where the mean stress p is replaced by the quantity $(p + p_t)$ to prevent the volumetric plastic flow from becoming singular at $p = 0$, see eq. (74).

Let:

$$p_\chi := \frac{1}{3} \text{tr}(\boldsymbol{\chi}_\tau) \quad q_\chi := \sqrt{\frac{3}{2} \text{dev}(\boldsymbol{\chi}_\tau) \cdot \text{dev}(\boldsymbol{\chi}_\tau)} \quad (68)$$

be the first and second invariants of the generalized dissipative stress $\boldsymbol{\chi}_\tau$, work-conjugated to d_v^p and d_s^p , respectively; eqs. (45), (66) and (67) then yield:

$$p_\chi = \frac{\partial \mathcal{D}}{\partial d_v^p} = \frac{1}{\Gamma_p} \frac{\mathcal{D}_{p,v}}{\mathcal{D}} \quad (69a)$$

$$q_\chi = \frac{\partial \mathcal{D}}{\partial d_s^p} = \frac{1}{\Gamma_q} \frac{\mathcal{D}_{p,s}}{\mathcal{D}} \quad (69b)$$

$$\chi_B = \frac{\partial \mathcal{D}}{\partial \dot{B}} = \frac{1}{\Gamma_B} \frac{\mathcal{D}_B}{\mathcal{D}} \quad (69c)$$

$$\chi_D = \frac{\partial \mathcal{D}}{\partial \dot{D}} = \frac{1}{\Gamma_D} \frac{\mathcal{D}_D}{\mathcal{D}} \quad (69d)$$

with:

$$\Gamma_{p,v} = \left(\frac{\partial \mathcal{D}_{p,v}}{\partial d_v^p} \right)^{-1} = \frac{(1-B) \sin \omega_B}{p + p_t} \sqrt{\frac{\bar{\chi}_B}{E_{BC}}} \quad (70a)$$

$$\Gamma_{p,s} = \left(\frac{\partial \mathcal{D}_{p,s}}{\partial d_s^p} \right)^{-1} = \frac{1}{M [p + p_t(1-D)]} \quad (70b)$$

$$\Gamma_B = \left(\frac{\partial \mathcal{D}_B}{\partial \dot{B}} \right)^{-1} = (1-B) \cos \omega_B \sqrt{\frac{1}{\bar{\chi}_B E_{BC}}} \quad (70c)$$

$$\Gamma_D = \left(\frac{\partial \mathcal{D}_D}{\partial \dot{D}} \right)^{-1} = (1-D) \sqrt{\frac{1}{\bar{\chi}_D E_{DC}}} \quad (70d)$$

Given the definition of dissipation function provided by eq. (66) and the results of eqs. (69), we can obtain the partial Legendre transform of \mathcal{D} , i.e., the yield function in the $\mathcal{S} \times \mathcal{K}$ space, by observing that:

$$\begin{aligned} y(\mathcal{S}, \mathcal{K}) &= \left(\frac{\mathcal{D}_{p,v}}{\mathcal{D}} \right)^2 + \left(\frac{\mathcal{D}_{p,s}}{\mathcal{D}} \right)^2 + \left(\frac{\mathcal{D}_B}{\mathcal{D}} \right)^2 + \left(\frac{\mathcal{D}_D}{\mathcal{D}} \right)^2 - 1 \\ &= (\Gamma_{p,v} p_\chi)^2 + (\Gamma_{p,s} q_\chi)^2 + (\Gamma_B \chi_B)^2 + (\Gamma_D \chi_D)^2 - 1 = 0 \end{aligned}$$

After substituting the expressions for the coefficients Γ of eq. (70), the full expression for the yield function is obtained:

$$y = \frac{\bar{\chi}_B(1-B)^2 \sin^2 \omega_B}{E_{BC}} \left(\frac{p_\chi}{p+p_t} \right)^2 + \frac{(1-B)^2 \cos^2 \omega_B}{E_{BC}} \frac{\bar{\chi}_B^2}{\bar{\chi}_B} + \frac{(1-D)^2 \chi_D^2}{E_{DC} \bar{\chi}_D} + \frac{q_\chi^2}{M^2 [p+p_t(1-D)]^2} - 1 = 0 \quad (71)$$

4.3. Flow rule in generalized dissipative stress space

In view of eq. (71), the plastic flow direction \mathbf{Q}_τ can be computed as follows, with the use of the chain rule for derivation of composite functions:

$$\mathbf{Q}_\tau = \frac{\partial y}{\partial \chi_\tau} = \frac{\partial y}{\partial p_\chi} \frac{\partial p_\chi}{\partial \chi_\tau} + \frac{\partial y}{\partial q_\chi} \frac{\partial q_\chi}{\partial \chi_\tau} \quad (72)$$

where:

$$\frac{\partial p_\chi}{\partial \chi_\tau} = \frac{1}{3} \mathbf{1} \quad \frac{\partial q_\chi}{\partial \chi_\tau} = \frac{3}{2} \frac{1}{q_\chi} \text{dev}(\chi_\tau) \quad (73)$$

and:

$$\frac{\partial y}{\partial p_\chi} = \frac{2\bar{\chi}_B(1-B)^2 \sin^2 \omega_B}{E_{BC}} \frac{p_\chi}{(p+p_t)^2} \quad (74)$$

$$\frac{\partial y}{\partial q_\chi} = \frac{2q_\chi}{M^2 [p+p_t(1-D)]^2} \quad (75)$$

Collecting the results in eqs. (72)–(75), we obtain:

$$\mathbf{Q}_\tau = \frac{2\bar{\chi}_B(1-B)^2 \sin^2 \omega_B}{3E_{BC}} \frac{p_\chi}{(p+p_t)^2} \mathbf{1} + \frac{3}{M^2 [p+p_t(1-D)]^2} \text{dev}(\chi_\tau) \quad (76)$$

The hardening functions Q_B and Q_D can be also determined by differentiating eq. (71) with respect to χ_B and χ_D , obtaining:

$$Q_B = \frac{\partial y}{\partial \chi_B} = \frac{2(1-B)^2 \cos^2 \omega_B}{E_{BC}} \frac{\chi_B}{\bar{\chi}_B} \quad (77)$$

$$Q_D = \frac{\partial y}{\partial \chi_D} = \frac{2(1-D)^2 \chi_D}{E_{DC} \bar{\chi}_D} \quad (78)$$

From the expressions in eqs. (76)–(78), the associative flow rule and hardening laws of eq. (50) specialize in the present case to:

$$\mathbf{d}^p = \dot{\gamma} \left\{ \frac{2\bar{\chi}_B(1-B)^2 \sin^2 \omega_B}{3E_{BC}} \frac{p_\chi}{(p+p_t)^2} \mathbf{1} + \frac{3 \text{dev}(\chi_\tau)}{M^2 [p+p_t(1-D)]^2} \right\} \quad (79a)$$

$$\dot{B} = \dot{\gamma} \left\{ \frac{2(1-B)^2 \cos^2 \omega_B}{E_{BC}} \frac{\chi_B}{\bar{\chi}_B} \right\} \quad (79b)$$

$$\dot{D} = \dot{\gamma} \left\{ \frac{2(1-D)^2 \chi_D}{E_{DC} \bar{\chi}_D} \right\} \quad (79c)$$

subject to the Kuhn–Tucker complementarity conditions:

$$y(\mathcal{S}, \mathcal{K}) \leq 0 \quad \dot{\gamma} \geq 0 \quad \dot{\gamma} y(\mathcal{S}, \mathcal{K}) = 0 \quad (80)$$

4.4. Yield function and flow directions in state variable space

The yield function provided by eq. (71) as well as the flow directions \mathbf{Q}_τ , Q_B and Q_D , appearing in the evolution equations (79), depend on the state variables \mathbf{b}^e , B and D and on the generalized dissipative stresses χ_τ , χ_B and χ_D .

By assuming the validity of Ziegler's orthogonality condition ($\chi_\tau = \boldsymbol{\tau}$, $\chi_B = \bar{\chi}_B$ and $\chi_D = \bar{\chi}_D$) and taking into account that the generalized stresses are functions of \mathbf{b}^e , B and D through the constitutive equations (59), (64) and (65), we can reformulate the evolution problem for the state variables in the state variables space as follows:

$$\mathbf{d}^p = \dot{\gamma} \mathbf{Q}_\tau^*(\mathbf{b}^e, B, D) \quad (81a)$$

$$\dot{B} = \dot{\gamma} Q_B^*(\mathbf{b}^e, B, D) \quad (81b)$$

$$\dot{D} = \dot{\gamma} Q_D^*(\mathbf{b}^e, B, D) \quad (81c)$$

subject to the Kuhn–Tucker complementarity conditions:

$$y^*(\mathbf{b}^e, B, D) \leq 0 \quad \dot{\gamma} \geq 0 \quad \dot{\gamma} y^*(\mathbf{b}^e, B, D) = 0 \quad (82)$$

where:

$$\mathbf{Q}_\tau^* = \frac{2\bar{\chi}_B(1-B)^2 \sin^2 \omega_B}{3E_{BC}} \frac{p}{(p+p_t)^2} \mathbf{1} + \frac{3 \mathbf{s}}{M^2 [p+p_t(1-D)]^2} \quad (83a)$$

$$Q_B^* = \frac{2(1-B)^2 \cos^2 \omega_B}{E_{BC}} \quad (83b)$$

$$Q_D^* = \frac{2(1-D)^2}{E_{DC}} \quad (83c)$$

In the above equations $\mathbf{s} = \text{dev}(\boldsymbol{\tau})$ is the deviatoric part of Kirchhoff stress tensor, and the yield function is provided by:

$$y^* = \frac{\bar{\chi}_B(1-B)^2 \sin^2 \omega_B}{E_{BC}} \left(\frac{p}{p+p_t} \right)^2 + \frac{\bar{\chi}_B(1-B)^2 \cos^2 \omega_B}{E_{BC}} + \frac{\bar{\chi}_D(1-D)^2}{E_{DC}} + \frac{q^2}{M^2 [p+p_t(1-D)]^2} - 1 = 0 \quad (84)$$

In deriving eqs. (83) and (84) the identities $p_\chi = p$ and $q_\chi = q$ have been used between the invariants of χ_τ and $\boldsymbol{\tau}$. The relevant definition for q can be obtained from eq. (68), replacing $\text{dev}(\chi_\tau)$ with \mathbf{s} .

It is worth noting that the evolution equations (81), together with the algebraic constraints (82) define a theory of hyperplasticity formulated in elastic strain space, rather than in stress space, following an approach which, for finite deformation plasticity applications in geomechanics, has been pioneered by Borja and Tamagnini [1998]. In this respect, the Kirchhoff stress tensor $\boldsymbol{\tau}$ and the generalized stresses $\bar{\chi}_B$ and $\bar{\chi}_D$ can be considered as dependent variables, which can be obtained from eqs. (59), (64) and (65) by a straightforward function evaluation.

The yield surface of eq. (84) can be easily represented in stress invariants space by considering that the generalized stresses $\bar{\chi}_B$ and $\bar{\chi}_D$ can be cast as functions of p and q through the elastic constitutive equations:

$$\varepsilon_v^e = \frac{p}{K^g b} \quad \varepsilon_s^e = \frac{q}{3G^g b}$$

easily derived from eq. (60) or (62). Substituting these equations in eqs. (64) and (65), we get $y^*(\varepsilon_v^e, \varepsilon_s^e, B, D) = y^*(p, q, B, D)$.

In the asymptotic conditions of full grain breakage and complete bond damage ($B = D = 1$), the yield surface reduces to the Drucker–Prager cone of a cohesionless soil:

$$y^* = q - Mp = 0 \quad (85)$$

In all the other circumstances, the yield surface in stress space has a drop-like shape and it is closed on the positive part of the p axis, as shown in Figs. 2 and 3. The yield surface crosses the positive part of the p axis at an apparent pre-consolidation pressure p_c given by the following implicit equation (see Appendix B):

$$\Xi_2 = 1 - p_c^2 \left\{ f_{Bs} \xi_B \left(\frac{p_c}{p_c + p_t} \right)^2 + f_{Bc} \xi_B + f_D \xi_D \right\} = 0 \quad (86)$$

for $p_c > 0$ and any values of $B < 1$ and $D < 1$. Eq. (86) can be solved in closed form only in the particular case of $p_t = 0$. Otherwise, a numerical procedure such as Newton’s method is required to find p_c . Plastic yielding under isotropic compression is induced by grain breakage and bond damage. When one of B or D are relatively low, the changes induced in p_c by the increase of the other state variable are relatively limited, see Figs. 2a and 3. However, for an almost completely debonded material ($D = 0.9$), p_c increases very fast with grain breakage, producing a behavior under isotropic compression similar to that of normally consolidated clays, see Fig. 2b. In practice, B and D increase simultaneously during plastic loading processes, and the expected response of the model in isotropic compression is typically similar to the one shown in Fig. 2b.

The flow rule in eqs. (81) and (83a) allows to determine the dilatancy $\mathfrak{D} := -d_v^p/d_s^p$ of the material as a function of p , q , B and D (see Appendix B):

$$\mathfrak{D} = -M^2 \left(\frac{p}{q} \right) \left[\frac{p + p_t(1-D)}{p + p_t} \right]^2 f_{Bs} (\xi_B p^2 + \eta_B q^2) \quad (87)$$

The sign of \mathfrak{D} is provided by the mean stress p : the material contracts ($\mathfrak{D} < 0$) when $p > 0$ and dilates ($\mathfrak{D} > 0$) otherwise, with a critical state line ($\mathfrak{D} = 0$) coinciding with the q axis. The plastic flow directions along the yield surface are shown, for constant B and D values, in Fig. 4. In the figure, contractant flow is represented by red arrows, while dilatant flow is shown with blue arrows. For the particular set of material constants adopted in generating the data in Fig. 4, the plastic flow in the low stress range is almost isochoric, while significant contractancy occurs along the yield surface “cap” at high mean stresses.

The impossibility of reproducing a dilatant behavior for positive (compressive) mean stresses could represent a limitation for the applications of the model to a large class of granular materials [Tengattini, 2015, Ch. 4]. This limitation

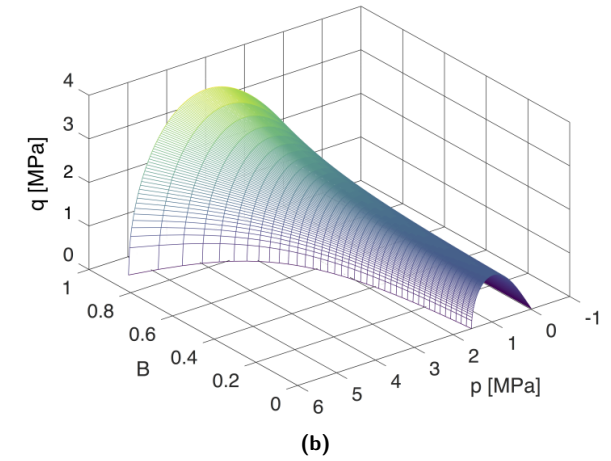
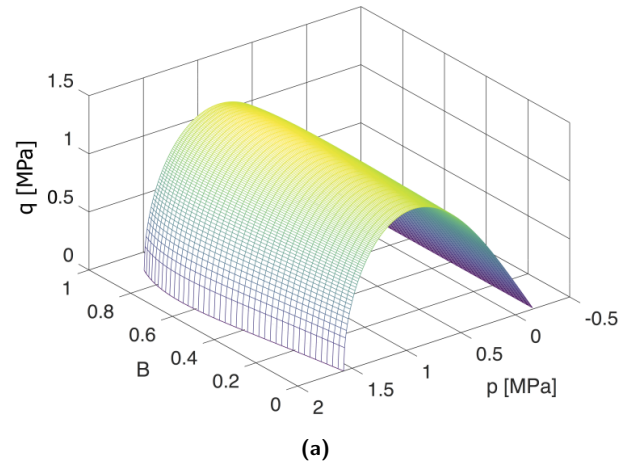


Figure 2. Yield function in (p, q, B) space: a) $D = 0.1$; b) $D = 0.9$. Material constants from Set 1 of Tab. 1.

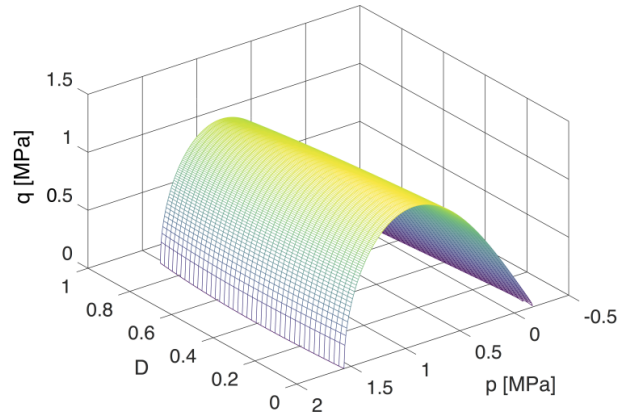


Figure 3. Yield function in (p, q, D) space for $B = 0.0$. Material constants from Set 1 of Tab. 1.

could be circumvented by introducing an isotropic back-stress depending on plastic deformations via a suitable modification of the free energy function, see e.g., Collins [2003], or with a modification of the dissipation function, as in the works of Tengattini et al. [2016] and Houlsby [2019],

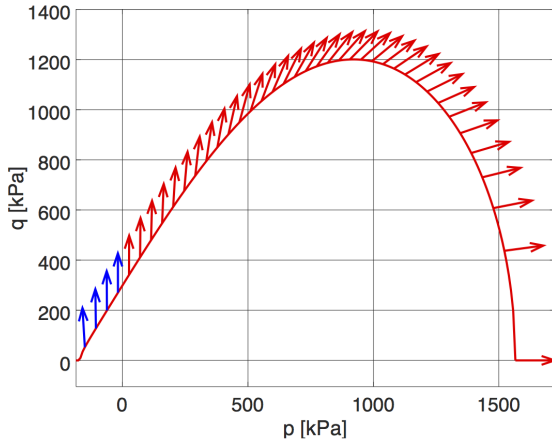


Figure 4. Yield function in (p, q) space for $B = 0.0$ and $D = 0.0$. Arrows provide the local direction of the plastic flow. Contractant flow is represented with red arrows, dilatant flow with blue arrows. Material constants from Set 1 of Tab. 1.

who uses an indicator function to impose a unilateral dilatancy constraint. In this work, mainly oriented towards the modeling of crushable cemented granular materials with a relatively open microstructure and showing a collapsing behavior upon compressive stress paths – such as, for example, the Italian calcarenites – this version of the model can still be considered adequate. Further modifications to the present formulation could be introduced without difficulties.

4.5. Model calibration

The proposed model – as its small deformation counterpart of Tengattini et al. [2014], Das et al. [2014] – is fully characterized by 12 material constants:

- the grading index θ^g and the Lagrangian porosities n_g and n_b (dimensionless), which can be determined from the initial (reference) state of the material;
- the grains bulk and shear moduli K^g and G^g (dimensions $[\text{FL}^{-2}]$);
- the bonds bulk and shear moduli K^b and G^b (dimensions $[\text{FL}^{-2}]$);
- the friction coefficient M (dimensionless), linked to the friction angle of the material at a fully damaged state ($B = D = 1$);
- the mean isotropic Kirchhoff stress at yield under isotropic tension, p_t (dimensions $[\text{FL}^{-2}]$);
- the critical breakage and bond damage energies per unit volume, E_{BC} and E_{DC} (dimensions $[\text{FL}^{-2}]$), see Einav [2007b], Tengattini et al. [2014];
- the coupling angle $\omega_B \in (0, \pi/2)$, controlling the balance between the grain breakage and plastic volumetric dissipation effects, with the role of plastic volumetric dissipation increasing with ω_B , as well as the material tendency to plastic volumetric compaction.

The grading index θ^g can be determined from the grain size distributions measured on the intact and fully damaged states of the grain phase. The volume fraction of the grains must add to the volume fraction of the bond to give the total volume fractions of solids: $n_g + n_b = n_s = 1 - n$, where n is the Lagrangian porosity of the material. Although n can be easily measured, the determination of the individual volume fractions requires a detailed microstructural analysis, with microscopy or X-ray tomography imaging.

The calibration of the elastic constants can be performed indirectly from the measurements of the pre-yield response of the material upon isotropic compression and during the deviatoric stage of a drained triaxial compression test. These two testing conditions allow the determination of the average moduli \bar{K}^{gb} and \bar{G}^{gb} . Knowing the volume fractions n_g and n_b as well as the pre-yield state of the material in terms of B and D (typically, $B = D = 0$), is not sufficient to obtain K^g, K^b, G^g and G^b from \bar{K}^{gb} and \bar{G}^{gb} . However, the knowledge of the mineralogic composition of grains and intergranular bonds can provide a reasonable estimate of the ratios K^g/K^b and G^g/G^b , from which the individual microscopic elastic constants can be estimated.

In Appendix B it is shown that, in the low stress range, the yield surface can be approximated quite well by a Drucker-Prager cone of equation:

$$q = M_{\text{app}}(p + p_{t,\text{app}}) \quad (88)$$

where:

$$M_{\text{app}} = M \left(\frac{1}{1 + \mu^2} \right)^{3/2} \simeq M$$

$$p_{t,\text{app}} = p_t(1 - D)(1 + \mu^2) \simeq p_t(1 - D)$$

In the above relations, the term $1 + \mu^2 \simeq 1$ when, as it is often the case, $\mu^2 \ll 1$. Based on this observation, the constant M could be measured as the slope of the line interpolating the yield states in the $q : p$ plane, measured in drained triaxial compression tests performed at low confining stresses. If the material can be considered as fully bonded ($D = 0$) at the start of the same tests, the value of the constant p_t can be obtained as the intercept of the same interpolation line with the negative part of the p axis. Another possible way to obtain experimental information on p_t is to observe that, for a cohesive-frictional material with constant friction angle ϕ , the uniaxial tensile strength σ_t is linked to p_t by the relation:

$$p_t = \frac{\sigma_t (1 + \sin \phi)}{2 \sin \phi} = \sigma_t \frac{(3 + 2M)}{3M} \quad (89)$$

as, under TX compression:

$$M = \frac{6 \sin \phi}{3 - \sin \phi} \quad \Leftrightarrow \quad \sin \phi = \frac{3M}{(6 + M)}$$

The tensile strength of the material can easily be determined by routine tests such as the Brazilian tensile strength test.

As far as the breakage and bond damage critical energies are concerned, it would be tempting to link them to the fundamental properties of grains and cement bonds at the microscale (e.g., grain crushing pressure). Unfortunately, the presence of cement bonds in the intact material makes this task very difficult. An alternative is to derive E_{BC} and

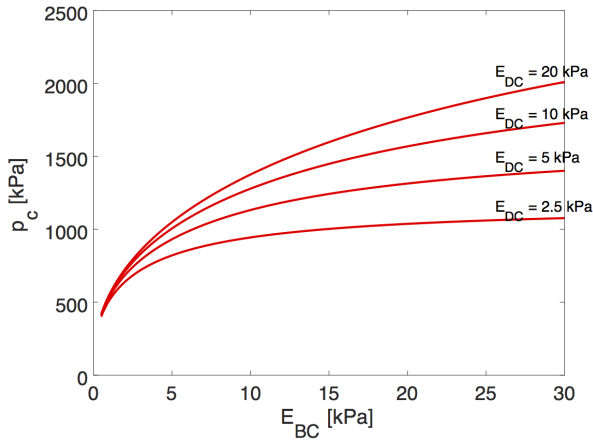
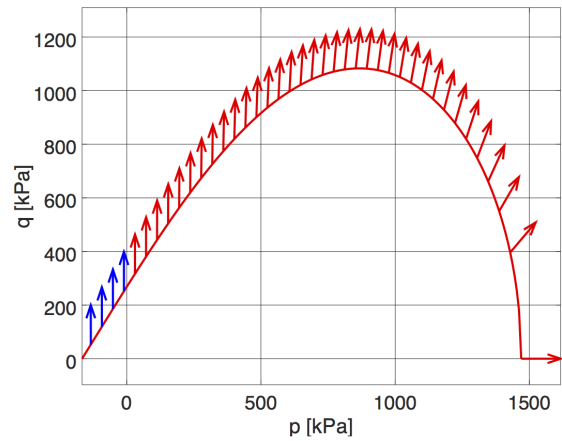


Figure 5. Effect of critical breakage and bond damage energies on isotropic yield stress p_c , for $B = 0.0$ and $D = 0.1$. Material constants from Set 1 of Tab. 1.

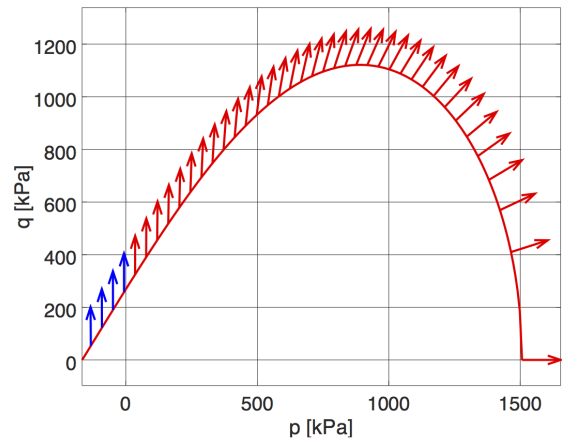
E_{DC} indirectly, associating their values to the macroscopic behavior of the material. The two critical energies control the evolution rate of B and D – the larger E_{BC} and E_{DC} , the slower the increase of B and D towards their asymptotic values, see eqs. (83b) and (83c). Thus, the measurement of the change of B and D with accumulated (plastic) deformations would provide a way to estimate these constants. However, this would only be possible if micromechanical measurements – say, X-ray CT scans of the specimen taken “in-situ” during the test – are available.

A possible alternative is to link the values of E_{BC} and E_{DC} to the mean effective stress at first yield in isotropic compression – i.e., the preconsolidation pressure p_c provided by eq. (86). Fig. 5 shows how the critical energies affect p_c for an almost intact material. As expected, p_c increases monotonically with both E_{BC} and E_{DC} . If E_{BC} is low, p_c is almost insensitive to E_{DC} . The effect of critical bond damage energy increases as E_{BC} increases. The preconsolidation pressure tends to reach an asymptotic value for large values of E_{BC} . The asymptotic limit increases with increasing E_{DC} . Assuming that the other material constants are known, a graphical representation like Fig. 5 can help in obtaining an indication of the most appropriate values for E_{BC} and E_{DC} for a given material, provided that p_c at first yield has been measured and a reasonable estimate of the ratio E_{DC}/E_{BC} can be obtained, based, for example, on the mineralogical composition of the grains and the bonds.

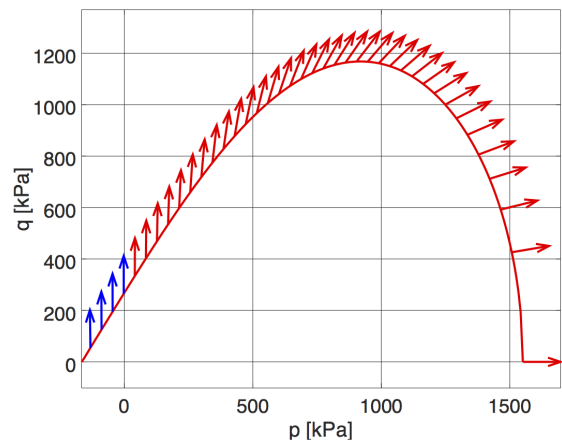
The last constant ω_B controls the plastic volumetric strain rate, and thus the dilatancy \mathcal{D} of the material, for yield states located on the “cap” of the yield surface. This can be seen by looking at the plastic flow directions computed for 3 different values of ω_B in the range between 20° and 60° , shown in Fig. 6. As ω_B increases, the contractancy ($-\mathcal{D}$) predicted at a given stress ratio q/p increases, as indicated by the clockwise rotation of the plastic flow vectors. Note that the different yield surfaces shown in the figure are not identical, as ω_B has some influence, albeit relatively small, on the size and shape of the yield surface, see eq. (84).



(a)



(b)



(c)

Figure 6. Effect of coupling angle on plastic flow direction for $B = D = 0.0$: a) $\omega_B = 20^\circ$; b) $\omega_B = 40^\circ$; c) $\omega_B = 60^\circ$. Material constants from Set 1 of Tab. 1.

Based on this observation, an estimate of ω_B could be provided by a stress–dilatancy plot (\mathcal{D} vs. q/p) obtained from a series of drained TX compression tests at different confining pressures, designed in such a way to touch the yield surface cap at different q/p values.

It is worth noting that all the constants E_{BC} , E_{DC} and ω_B affect both the initial value of the preconsolidation pressure p_c and the stress–dilatancy behavior of the material, although to a different extent. Therefore, the procedures suggested for their indirect determination could require some iterations in order to find the set of data which fits the observed behavior best.

5. Numerical integration of the evolution equations

In order to apply the proposed model to the solution of relevant engineering problems by means of the Finite Element method, it is necessary to define a strategy which allows the integration of the constitutive equations in rate–form at the material point level for a given history of the deformation.

More precisely, let $\mathbb{I} = \bigcup_{n=0}^N [t_n, t_{n+1}]$ a partition of the time interval of interest into time steps. It is assumed that at time $t_n \in \mathbb{I}$ the state of the material $\mathcal{S}_n = \{\mathbf{b}_n^e, B_n, D_n\}$ and the deformation gradient \mathbf{F}_n are known at any Gauss point in the adopted finite element discretization. Let:

$$\mathbf{u}_{n+1}(\mathbf{x}_n) := \boldsymbol{\phi}_{n+1}(\mathbf{x}_n) - \boldsymbol{\phi}_n$$

be the (given) relative displacement vector in the configuration $\boldsymbol{\phi}_n(\mathcal{B})$. Then, the deformation gradient at time t_{n+1} can be evaluated as:

$$\mathbf{F}_{n+1} = \mathbf{f}_{n+1} \mathbf{F}_n \quad \mathbf{f}_{n+1} = \mathbf{1} + \frac{\partial \mathbf{u}_{n+1}}{\partial \mathbf{x}_n} \quad (90)$$

the second order tensor $\mathbf{f}_{n+1} = \partial \boldsymbol{\phi}_{n+1} / \partial \mathbf{x}_n$ being the relative deformation gradient of the incremental motion carrying the body \mathcal{B} from the spatial configuration \mathcal{S}_n to \mathcal{S}_{n+1} . The computational problem to be addressed is then the update of the state variables:

$$\mathbf{b}_{n+1}^e \rightarrow \hat{\mathbf{b}}^e(\mathbf{f}_{n+1}; \mathbf{b}_n^e, B_n, D_n) \quad (91a)$$

$$B_{n+1} \rightarrow \hat{B}(\mathbf{f}_{n+1}; \mathbf{b}_n^e, B_n, D_n) \quad (91b)$$

$$D_{n+1} \rightarrow \hat{D}(\mathbf{f}_{n+1}; \mathbf{b}_n^e, B_n, D_n) \quad (91c)$$

through the integration of the system of ordinary differential equations defining the inelastic response of the material:

$$\dot{\mathbf{f}} = \mathbf{l} \mathbf{f} \quad (92a)$$

$$\dot{\mathbf{b}}^e = \mathbf{l} \mathbf{b}^e + \mathbf{b}^e \mathbf{l}^T - 2\dot{\gamma} \mathbf{Q}_\tau^* \mathbf{b}^e \quad (92b)$$

$$\dot{B} = \dot{\gamma} Q_B^* \quad (92c)$$

$$\dot{D} = \dot{\gamma} Q_D^* \quad (92d)$$

$$y^* \leq 0, \quad \dot{\gamma} \geq 0, \quad \dot{\gamma} y^* = 0 \quad (92e)$$

subjected to the initial conditions:

$$\mathbf{f}|_{t=t_n} = \mathbf{1} \quad \mathbf{b}^e|_{t=t_n} = \mathbf{b}_n^e \quad B|_{t=t_n} = B_n \quad D|_{t=t_n} = D_n \quad (93)$$

In eqs. (92), the flow directions \mathbf{Q}_τ^* , Q_B^* and Q_D^* are given by eqs. (83). The development of a fully implicit integration algorithm for the solution of this problem is described in the following sections 5.1–5.4.

Box 1. Operator split of the evolution problem.

	Problem 1 (elastic predictor)	Problem 2 (plastic corrector)
Evolution equations	$\dot{\mathbf{f}} = \mathbf{l} \mathbf{f}$ $\dot{\mathbf{b}}^e = \mathbf{l} \mathbf{b}^e + \mathbf{b}^e \mathbf{l}^T$ $\dot{B} = 0$ $\dot{D} = 0$	$\dot{\mathbf{f}} = \mathbf{0}$ $\dot{\mathbf{b}}^e = -2\dot{\gamma} \mathbf{Q}_\tau^* \mathbf{b}^e$ $\dot{B} = \dot{\gamma} Q_B^*$ $\dot{D} = \dot{\gamma} Q_D^*$
Initial conditions	$\mathbf{b}^e(t = t_n) = \mathbf{b}_n^e$ $B(t = t_n) = B_n$ $D(t = t_n) = D_n$	$\mathbf{b}^e = \mathbf{b}_{n+1}^{e, \text{tr}}$ $B = B_{n+1}^{\text{tr}}$ $D = D_{n+1}^{\text{tr}}$
Constraints	none	$y^*(\mathbf{b}^e, B, D) \leq 0$ $\dot{\gamma} \geq 0$ $y^*(\mathbf{b}^e, B, D) \dot{\gamma} = 0$

5.1. Operator split of the evolution problem

For the numerical integration of the evolution equations (92), we proceed along standard lines in computational plasticity by adopting the *operator split* shown in Box 1, suggested by the additive structure of eq. (92b).

The computational strategy is to solve Problem 1 first, with initial conditions provided by eq. (93), obtaining the so–called *trial solution* $\mathcal{S}_{n+1}^{\text{tr}}$. Then, if the constraints of Problem 2 are violated, solve Problem 2 using the trial solution as initial conditions. The attractiveness of this strategy stands in the geometric interpretation which can be given to each Problem, as detailed below.

5.2. Problem 1: elastic predictor

The evolution equations of Problem 1, also known as *elastic predictor* problem, can be obtained from the original problem by assuming that no dissipative processes take place (i.e., $\dot{\gamma} = 0$) and ignoring the constraint placed on the state variables by the yield function.

From a geometric point of view, during the elastic predictor stage the update of the current configuration from \mathcal{S}_n to \mathcal{S}_{n+1} takes place at fixed intermediate configuration (modulo a rigid body rotation), with $\mathbf{F}_{n+1}^{p, \text{tr}} = \mathbf{F}_n^p$. Thus we have:

$$\mathbf{F}_{n+1} = \mathbf{f}_{n+1} \mathbf{F}_n = \mathbf{F}_{n+1}^{e, \text{tr}} \mathbf{F}_n^p \Rightarrow \mathbf{F}_{n+1}^{e, \text{tr}} = \mathbf{f}_{n+1} \mathbf{F}_n^e \quad (94)$$

From this last result and the (trivial) evolution equations for B and D of the elastic predictor problem, the complete trial state is obtained:

$$\mathbf{b}_{n+1}^{e, \text{tr}} = \mathbf{f}_{n+1} \mathbf{b}_n^e \mathbf{f}_{n+1}^T \quad B_{n+1}^{\text{tr}} = B_n \quad D_{n+1}^{\text{tr}} = D_n \quad (95)$$

It is worth noting that, due to its formulation in terms of kinematics, the solution of the elastic predictor problem provided by eqs. (95) is exact. The trial value of \mathbf{b}^e at the end of the step is just the geometric update (actually, the push–forward) of \mathbf{b}_n^e to the current configuration \mathcal{S}_{n+1} via the relative deformation gradient.

For the trial state, Kirchhoff stress $\boldsymbol{\tau}$ and the generalized stresses $\bar{\chi}_B$ and $\bar{\chi}_D$ are provided by eqs. (59), (64) and (65):

$$\begin{aligned}\boldsymbol{\tau}_{n+1}^{\text{tr}} &= \sum_{A=1}^3 \boldsymbol{\tau}_{A,n+1}^{\text{tr}} \mathbf{n}_{n+1}^{(A),\text{tr}} \otimes \mathbf{n}_{n+1}^{(A),\text{tr}} \\ &= \sum_{A=1}^3 \left(\frac{\partial \psi}{\partial \boldsymbol{\varepsilon}_A^e} \right)_{n+1}^{\text{tr}} \mathbf{n}_{n+1}^{(A),\text{tr}} \otimes \mathbf{n}_{n+1}^{(A),\text{tr}}\end{aligned}\quad (96)$$

$$\bar{\chi}_{B,n+1}^{\text{tr}} = n_g \theta^g \left\{ \frac{1}{2} K^g (\boldsymbol{\varepsilon}_{v,n+1}^{e,\text{tr}})^2 + \frac{2}{3} G^g (\boldsymbol{\varepsilon}_{s,n+1}^{e,\text{tr}})^2 \right\} \quad (97)$$

$$\bar{\chi}_{D,n+1}^{\text{tr}} = n_b \left\{ \frac{1}{2} K^b (\boldsymbol{\varepsilon}_{v,n+1}^{e,\text{tr}})^2 + \frac{2}{3} G^b (\boldsymbol{\varepsilon}_{s,n+1}^{e,\text{tr}})^2 \right\} \quad (98)$$

where:

$$\begin{aligned}\left(\frac{\partial \psi}{\partial \boldsymbol{\varepsilon}_A^e} \right)_{n+1}^{\text{tr}} &= (\bar{K}^{gb})_{n+1}^{\text{tr}} \boldsymbol{\varepsilon}_{v,n+1}^{e,\text{tr}} \\ &\quad + 2(\bar{G}^{gb})_{n+1}^{\text{tr}} \left(\boldsymbol{\varepsilon}_{A,n+1}^{e,\text{tr}} - \frac{1}{3} \boldsymbol{\varepsilon}_{v,n+1}^{e,\text{tr}} \right)\end{aligned}\quad (99)$$

and:

$$\begin{aligned}(\bar{K}^{gb})_{n+1}^{\text{tr}} &:= \bar{K}^{gb} (B_{n+1}^{\text{tr}}, D_{n+1}^{\text{tr}}) \\ (\bar{G}^{gb})_{n+1}^{\text{tr}} &:= \bar{G}^{gb} (B_{n+1}^{\text{tr}}, D_{n+1}^{\text{tr}})\end{aligned}$$

In the above equations, $\mathbf{n}_{n+1}^{(A),\text{tr}}$ is the A -th unit eigenvector of $\mathbf{b}_{n+1}^{e,\text{tr}}$, $\boldsymbol{\varepsilon}_{A,n+1}^{e,\text{tr}}$ is the corresponding logarithmic principal elastic strain, and $\boldsymbol{\varepsilon}_{v,n+1}^{e,\text{tr}}$ and $\boldsymbol{\varepsilon}_{s,n+1}^{e,\text{tr}}$ are the logarithmic volumetric and deviatoric elastic strains, respectively.

5.3. Problem 2: plastic corrector

If the trial state $\mathcal{S}_{n+1}^{\text{tr}}$ satisfies the constraint posed by the Kuhn–Tucker conditions, i.e. :

$$(y^*)_{n+1}^{\text{tr}} := y^* (\mathbf{b}_{n+1}^{e,\text{tr}}, B_{n+1}^{\text{tr}}, D_{n+1}^{\text{tr}}) \leq 0$$

then the trial state is the exact update of the material state we had been looking for. Otherwise, the intermediate configuration needs to be modified in order to restore the consistency with the yield surface:

$$y_{n+1}^* = y^* (\mathbf{b}_{n+1}^e, B_{n+1}, D_{n+1}) = 0 \quad (100)$$

where \mathbf{b}_{n+1}^e , B_{n+1} and D_{n+1} are obtained as the solution of the differential–algebraic Problem 2, also known as *plastic corrector* problem. Since $\dot{\mathbf{f}} = \mathbf{0}$ in this case, Problem 2 is formulated on a fixed current configuration \mathcal{S}_{n+1} .

The evolution equations of Problem 2 must be integrated numerically, adopting an implicit strategy such as the Backward Euler formula. In particular, the structure of the evolution equation for \mathbf{b}^e suggest the use of the following exponential approximation [Simo, 1992]:

$$\mathbf{b}_{n+1}^e = \exp \{ -2\Delta\gamma_{n+1} \mathbf{Q}_{\tau,n+1}^* \} \mathbf{b}_{n+1}^{e,\text{tr}} \quad (101)$$

where $\Delta\gamma_{n+1}$ is the increment of the plastic multiplier associated to the plastic deformations, to be determined as part of the solution.

Using the Backward Euler algorithm to integrate the evolution equations for B and D yields:

$$B_{n+1} = B_{n+1}^{\text{tr}} + \Delta\gamma_{n+1} Q_{B,n+1}^* \quad (102)$$

$$D_{n+1} = D_{n+1}^{\text{tr}} + \Delta\gamma_{n+1} Q_{D,n+1}^* \quad (103)$$

In principle, the system of 9 non–linear algebraic equations (100)–(103) can be solved to provide the 9 unknowns \mathbf{b}_{n+1}^e , B_{n+1} , D_{n+1} and $\Delta\gamma_{n+1}$. However, the solution of the plastic corrector problem can be significantly simplified by exploiting the isotropy of the material response, as shown in the following section.

5.4. Plastic corrector in principal logarithmic elastic strains space

Due to the assumption of material isotropy and Ziegler’s orthogonality condition, the tensor $\mathbf{Q}_{\tau,n+1}^*$ has the same principal directions of \mathbf{b}_{n+1}^e , see eqs. (59) and (83a). Therefore, the spectral decomposition of the tensors \mathbf{b}_{n+1}^e , $\mathbf{Q}_{\tau,n+1}^*$ and $\mathbf{b}_{n+1}^{e,\text{tr}}$ appearing in eq. (101) read:

$$\mathbf{b}_{n+1}^e = \sum_{A=1}^3 \left(\lambda_{A,n+1}^e \right)^2 \mathbf{n}_{n+1}^{(A)} \otimes \mathbf{n}_{n+1}^{(A)} \quad (104a)$$

$$\mathbf{Q}_{\tau,n+1}^* = \sum_{A=1}^3 Q_{A,n+1}^* \mathbf{n}_{n+1}^{(A)} \otimes \mathbf{n}_{n+1}^{(A)} \quad (104b)$$

$$\mathbf{b}_{n+1}^{e,\text{tr}} = \sum_{A=1}^3 \left(\lambda_{A,n+1}^{e,\text{tr}} \right)^2 \mathbf{n}_{n+1}^{(A),\text{tr}} \otimes \mathbf{n}_{n+1}^{(A),\text{tr}} \quad (104c)$$

where the quantities $\lambda_A^{e,\text{tr}}$ and $\mathbf{n}^{(A),\text{tr}}$ denote the trial principal elastic stretches (eigenvalues of $\mathbf{F}^{e,\text{tr}}$) and the unit eigenvectors of $\mathbf{b}^{e,\text{tr}}$, respectively, while the scalars $Q_{A,n+1}^*$ are the principal values of \mathbf{Q}^* .

Rewriting eq. (101) as:

$$\exp \{ 2\Delta\gamma_{n+1} \mathbf{Q}_{\tau,n+1}^* \} \mathbf{b}_{n+1}^e = \mathbf{b}_{n+1}^{e,\text{tr}}$$

and incorporating the spectral decompositions (104), it easy to show that:

- a) the principal directions of \mathbf{b}_{n+1}^e coincide with the (known) principal directions of $\mathbf{b}_{n+1}^{e,\text{tr}}$:

$$\mathbf{n}_{n+1}^{(A)} = \mathbf{n}_{n+1}^{(A),\text{tr}} \quad (A = 1, 2, 3) \quad (105)$$

- b) the principal values of the three tensors \mathbf{b}_{n+1}^e , $\mathbf{Q}_{\tau,n+1}^*$ and $\mathbf{b}_{n+1}^{e,\text{tr}}$ are related by the following equations:

$$\left(\lambda_{A,n+1}^e \right)^2 = \exp \{ -2\Delta\gamma_{n+1} Q_{A,n+1}^* \} \left(\lambda_{A,n+1}^{e,\text{tr}} \right)^2 \quad (106)$$

with $A = 1, 2$ or 3 .

The result in eq. (106) is particularly relevant since, taking the natural logarithm of both sides, we obtain:

$$\varepsilon_{A,n+1}^e = \varepsilon_{A,n+1}^{e,\text{tr}} - \Delta\gamma_{n+1} Q_{A,n+1}^*$$

or, in vector notation:

$$\hat{\boldsymbol{\varepsilon}}_{n+1}^e = \hat{\boldsymbol{\varepsilon}}_{n+1}^{e,\text{tr}} - \Delta\gamma_{n+1} \hat{\mathbf{Q}}_{n+1}^* \quad (107)$$

Box 2. Plastic corrector problem.

(1) Determine the trial principal elastic stretches $\lambda_{A,n+1}^{e, \text{tr}}$ and the principal eigenvectors $\mathbf{n}_{n+1}^{(A), \text{tr}}$ via the spectral decomposition of $\mathbf{b}_{n+1}^{e, \text{tr}}$.

(2) Set:

$$\mathbf{n}_{n+1}^{(A)} = \mathbf{n}_{n+1}^{(A), \text{tr}} \quad (A = 1, 2, 3)$$

(3) Solve the system of nonlinear algebraic equations:

$$\hat{\boldsymbol{\varepsilon}}_{n+1}^e = \hat{\boldsymbol{\varepsilon}}_{n+1}^{e, \text{tr}} - \Delta\gamma_{n+1} \hat{\mathbf{Q}}^* (\hat{\boldsymbol{\varepsilon}}_{n+1}^e, B_{n+1}, D_{n+1})$$

$$B_{n+1} = B_{n+1}^{\text{tr}} + \Delta\gamma_{n+1} Q_B^* (\hat{\boldsymbol{\varepsilon}}_{n+1}^e, B_{n+1}, D_{n+1})$$

$$D_{n+1} = D_{n+1}^{\text{tr}} + \Delta\gamma_{n+1} Q_D^* (\hat{\boldsymbol{\varepsilon}}_{n+1}^e, B_{n+1}, D_{n+1})$$

$$\hat{\gamma}_{n+1}^* = \hat{\gamma}^* (\hat{\boldsymbol{\varepsilon}}_{n+1}^e, B_{n+1}, D_{n+1}) = 0$$

via Newton's method, to obtain the updated state variables at the end of the step.

(4) Recover \mathbf{b}_{n+1}^e , $\boldsymbol{\tau}_{n+1}$, $\bar{\chi}_{B,n+1}$ and $\bar{\chi}_{D,n+1}$ using the spectral decomposition and the hyperelastic constitutive equations:

$$\mathbf{b}_{A,n+1}^e = \exp\left(2\varepsilon_{A,n+1}^e\right) \quad \mathbf{b}_{n+1}^e = \sum_{A=1}^3 b_{A,n+1}^e \mathbf{n}_{n+1}^{(A)} \otimes \mathbf{n}_{n+1}^{(A)}$$

$$\boldsymbol{\tau}_{A,n+1} = \left(\frac{\partial \psi}{\partial \varepsilon_A^e} \right)_{n+1} \quad \boldsymbol{\tau}_{n+1} = \sum_{A=1}^3 \tau_{A,n+1} \mathbf{n}_{n+1}^{(A)} \otimes \mathbf{n}_{n+1}^{(A)}$$

$$\bar{\chi}_{B,n+1} = - \left(\frac{\partial \psi}{\partial B} \right)_{n+1} \quad \bar{\chi}_{D,n+1} = - \left(\frac{\partial \psi}{\partial D} \right)_{n+1}$$

where:

$$\varepsilon_{A,n+1}^{e, \text{tr}} := \ln(\lambda_{A,n+1}^{e, \text{tr}}) \quad \hat{\boldsymbol{\varepsilon}}^{e, \text{tr}} := \begin{Bmatrix} \varepsilon_1^{e, \text{tr}} \\ \varepsilon_2^{e, \text{tr}} \\ \varepsilon_3^{e, \text{tr}} \end{Bmatrix} \quad \hat{\mathbf{Q}}^* := \begin{Bmatrix} Q_{\tau,1}^* \\ Q_{\tau,2}^* \\ Q_{\tau,3}^* \end{Bmatrix}$$

The set of 6 non-linear algebraic equations provided by eqs. (100), (102), (103) and (107) can then be solved using Newton's method to obtain the updated state at the end of the step, $\hat{\boldsymbol{\varepsilon}}_{n+1}^e$, B_{n+1} , D_{n+1} , and the plastic multiplier increment $\Delta\gamma_{n+1}$, as shown in Box 2. The details of the numerical solution of the plastic corrector problem are provided in Appendix C.

As noted by Simo [1992], the use of the exponential algorithm in connection with the choice of formulating the plastic corrector problem in principal logarithmic elastic strain space leads to an algebraic system of equations which are formally similar to the Generalized Backward Euler algorithm of infinitesimal plasticity [see, e.g. Tamagnini et al., 2002, Borja et al., 2003].

6. Consistent linearization of the integration algorithm

One of the main advantages of the implicit generalized Backward Euler algorithm presented in Sect. 5 is that it is

amenable to closed form linearization, which is an important feature whenever Newton's method is used to solve iteratively the discretized equilibrium equations at the global level.

Let:

$$\mathcal{G}(\boldsymbol{\phi}, \boldsymbol{\eta}) = \mathcal{G}_{\text{int}}(\boldsymbol{\phi}, \boldsymbol{\eta}) - \mathcal{G}_{\text{ext}} = \int_{\mathcal{B}} \boldsymbol{\tau}(\boldsymbol{\phi}) \cdot (\nabla \boldsymbol{\eta}) dV - \mathcal{G}_{\text{ext}} = 0 \quad (108)$$

be the variational form of the equilibrium equations, i.e., the principle of virtual work, expressing the equality between the virtual work done by the Kirchhoff stress field over the virtual deformation field and the virtual work of the external forces \mathcal{G}_{ext} for any kinematically admissible virtual displacement field $\boldsymbol{\eta}$.

The computation of the Jacobian of the internal force vector in a typical time step is based on the discretization of the linearized form of \mathcal{G}_{int} with respect to a infinitesimal perturbation $\delta \mathbf{u}$ of the current deformation $\boldsymbol{\phi}$:

$$D_u \mathcal{G}_{\text{int}}(\boldsymbol{\phi}, \boldsymbol{\eta})[\delta \mathbf{u}] = \int_{\mathcal{B}} \{ \nabla^s \boldsymbol{\eta} \cdot (\tilde{\mathbf{c}} \nabla^s \delta \mathbf{u}) \} dV + \int_{\mathcal{B}} \{ \boldsymbol{\tau} \cdot (\nabla \delta \mathbf{u})^T (\nabla \boldsymbol{\eta}) \} dV \quad (109)$$

in which $\tilde{\mathbf{c}}$ is the so-called *algorithmic tangent stiffness tensor*, given for the case at hand by the following expression [see, e.g. Simo, 1998]:

$$\tilde{\mathbf{c}} = \sum_{A=1}^3 \sum_{B=1}^3 \hat{d}_{AB} \mathbf{m}^A \otimes \mathbf{m}^B - \sum_{A=1}^3 2\tau_A \mathbf{m}^A + \sum_{A \neq B} \left\{ \frac{\tau_A (\lambda_B^{e, \text{tr}})^2 - \tau_B (\lambda_A^{e, \text{tr}})^2}{(\lambda_A^{e, \text{tr}})^2 - (\lambda_B^{e, \text{tr}})^2} \right\} \mathbf{M}^{AB} \quad (110)$$

where:

$$\mathbf{m}^A := \mathbf{n}^{(A)} \otimes \mathbf{n}^{(A)} \quad \mathbf{m}^{AB} := \mathbf{n}^{(A)} \otimes \mathbf{n}^{(B)} \quad \mathbf{m}^{BA} := \mathbf{n}^{(B)} \otimes \mathbf{n}^{(A)} \\ \mathbf{M}^{(AB)} := \mathbf{m}^{AB} \otimes \mathbf{m}^{AB} + \mathbf{m}^{AB} \otimes \mathbf{m}^{BA}$$

and the quantities \hat{d}_{AB} , given by:

$$\hat{d}_{AB} := \frac{\partial \tau_A}{\partial \varepsilon_B^{e, \text{tr}}} \quad (111)$$

are the components of the (3×3) matrix $\hat{\mathbf{d}} := \partial \boldsymbol{\tau} / \partial \hat{\boldsymbol{\varepsilon}}^{e, \text{tr}}$ of tangent moduli in principal strain space. In presence of repeated eigenvalues for $\mathbf{b}^{e, \text{tr}}$, the third term on the RHS of eq. (110) becomes singular. The singularity can be easily eliminated as shown in Ogden [1984], Ch. 6.

For the case at hand, the exact calculation of the matrix $\hat{\mathbf{d}}$ is possible only if, during the current time step, the loading process is elastic. When the plastic deformations occur, the Kirchhoff stress tensor is provided as a function of the

state variables whose values at the end of the step are determined numerically via the algorithm of Box 2. In such conditions, the evaluation of $\hat{\mathbf{d}}$ requires the linearization of the integration algorithm and proceeds as follows. From the elastic constitutive equation (62) we have:

$$\begin{aligned} \hat{\mathbf{d}}_{n+1}^{(k)} &= \left(\frac{\partial \hat{\boldsymbol{\tau}}}{\partial \hat{\boldsymbol{\varepsilon}}^e} \right)_{n+1}^{(k)} \left(\frac{\partial \hat{\boldsymbol{\varepsilon}}^e}{\partial \hat{\boldsymbol{\varepsilon}}^{e,\text{tr}}} \right)_{n+1}^{(k)} \\ &+ \left(\frac{\partial \hat{\boldsymbol{\tau}}}{\partial B} \right)_{n+1}^{(k)} \left(\frac{\partial B}{\partial \hat{\boldsymbol{\varepsilon}}^{e,\text{tr}}} \right)_{n+1}^{(k)} + \left(\frac{\partial \hat{\boldsymbol{\tau}}}{\partial D} \right)_{n+1}^{(k)} \left(\frac{\partial D}{\partial \hat{\boldsymbol{\varepsilon}}^{e,\text{tr}}} \right)_{n+1}^{(k)} \end{aligned} \quad (112)$$

By considering that:

$$\left(\frac{\partial \hat{\boldsymbol{\tau}}}{\partial \hat{\boldsymbol{\varepsilon}}^e} \right)_{n+1}^{(k)} = \left(\frac{\partial^2 \psi}{\partial \hat{\boldsymbol{\varepsilon}}^e \otimes \partial \hat{\boldsymbol{\varepsilon}}^e} \right)_{n+1}^{(k)} =: (\hat{\mathbf{D}}^e)_{n+1}^{(k)} \quad (113a)$$

$$\left(\frac{\partial \hat{\boldsymbol{\tau}}}{\partial B} \right)_{n+1}^{(k)} = \left(\frac{\partial^2 \psi}{\partial \hat{\boldsymbol{\varepsilon}}^e \partial B} \right)_{n+1}^{(k)} =: (\hat{\mathbf{D}}_B^e)_{n+1}^{(k)} \quad (113b)$$

$$\left(\frac{\partial \hat{\boldsymbol{\tau}}}{\partial D} \right)_{n+1}^{(k)} = \left(\frac{\partial^2 \psi}{\partial \hat{\boldsymbol{\varepsilon}}^e \partial D} \right)_{n+1}^{(k)} =: (\hat{\mathbf{D}}_D^e)_{n+1}^{(k)} \quad (113c)$$

where $\hat{\mathbf{D}}^e$, $\hat{\mathbf{D}}_B^e$ and $\hat{\mathbf{D}}_D^e$ are the elastic and coupling matrices of the material, respectively, eq. (112) can be rewritten in compact form as:

$$\hat{\mathbf{d}}_{n+1}^{(k)} = \hat{\mathbf{K}}_{n+1}^{e(k)} \left(\frac{\partial \mathbf{x}}{\partial \hat{\boldsymbol{\varepsilon}}^{e,\text{tr}}} \right)_{n+1}^{(k)} \quad (114)$$

in which:

$$\mathbf{x}_{n+1}^{(k)} := \begin{Bmatrix} (\hat{\boldsymbol{\varepsilon}}^e)_{n+1}^{(k)} \\ B_{n+1}^{(k)} \\ D_{n+1}^{(k)} \\ \Delta \gamma_{n+1}^{(k)} \end{Bmatrix} \quad \hat{\mathbf{K}}_{n+1}^{e(k)} := \begin{bmatrix} \hat{\mathbf{D}}^e & \hat{\mathbf{D}}_B^e & \hat{\mathbf{D}}_D^e & \mathbf{0}_{(3 \times 1)} \end{bmatrix}_{n+1}^{(k)} \quad (115)$$

The derivative $\partial \mathbf{x} / \partial \hat{\boldsymbol{\varepsilon}}^{e,\text{tr}}$ measures the variation in the converged solution of the iteration algorithm used to solve the plastic corrector problem for an infinitesimal change in the relative displacement gradient \mathbf{f}_{n+1} , and thus in $\hat{\boldsymbol{\varepsilon}}_{n+1}^{e,\text{tr}}$. This quantity can be obtained by linearizing the plastic corrector problem equations in Box 2.

Let $\mathbf{x}_{n+1}^{(k),\text{tr}} := \{(\hat{\boldsymbol{\varepsilon}}^{e,\text{tr}})^T, B^{\text{tr}}, D^{\text{tr}}, 0\}_{n+1}^{(k)T}$ be the trial value of solution vector \mathbf{x} and let:

$$\mathbf{g}_{n+1}^{(k)} := \mathbf{x}_{n+1}^{(k),\text{tr}} - \mathbf{R}_{n+1}^{(k)} = \begin{Bmatrix} (\hat{\boldsymbol{\varepsilon}}^e)_{n+1}^{(k)} + \Delta \gamma_{n+1}^{(k)} (\hat{\mathbf{Q}}^*)_{n+1}^{(k)} \\ B_{n+1}^{(k)} - \Delta \gamma_{n+1}^{(k)} (Q_B^*)_{n+1}^{(k)} \\ D_{n+1}^{(k)} - \Delta \gamma_{n+1}^{(k)} (Q_D^*)_{n+1}^{(k)} \\ (y^*)_{n+1}^{(k)} \end{Bmatrix} \quad (116)$$

the difference between $\mathbf{x}_{n+1}^{(k),\text{tr}}$ and the residual vector $\mathbf{R}_{n+1}^{(k)}$ of eq. (138), i.e., the only part of the residual vector which actually depends on the problem unknowns. Then the governing equations of the plastic corrector problem in Box 2 can be recast as follows:

$$\mathbf{g} \left(\mathbf{x}_{n+1}^{(k)} \right) = \mathbf{x}_{n+1}^{(k),\text{tr}} \quad (117)$$

Deriving both sides of eq. (117) with respect to $\hat{\boldsymbol{\varepsilon}}^{e,\text{tr}}$, we have:

$$\left(\frac{\partial \mathbf{g}}{\partial \mathbf{x}} \right)_{n+1}^{(k)} \left(\frac{\partial \mathbf{x}}{\partial \hat{\boldsymbol{\varepsilon}}^{e,\text{tr}}} \right)_{n+1}^{(k)} = \left(\frac{\partial \mathbf{x}^{\text{tr}}}{\partial \hat{\boldsymbol{\varepsilon}}^{e,\text{tr}}} \right)_{n+1}^{(k)} \quad (118)$$

Noting that:

$$\left(\frac{\partial \mathbf{g}}{\partial \mathbf{x}} \right)_{n+1}^{(k)} = - \left(\frac{\partial \mathbf{R}}{\partial \mathbf{x}} \right)_{n+1}^{(k)} = -\mathbf{J}_{n+1}^{(k)} \quad (119)$$

$$\left(\frac{\partial \mathbf{x}^{\text{tr}}}{\partial \hat{\boldsymbol{\varepsilon}}^{e,\text{tr}}} \right)_{n+1}^{(k)} = \begin{Bmatrix} \mathbf{I}_3 \\ \mathbf{0}_{(3 \times 3)} \end{Bmatrix} =: \mathbf{P} \quad (120)$$

where \mathbf{J} is the Jacobian matrix of eq. (142) of Appendix C, and considering that this matrix is non-singular if the plastic corrector problem is well-posed, we obtain:

$$\left(\frac{\partial \mathbf{x}}{\partial \hat{\boldsymbol{\varepsilon}}^{e,\text{tr}}} \right)_{n+1}^{(k)} = -(\mathbf{J}^{-1})_{n+1}^{(k)} \mathbf{P} \quad (121)$$

and, finally:

$$\hat{\mathbf{d}}_{n+1}^{(k)} = -\hat{\mathbf{K}}_{n+1}^{e(k)} (\mathbf{J}^{-1})_{n+1}^{(k)} \mathbf{P} \quad (122)$$

The evaluation of the RHS of eq. (122) is relatively easy as the Jacobian matrix has already been computed in the iterative solution of the local plastic corrector problem and its components are given in Appendix C.

7. Numerical examples

In this section, a series of numerical examples are presented to demonstrate the relevance of geometric non-linearity for the model discussed in Sect. 4 and the efficiency and accuracy of the integration algorithm presented in Sect. 5.

All the simulations have been performed adopting the three sets of material constants listed in Tab. 1. The data of Set 1 are taken from Das et al. [2014] for the Gravina calcarenite, the only difference being the volume fractions n_g and n_b , which have been evaluated assuming an initial void ratio $e_0 = 1.15$ and a ratio between n_g/n_b equal to 4. Set 2 differs from Set 1 only for the values of the critical breakage and damage energies, taken as 50% of the original values to simulate a material with weaker grains and intergranular bonds. In Set 3, only the critical bond damage energy has been reduced by 50%. Whenever the scope of the simulation is to highlight the effects of a specific constant on the material response, the values adopted for this constant are explicitly provided.

7.1. Element tests

A first series of numerical simulations has been conducted on ‘‘element tests’’ imposing a homogeneous deformation to a single soil element. The complete set of element test simulations is provided in Tab. 2.

The group of 7 simulations labeled ‘‘ax’’ refer to a series of oedometric compression tests with zero radial displacement ($u_r = u_x = u_z = 0$) and axial shortening ($-u_a = -u_y$) increasing at constant rate from 0 to 30% of the reference specimen height H . In all the tests, the initial state in the reference configuration has been set to p_0 (Kirchhoff mean stress) = 200.0 kPa, q_0 (Kirchhoff deviatoric stress) = 0.0 kPa, $B_0 = D_0 = 0.0$ and $e_0 = 1.15$.

Table 1. Material constants sets for calcarenite rock adopted in the numerical simulations.

	θ^g	n_g	n_b	K^g	G^g	K^b
	[-]	[-]	[-]	[kPa]	[kPa]	[kPa]
Set 1	0.622	0.372	0.093	1.00e5	7.55e4	1.00e5
Set 2	0.622	0.372	0.093	1.00e5	7.55e4	1.00e5
Set 3	0.622	0.372	0.093	1.00e5	7.55e4	1.00e5
	G^b	M	p_t	E_{BC}	E_{DC}	ω_B
	[kPa]	[-]	[kPa]	[kJ/m ³]	[kJ/m ³]	[deg]
Set 1	7.55e4	1.62	185.2	15.0	18.0	78.0
Set 2	7.55e4	1.62	185.2	7.5	9.0	78.0
Set 3	7.55e4	1.62	185.2	15.0	9.0	78.0

Table 2. Program of single element simulations. Note: AX–SD = axisymmetric compression, small deformations; AX–FD = axisymmetric compression, finite deformations; PS–FD = plane strain compression, finite deformations; OED = oedometric compression tests; ISO = isoerror maps tests.

run no.	material	type	u_x/H	u_y/H	note
ax001	Set 1	AX–SD	0.00	-0.30	OED
ax101	Set 1	AX–FD	0.00	-0.30	OED
ax002	Set 2	AX–SD	0.00	-0.30	OED
ax102	Set 2	AX–FD	0.00	-0.30	OED
ax103a–c	Set 1 ^(*)	AX–FD	0.00	-0.30	OED
iso01 to iso06	Set 1	PS–FD	-5.0e-4	-5.0e-4÷ -1.6e-2	ISO
iso07 to iso12	Set 1	PS–FD	-1.0e-3	-5.0e-4÷ -1.6e-2	ISO
iso13 to iso18	Set 1	PS–FD	-2.0e-3	-5.0e-4÷ -1.6e-2	ISO
iso19 to iso24	Set 1	PS–FD	-4.0e-3	-5.0e-4÷ -1.6e-2	ISO
iso25 to iso30	Set 1	PS–FD	-8.0e-3	-5.0e-4÷ -1.6e-2	ISO
iso31 to iso36	Set 1	PS–FD	-1.6e-2	-5.0e-4÷ -1.6e-2	ISO

(*) Simulations performed with different values of ω_B .

Tests ax001 (small deformations, SD) and ax101 (finite deformations, FD) have been performed with material constants of Set 1 of Tab. 1. The compressibility curves obtained in the two simulations, in terms of Cauchy axial stress σ_a vs. normalized axial shortening $-u_a/H$ of the specimen, are shown in Fig. 7. The two simulations appear almost

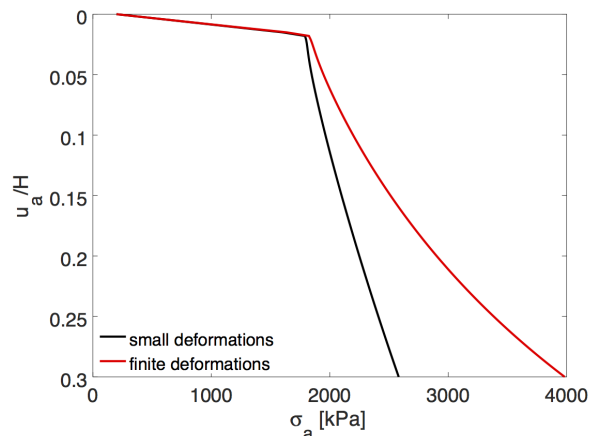


Figure 7. Oedometric compression tests ax001–ax101: compressibility curves for small and finite deformations.

coincident up to the yield point, which is reached at about 2% axial shortening. Then the two solutions rapidly diverge, the FD one showing a much larger apparent stiffness than the SD one.

Although this result is to be expected, given that in the SD setting the current configuration is always assumed coincident with the reference one, it is important to note that the differences between the two solutions are non negligible already for axial shortenings as small as 5%. This is a consequence of the collapsible nature of the calcarenite, which, due to its large porosity and the presence of intergranular bonds, is characterized by a large compressibility after yield, under isotropic or one-dimensional compression conditions. A consequence of this observation is that the calibration of the model from experimental results from tests conducted to this large levels of axial shortening would result in the overestimation of material stiffness if the prediction of the model response is made assuming linear kinematics.

The stress paths followed by the soil element during the imposed one-dimensional deformation loading are shown in the Cauchy stress invariants space in Figs. 8a,b. Note that the Cauchy stress invariants \bar{p} and \bar{q} are related to the corresponding Kirchhoff stress invariants p and q by the relations $\bar{p} = p/J$ and $\bar{q} = q/J$. In small deformations, the two quantities coincide as $J = 1$.

In both simulations, the initial (elastic) part of the stress path is linear up to the first yield point on the initial yield surface (shown in green in the figure). Afterwards, the stress path rotates clockwise up to the point on the yield surface where the plastic flow direction is consistent with the imposed kinematic constraint of zero lateral deformation. Just after the first yield, the material is almost in a neutral loading condition, then, as the stress path rotate, the plastic deformations increase substantially. Due to the purely kinematic nature of the imposed boundary conditions, the stress paths after first yield in the SD and FD simulations are not identical, as a close observation of Fig. 8 reveals. This explains why the tangent (oedometric) stiffnesses after yield are slightly

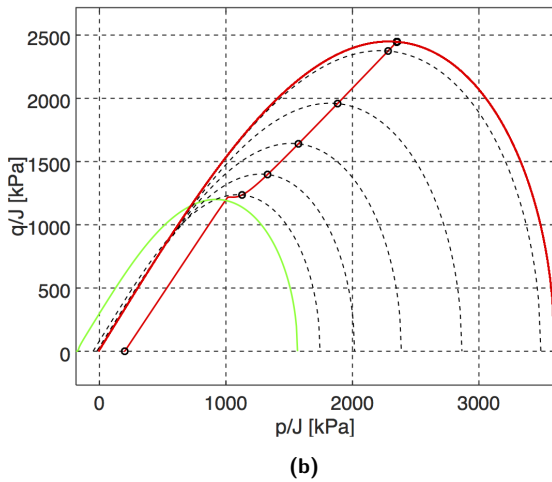
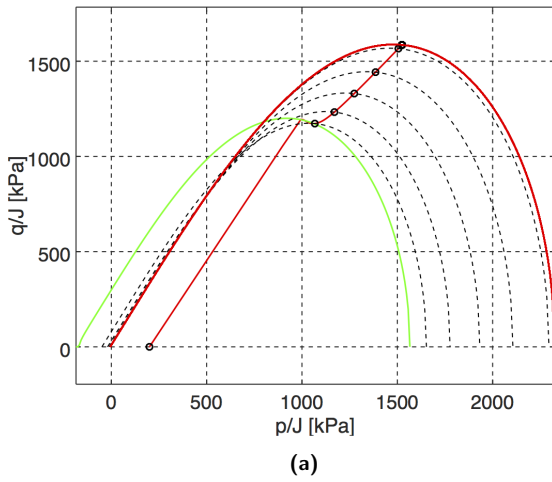


Figure 8. Oedometric compression tests ax001–ax101: stress paths for a) small deformations; b) finite deformations.

different in the two simulations. At large axial shortenings, the asymptotic K_0 condition is reached in both SD and FD simulations. The extent of the stress paths in Cauchy stress space is obviously different, with much larger mean and deviatoric stresses at the end of the test in the FD case. However, the final value of K_0 , about 0.38, is exactly the same in both cases.

The evolution of the internal variables B and D with axial shortening is shown in Fig. 9. As expected for a material with grains and bonds of the same chemical composition, bond damage and grain breakage occur simultaneously, although D increases at a much faster rate than B . Surprisingly, in this case, geometric non-linearity plays only a minor role in the grain breakage and bond damage processes.

To explore the effect of critical breakage and damage energies on the material response, the oedometric tests of simulations ax001 and ax101 have been repeated with material Set 2 (simulations ax002 and ax102 of Tab. 2), with E_{BC} and E_{DC} values reduced to 50% of those of Set 1.

The compressibility curves and the evolutions of the internal variables B and D with axial shortening for the two

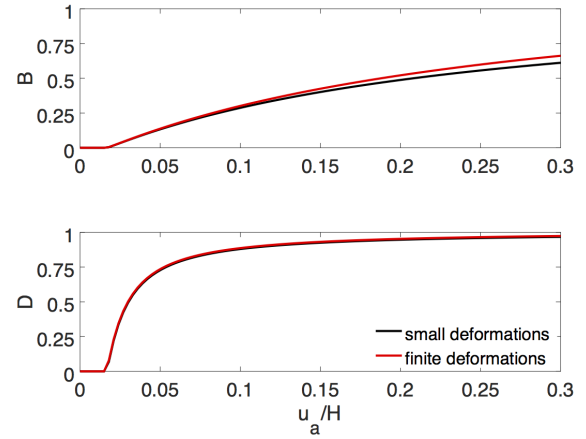


Figure 9. Oedometric compression tests ax001–ax101: evolution of breakage and damage indices for small and finite deformations.

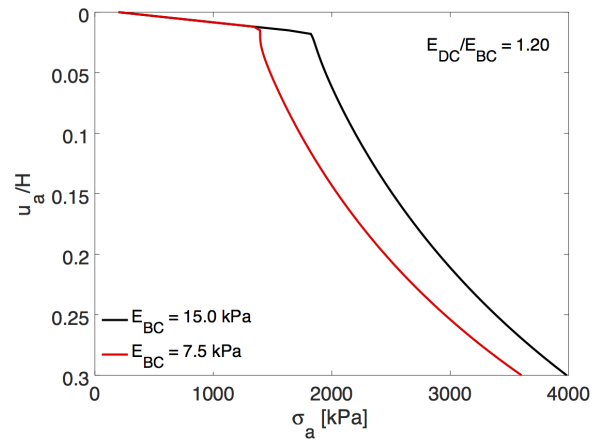


Figure 10. Oedometric compression tests ax101–ax102: effect of E_{BC} and E_{DC} on the compressibility curves.

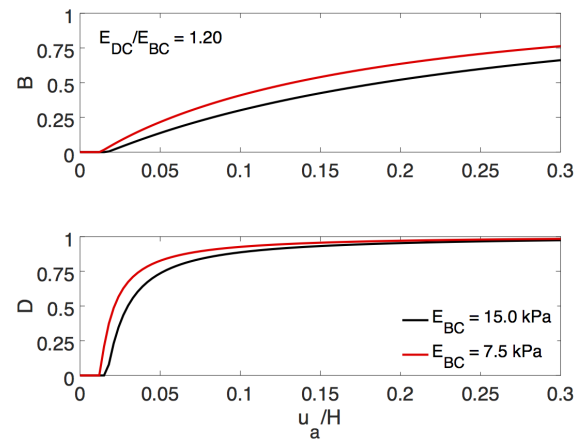


Figure 11. Oedometric compression tests ax101–ax102: effect of E_{BC} and E_{DC} on the evolution of breakage and damage indices.

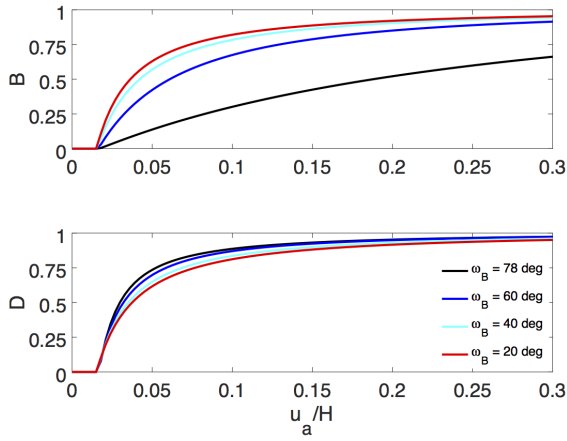


Figure 12. Oedometric compression tests ax101–ax103: effect of ω_B on the evolution of breakage and damage indices.

FD simulations ax101 and ax102 are shown in Figs. 10 and 11, respectively. By decreasing E_{BC} and E_{DC} , the size of the initial yield surface is reduced significantly (see Sect. 4.5), and at the same time, the rate at which the internal variables converge to their final asymptotic values ($B = D = 1$) is increased. In simulation ax102, the larger softening associated to a more rapid breakage of particles and damage of bonds gives rise to a very soft response after first yield, which occurs at a smaller axial stress. In this particular case, a small snap–trough effect is visible in the compressibility curve just after yield. Upon continued plastic loading, the more rapid increase of the internal state variables gives rise to a faster increase of the yield surface size as compared to the simulation ax101. This is clearly visible in the reduced slope of the one–dimensional “virgin compression” curve for simulation ax102.

Simulations ax103a,b,c have been performed with material Set 1, as ax101, but with different values of the coupling angle ω_B – equal to 60° (ax103a), 40° (ax103b) and 20° (ax103c), respectively – to explore the effect of this constant on the predicted response. As ω_B controls the relative importance of plastic volumetric compaction and grain breakage, the rate at which B converges to 1 is increased as ω_B decreases for the same amount of volumetric compaction, see Fig. 12. The change of ω_B affects also the evolution of bond damage D with material compaction, but to a much lesser extent and in the opposite way, being the rate of increase of bond damage slower for smaller values of ω_B .

Fig. 13 shows the four different compressibility curves for the different coupling angles. While ω_B has only a minor effect on the vertical stress at first yield, the post–yield stiffness of the material is strongly affected. The smaller ω_B , the larger is the increase in axial stress associated to a given increment of axial deformation. This is a consequence of the faster increase of breakage index B , which in turns controls the size of the yield locus for one–dimensional compression paths, see Fig. 2.

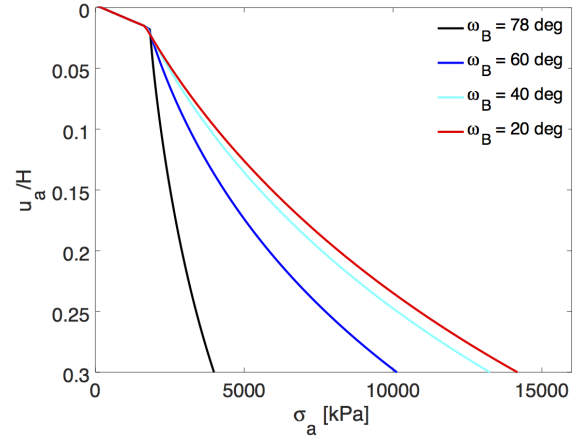


Figure 13. Oedometric compression tests ax101–ax103: effect of ω_B on the compressibility curves.

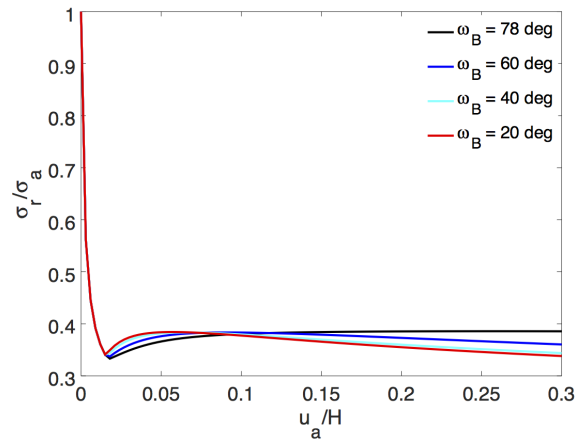


Figure 14. Oedometric compression tests ax101–ax103: effect of ω_B on the evolution of σ_r/σ_a .

The effect of ω_B on the predicted radial stress σ_r are shown in Fig. 14, in terms of stress ratio $K = \sigma_r/\sigma_a$. After the initial elastic part of the stress path, during which K decreases very fast, a subsequent small increase is observed in all the simulations, until a final steady–state value is approached for large axial shortenings. Taking these final values of K as the coefficients of earth pressure at rest K_0 , we note that as ω_B decreases, K_0 decreases as well, passing from about 0.38 for $\omega_B = 78^\circ$ to 0.34 for $\omega_B = 20^\circ$. The results in Figs. 13 and 14 indicate that the comparison between observed and predicted post–yield compression curves could be used as the main calibration criterion for ω_B , with a secondary criterion being the predicted value of K_0 .

The accuracy of the proposed integration algorithm has been evaluated by resorting to the concept of of *isoerror map*, see [Simo and Hughes, 1998, Ch. 3]. To this end 36 plane strain element simulations (iso01 to iso36) have been performed on a cubic element of size H , applying in a single step rectilinear compression paths characterized by u_x/H and u_y/H values ranging from -5.0×10^{-4} to -1.6×10^{-2} , see Tab. 2. In all the tests, the initial state in the reference configuration has been set to $\sigma_{x0} = \sigma_{z0} = 697.6$ kPa (radial Cauchy stress), $\sigma_{y0} = 1815.3$ kPa (axial Cauchy stress), $B_0 =$

0.4247, $D_0 = 0.9317$ and $e_0 = 0.8275$. This state corresponds to the plastic state reached during the oedometric test ax101 at an axial shortening of 0.15, in almost K_0 conditions.

The converged stress state $(\sigma_x, \sigma_y, \sigma_z, B, D)$ at the end of each test has been compared to the “exact” solution $(\sigma_x^*, \sigma_y^*, \sigma_z^*, B^*, D^*)$ to define the following error measures:

$$\text{ERR}_\sigma = \frac{\|\hat{\boldsymbol{\sigma}} - \hat{\boldsymbol{\sigma}}^*\|}{\|\hat{\boldsymbol{\sigma}}^*\|} \quad \text{ERR}_q = \frac{\|\mathbf{q} - \mathbf{q}^*\|}{\|\mathbf{q}^*\|}$$

where:

$$\hat{\boldsymbol{\sigma}} = \begin{Bmatrix} \sigma_x \\ \sigma_y \\ \sigma_z \end{Bmatrix} \quad \hat{\boldsymbol{\sigma}}^* = \begin{Bmatrix} \sigma_x^* \\ \sigma_y^* \\ \sigma_z^* \end{Bmatrix} \quad \mathbf{q} = \begin{Bmatrix} B \\ D \end{Bmatrix} \quad \mathbf{q}^* = \begin{Bmatrix} B^* \\ D^* \end{Bmatrix}$$

Note that the need to distinguish between the errors in the stress and internal variables update originates from the different units of $\hat{\boldsymbol{\sigma}}$ and \mathbf{q} . In lack of a true exact solution for the state update of the imposed deformation paths, the reference “exact” solutions have been computed repeating each simulations with 100 steps.

Figs. 15 shows the contour maps of ERR_σ and ERR_q in the $-\ln(1/\lambda_x)$ vs. $-\ln(1/\lambda_y)$ plane, where $\lambda_x = 1 + u_x/H$ and $\lambda_y = 1 + u_y/H$ are the principal stretches in x and y directions, respectively. The data in the two figures show the good accuracy properties of the algorithm. The error in the updated stress state (Fig. 15a) reaches a maximum of 5% for the strain path with the maximum extension (iso36 test), at about 2% nominal strain norm. Is worth noting that, at the same strain path extension, the accuracy increases when the strain path is characterized by one of the two stretches prevailing on the other. The error in the updated internal variables (Fig. 15b) is much smaller, with a maximum value of 0.08%.

The efficiency of the stress point algorithm for plastic processes can be assessed by the convergence rate of the local Newton algorithm detailed in Appendix C. Fig. 16 shows the convergence profiles for the yield function y^* and the residuals $R_\varepsilon := \|\mathbf{r}^\varepsilon\|$ and $R_q := \sqrt{(r^B)^2 + (r^D)^2}$, see eq. (139) of Appendix C, as computed in the one-step simulations iso06, iso31 and iso36. These three tests have been chosen as they are characterized by: maximum λ_x and minimum λ_y ; minimum λ_x and maximum λ_y , and minimum λ_x and λ_y , respectively. The tolerance limits adopted for y^* , R_ε and R_q are indicated in each plot with a dashed line.

For all the three residuals, the profiles show a very fast – almost quadratic – convergence, with the assumed tolerances reached in maximum 5 iterations. Of the three convergence criteria which control the iteration procedure, those on y^* and R_ε require more iterations to be met, while the residual R_q drops very fast to very low values after just three iterations. The convergence for test iso31 is much faster than for the other tests, as in this case the trial stress state is much closer to the yield surface at the beginning of the step, see the value of y^* at iteration 0 (initialization).

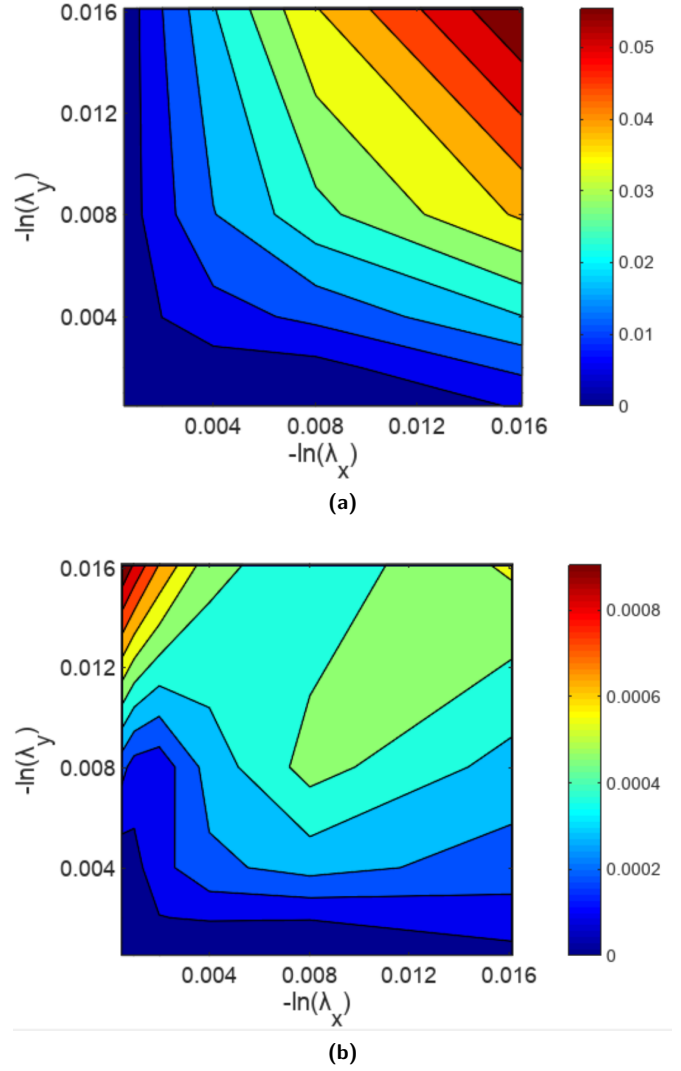
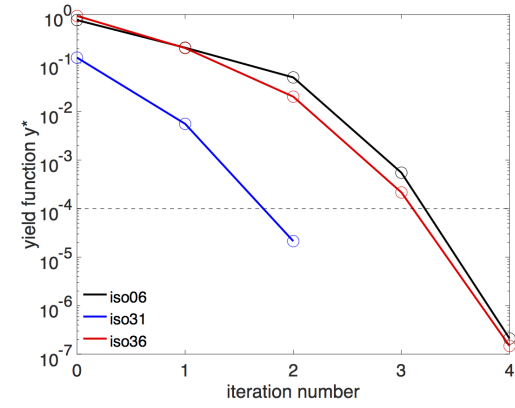


Figure 15. Isoerror maps: a) ERR_σ ; b) ERR_q .

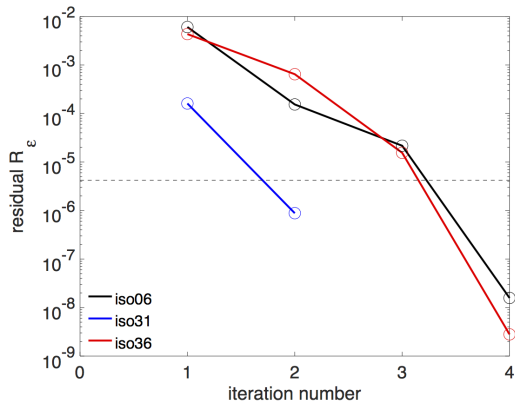
7.2. Plane strain compression tests

As an example of application to a boundary value problem, a second group of simulations has been carried out to model the “structural” response of a specimen of calcarenite subjected to plane strain compression tests. In this case, the objective is to assess the possibility that the solution may bifurcate from the ideal homogeneous deformation path, i.e., by strain localization into shear band. This possibility has been explored, in the context of linearized kinematics, by Das et al. [2014]. By adopting a finite deformation formulation, our goal is to assess the effects of non-linear kinematics on the bifurcation mode of the solution, if any.

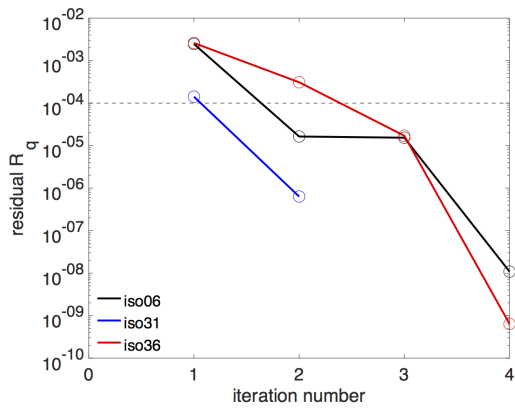
The layout of the plane strain tests has been taken from the experimental device adopted by Finno et al. [1997] and used in many others experimental works focused on the study of shear localization in geomaterials. The geometry of the specimen, of height $H = 140$ mm and width $B = 40$ mm in the plane of deformation, is shown in Fig. 17. The specimen is confined between two horizontal, rigid and perfectly smooth platens (ab and dc) and subjected to a



(a)



(b)



(c)

Figure 16. Convergence profiles for simulations iso06, iso31 and iso36: a) yield function y^* ; b) residual R_ϵ ; c) residual R_q .

uniform, constant pressure σ_{x0} on the lateral boundaries ad and bc. To prevent rigid translations in x direction, the horizontal displacement has been fixed at the individual node a, at the origin of the reference frame.

The initial state of the material has been assigned as follows. The initial Cauchy stress state has been assumed isotropic, with $\bar{p}_0 = \sigma_{x0}$ equal to two different values, namely 200 kPa (low confining stress) and 1200 kPa (high

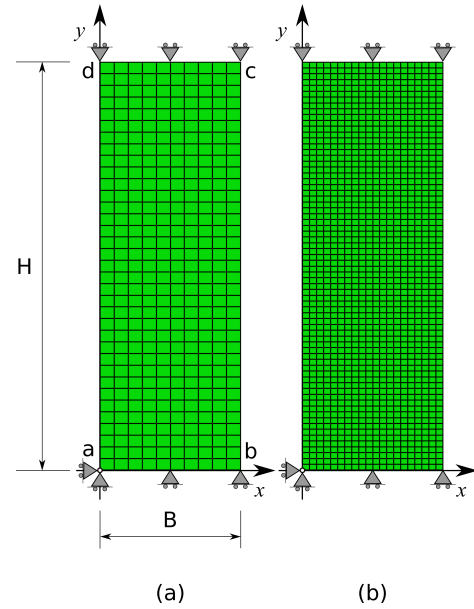


Figure 17. Biaxial tests: problem geometry and finite element discretizations adopted. a) Coarse mesh, 10×35 Q4 elements; b) fine mesh, 20×70 Q4 elements.

confining stress). In order to trigger the onset of (possible) bifurcated solutions, the initial breakage and damage indices have been assigned a spatially uncorrelated Gaussian distribution within the domain, with an average value $\mu = 0.01$ and a coefficient of variation $CoV = 20\%$ for both variables. The value of the CoV adopted guarantees that no unphysical, negative values for B and D are generated.

The plane strain compression tests are simulated by imposing negative vertical displacements to the top rigid platen, up to a minimum values of -15 mm for low confining stress tests and -30 mm for high confining stress tests.

In order to detect a possible mesh-dependence on the test results, two different discretizations have been adopted: a relatively coarse one, with 350 bilinear Q4 elements (Fig. 17a) and a finer one, with 1400 bilinear Q4 elements (Fig. 17b). The complete program of plane strain simulations is provided in Tab. 3.

The response of the specimens to an imposed rectilinear displacement u_y along the axial direction y is shown in Fig. 18 for low confining stress tests and in Fig. 22 for high confining stress. In the figures, the global response of the specimen, as provided by external displacement and load transducers in real experiments, is provided in terms of axial load increment $\Delta F_y := F_y - F_{y0}$ (F_{y0} being the axial load at the end of the isotropic compression stage) vs. the normalized axial shortening $-u_y/H$.

For the low confining stress case, the results in Fig. 18 show that the predictions obtained in small and finite deformations are practically coincident up to the peak failure at first yield, occurring at an axial shortening of about 1.2%. After the peak, the SD and FD predictions diverge significantly, with the axial load remaining almost constant in the SD simulation while it experiences a substantial reduction in the FD case. It is worth noting that these observations are

Table 3. Program of plane strain simulations. Note: SD = small deformations; FD = finite deformations.

run no.	material	type	mesh	σ_{x0}	u_y/H
bx001	Set 3	SD	coarse	200.0	-0.107
bx101	Set 3	FD	coarse	200.0	-0.075(*)
bx002	Set 3	SD	coarse	1200.0	-0.214
bx102	Set 3	FD	coarse	1200.0	-0.214
bx003	Set 3	SD	fine	200.0	-0.061(*)
bx103	Set 3	FD	fine	200.0	-0.044(*)
bx004	Set 3	SD	fine	1200.0	-0.214
bx104	Set 3	FD	fine	1200.0	-0.214

(*) Simulations terminated earlier due to lack of convergence in the global equilibrium iteration.

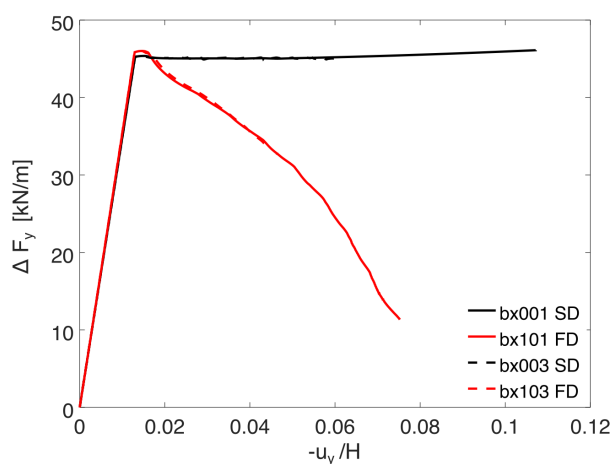


Figure 18. Biaxial tests at low confining stress: axial load increment ΔF_y vs. normalized axial shortening $-u_y/H$.

independent of the mesh size, as the solutions obtained with the coarse and fine meshes are almost coincident for the entire range of $-u_y/H$. The simulations r003, r101, and r103 do not reach the prescribed maximum shortening due to a lack of convergence of the global equilibrium iteration.

The reason for the large impact of non-linear kinematics on the post-peak response of the specimens can be found by observing the evolution with time of material displacements, internal variables and void ratio. Such information is provided by Figs. 19–21, where the displacements are represented through the deformed configurations of the specimen at real scale (magnification factor set to 1), while B , D and e are shown as contour maps. In the figure, four different time stations have been considered, each corresponding to a characteristic level of axial shortening – (a) to (d) – identified on the load–displacement curves (shown in a inset) with full circles. The top four contour maps refer to the

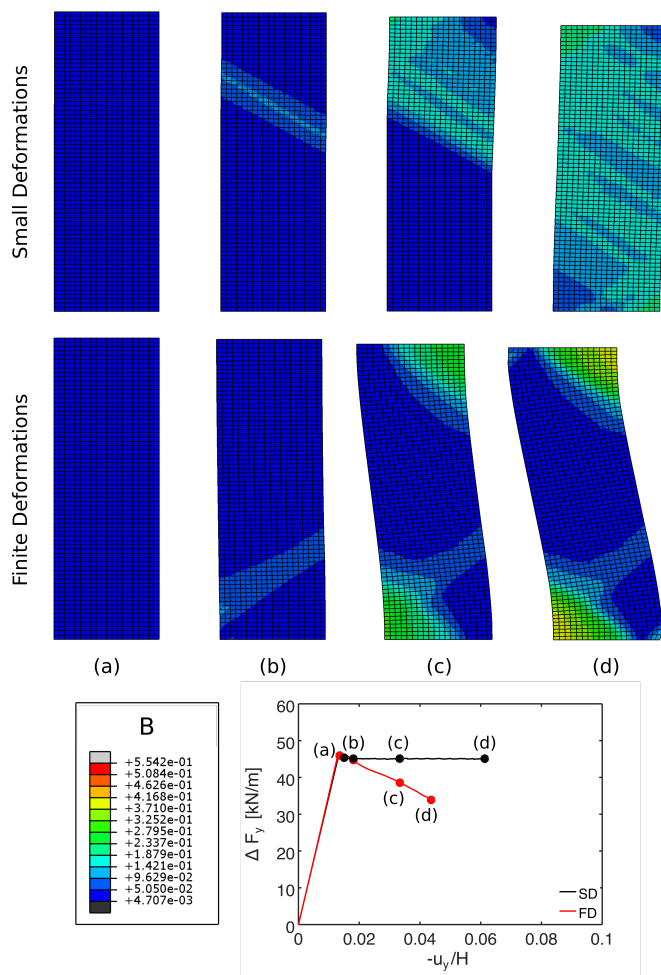


Figure 19. Biaxial tests bx003 and bx103: Contour maps of breakage index B at different time stations.

SD simulation, while the bottom ones to the corresponding FD simulation.

As far as the SD predictions are concerned, it can be clearly seen that, at peak – time station (a) – the specimen is deforming homogeneously, except for some small variations in D (see Fig. 20, top). Soon after reaching the peak – time station (b) – the formation of a compactant shear band is observed in the upper part of the specimen, with a localized increase in grain crushing and bond damage. As the axial displacement of the top platen progresses – time station (c) – the deformation within the specimen tend to spread through its upper part, rather than concentrating on the initial localized zone. This spread can be seen as the coalescence of a number of secondary parallel bands, as in Fig. 19 for the variable B , or the progressive spread of the initial band towards the top of the specimen, as in Figs. 20 (for D) and 21 (for e). Finally, at time station (d), the distribution of all the three fields B , D and e is again almost homogeneous, although the deformed shape of the specimen is affected by the irreversible shear strains accumulated in the previous stages.

The spreading of the localized zone to the initially less deformed parts of the specimen is most likely caused by the

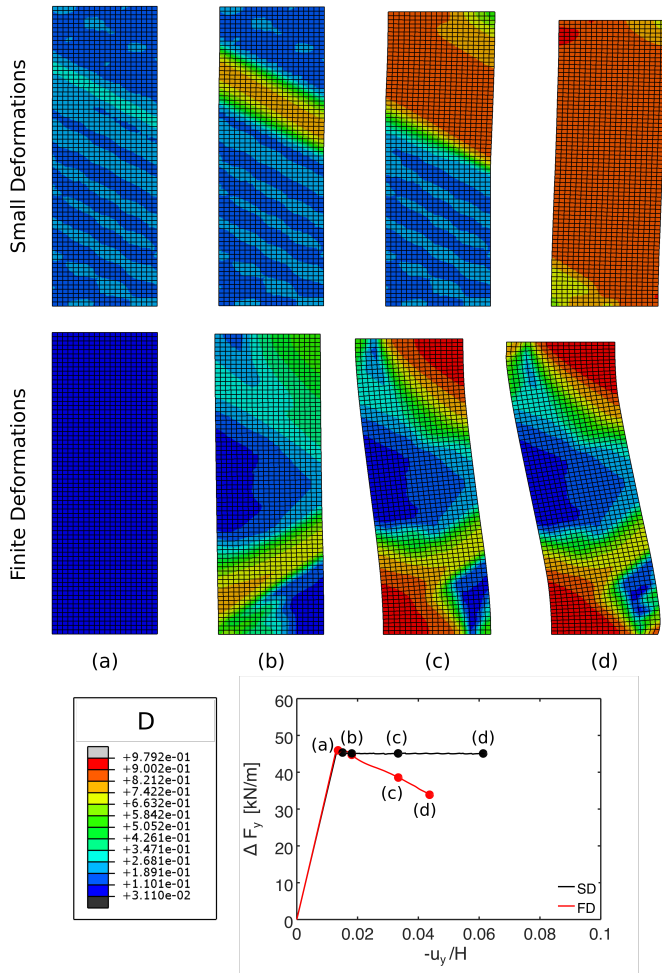


Figure 20. Biaxial tests bx003 and bx103: Contour maps of damage index D at different time stations.

relatively ductile behavior of the material, even at a confining stress as low as 200 kPa. The fact that no strong gradients of displacements or state variables have been developed during the entire test explains the mesh insensitivity of the solution.

If we now consider the corresponding FD predictions, reported at the bottom rows of the same figures, we note that as far as time stations (a) and (b) are concerned, the pattern of behavior of the specimen is pretty similar the one observed in the SD simulations. The deformation is homogeneous up to time station (a) and start to localize into a shear band in (b). In this case, the band is originating in the lower part of the specimen, with a different (conjugate) orientation, and the same average inclination. However, as the test progresses – time stations (c) and (d) – the mode of deformation of the specimen changes radically from the SD case. The initial offset to the left of the top platen with respect to the base at stage (b) triggers a buckling deformation in the slender specimen, clearly visible in its deformed shape. At this point, this mode of deformation prevails over the initial shear band mode. The shear band remains locked in its original position, and is progressively shadowed by the buckling deformation mode.

The emergence of the buckling mode in the post-peak regime is responsible for the strong decrease observed in the axial load as specimen shortening progresses. This mode cannot emerge in the SD setting since, in this case, the deformed configuration at each step is assumed coincident to the (symmetric) reference one.

For the high confining stress case, the load–displacement curves are shown Fig. 22. The predictions obtained in small and finite deformations are again coincident up to the first yield point, which is now attained at much smaller axial shortening and axial load increment. Subsequently, while the SD prediction shows a monotonic increase of axial load with specimen shortening, the FD prediction is characterized by a small peak, followed by an almost constant F_y value and then by a subsequent strong decrease of the axial load up to the (large) final imposed shortening value. As in the small confining stress case, the load–deformation curves are independent of the mesh size, as the solutions obtained with the coarse and fine meshes are almost coincident for the entire range of $-u_y/H$.

Again, the reason for the large impact of non-linear kinematics on the load–displacement response of the specimens can be found by observing the evolution with time of material displacements, internal variables and void ratio. Such

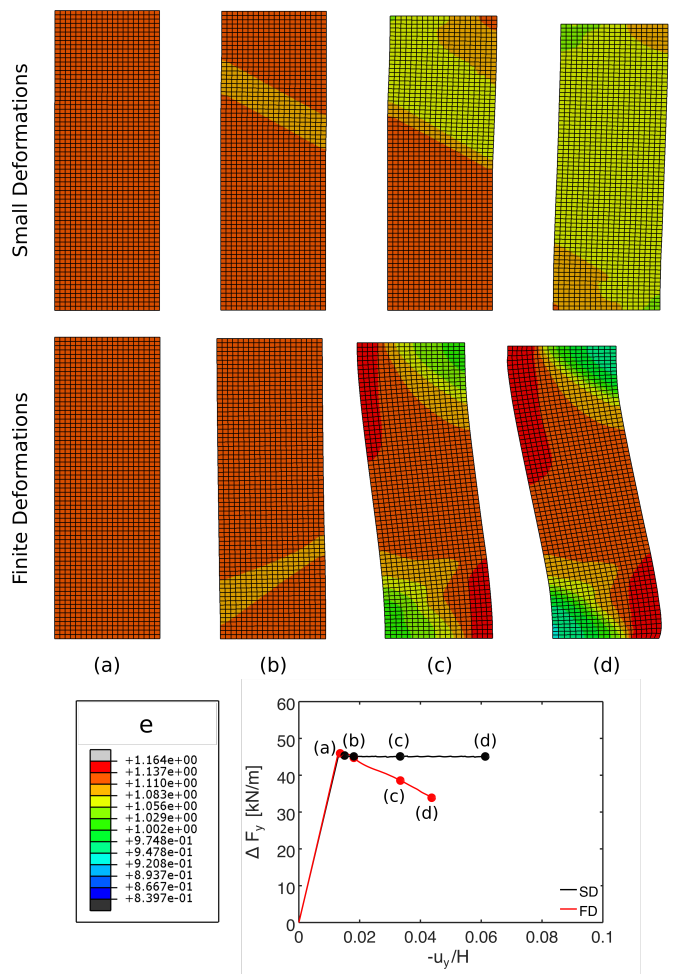


Figure 21. Biaxial tests bx003 and bx103: Contour maps of void ratio e at different time stations.

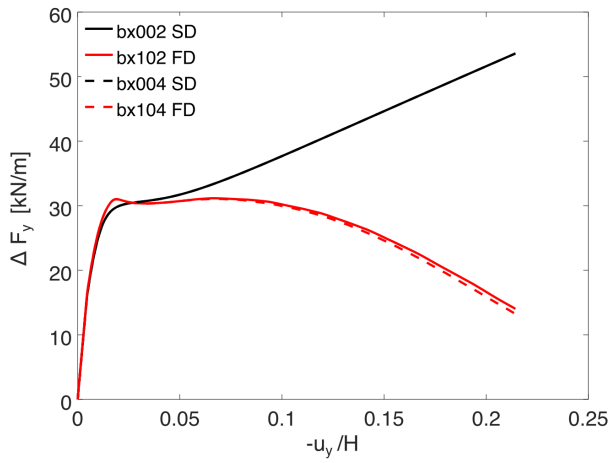


Figure 22. Biaxial tests at high confining stress: axial load increment ΔF_y vs. normalized axial shortening $-u_y/H$.

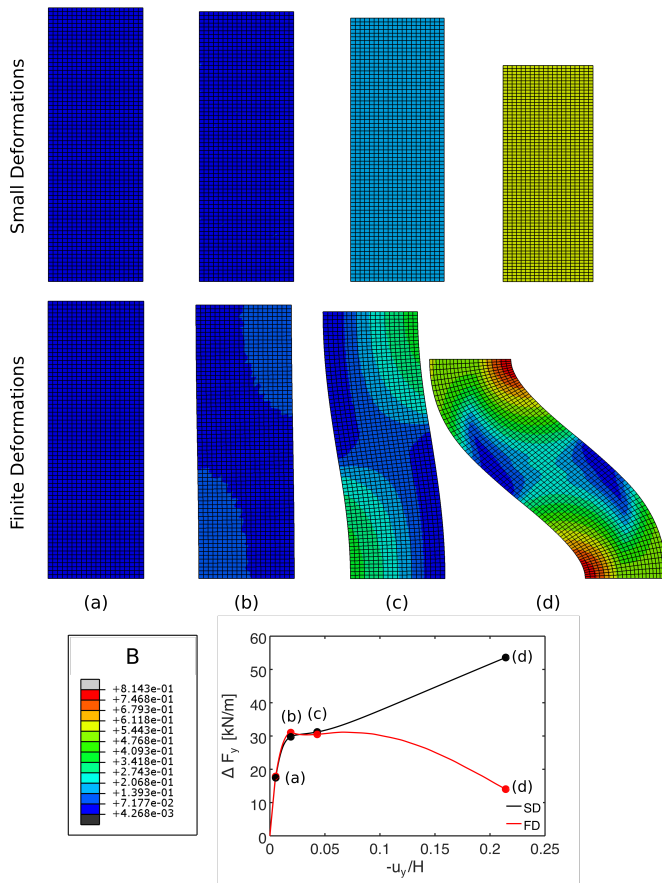


Figure 23. Biaxial tests bx004 and bx104: Contour maps of breakage index B at different time stations.

information is provided by Figs. 23–25, where, as before, the displacements are represented through the deformed configurations of the specimen at real scale (magnification factor set to 1), while B , D and e are shown as contour maps.

Looking at the results of the SD predictions, the specimen deforms homogeneously throughout the entire test, up to

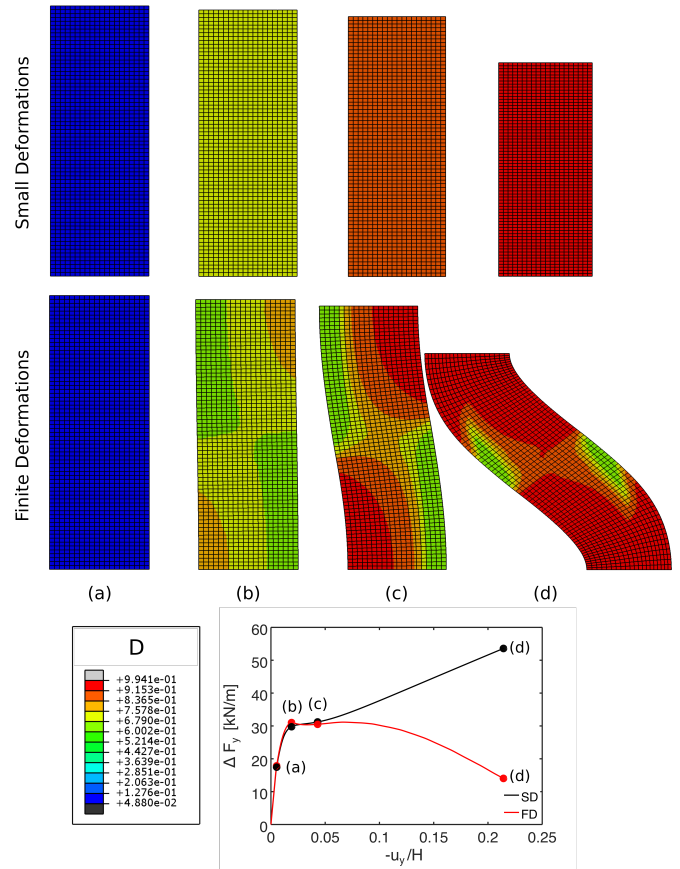


Figure 24. Biaxial tests bx004 and bx104: Contour maps of damage index D at different time stations.

the maximum applied axial shortening, in spite of the initial small random heterogeneity introduced in the initial conditions for B and D . In fact, at the high initial stress level considered in this test, the conditions for the bifurcation of equilibrium into a shear band localized mode are unlikely to occur and the initial heterogeneity is quickly erased by the ductile response of the material. Given the “ideal” displacement boundary conditions imposed at the top and bottom platens, the same results of this test – plotted in terms of homogeneous stress and strain quantities – would have been obtained in a single element test.

This is not the case for the FD simulation, in which the specimen deforms homogeneously only up to the first yield point at time station (a). Then, as soon as plastic deformations start to develop – time station (b) – the specimen shows a tendency to buckle leftwards, clearly visible in the map of the bond damage index D of Fig. 24. As the axial shortening increases – time stations (c) and (d) – the specimen buckles leftwards, showing no sign of strain localization, while the axial load decreases as a consequence of the significant horizontal displacements experienced by the upper loading plate.

The occurrence of buckling in the FD regime is the consequence of a bifurcation of equilibrium around time station (b), upon which the system abandons the homogeneous rectilinear compression solution for the more stable buckled one. The non-linear kinematics is essential for this

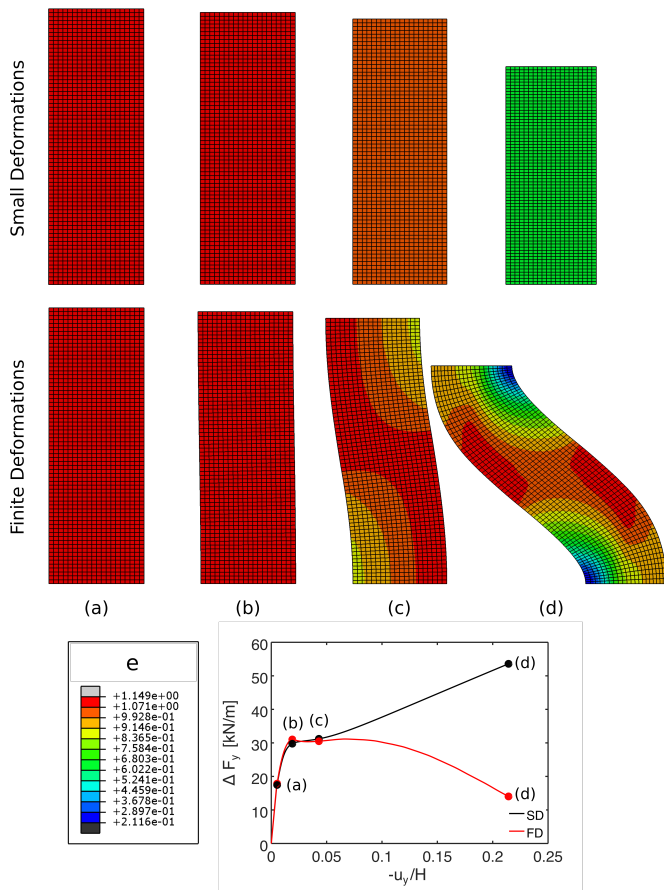


Figure 25. Biaxial tests bx004 and bx104: Contour maps of void ratio e at different time stations.

phenomenon to be captured correctly, as evidenced by the comparison between the SD and FD solutions.

It is interesting to note that the choice of the solution among the possible alternatives occurring at bifurcation might be determined by the small random “perturbations” introduced in the initial internal variables fields. In fact, by comparing the results of Fig. 25 with those of Fig. 26, which refers to the coarse mesh prediction of the same test – performed with a different random initialization of B and D – the most striking observation is that, in this latter case, the buckling of the specimen occurs rightward, i.e., in the direction opposite to the one observed with the fine mesh. Quite surprisingly, this drastic difference in the deformation patterns of the specimens has almost no effect on the global load–displacement curve and on the spatial distributions of the void ratio.

8. Concluding remarks

In this work, the theory of isotropic hyperplasticity with micromechanically–inspired internal variables, originated from Einav’s breakage mechanics and subsequent modifications, has been extended to the finite deformation setting in order to deal with the behavior typically observed in natural granular materials such as cemented soils and soft arenaceous rocks, when subject to mechanical degradation processes. The open, highly porous microstructure of such

materials can be responsible for the occurrence of high volumetric and shear strains, as soon as, after first yield, the breakage of intergranular bonds and the comminutions of the grains give rise to a significant irreversible reduction of the solid skeleton porosity.

As in recent applications of finite deformation plasticity to geomechanics, the formulation of the theory is based on a multiplicative split of the deformation gradient into an elastic and a plastic deformation gradient. However, differently from all the works originated from the finite deformation plasticity theory proposed by Simo [1992] – based on the principle of maximum dissipation – the present approach does not prevent the possibility of modeling non–associative plastic flow in Kirchhoff or Cauchy stress spaces. As an example of application of the general theory to a specific class of natural geomaterials, an isotropic hardening model for porous calcarenite rocks has been proposed which can be considered the finite deformation counterpart of the small–strain model of Tengattini et al. [2014] and Das et al. [2014], with some minor, but important, modifications on the free energy and dissipation functions adopted.

In view of the practical application of the model to actual geotechnical engineering problems, an important contribution of the work is represented by the development of a numerical integration algorithm for its implementation into general purpose finite element platforms. The proposed algorithm is a fully implicit Backward Euler scheme based on the concepts of operator split and exponential mapping,

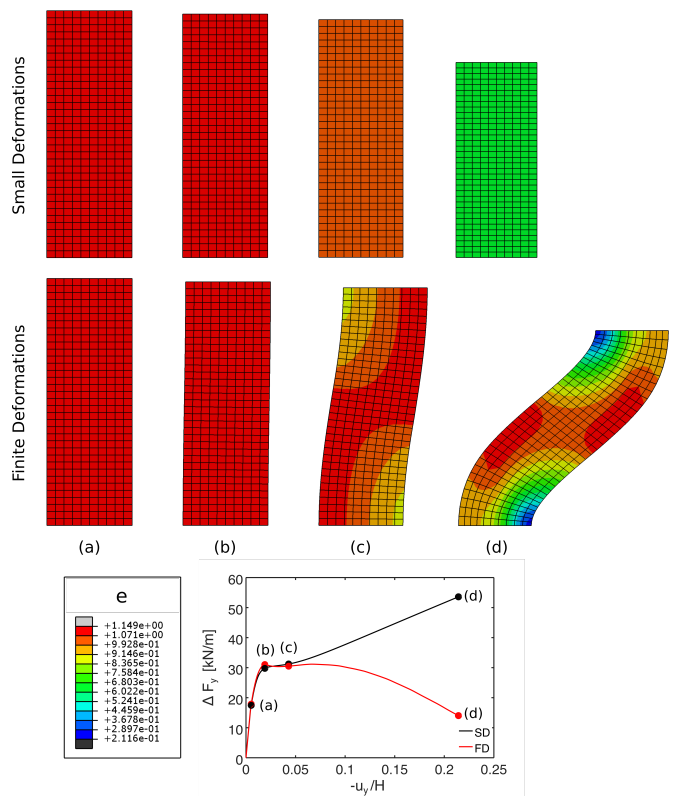


Figure 26. Biaxial tests bx002 and bx102: Contour maps of void ratio e at different time stations, coarse mesh.

which, when formulated in logarithmic principal elastic strain space possesses the same algebraic structure of the classical elastic predictor–plastic corrector schemes of infinitesimal plasticity. In addition, the algorithm has been linearized in closed form, to allow the computation of the consistent tangent stiffness matrix to be used in the global Newton iteration scheme in order to achieve quadratic convergence.

A series of single element tests have demonstrated the accuracy and efficiency of the proposed integration scheme, and have highlighted the role played by some of the material constants in determining the material response under simple, yet very important loading paths. The finite element simulation of two different plane strain biaxial tests, modeled as boundary–value problems, has allowed to identify the importance of the kinematic setting in determining the evolution of the specimen deformation upon reaching a bifurcation condition. At small confining stress, the small deformation simulation is characterized by localization of strains into shear bands, while the finite deformation simulation switches very early to a buckling mode. At large confining stress, the small deformation simulation remains perfectly homogeneous, while buckling again occurs as soon as plastic deformations occur in the finite deformation case. It is important to stress that non–linear kinematics is essential to capture the buckling modes, since the deformed configuration and the (symmetric) reference one are assumed coincident in the small deformation approximation. This aspect could be of importance not only in the interpretation of laboratory test results – as in this case – but also in practical applications where strong geometric non–linearity effects could be foreseen, e.g., in the study of the stability of tall structures with a relatively high center of gravity, in presence of significant second–order ($P - \Delta$) effects.

Finally, it should be noted that significant volumetric strains of non–mechanical origin could be induced in dissolution–prone granular materials – such as calcarenite rocks – in presence of weathering processes involving grain and bond dissolution. The extension of this work to incorporate such degradation processes, of relevance in a number of geotechnical applications including CO₂ sequestration in depleted carbonatic reservoirs, is currently under study and will be the subject of a forthcoming work.

Conflicts of Interest

The Authors have no conflict of interest.

Acknowledgements

The authors would like to thank Dr. Alessandro Tengattini, Dr. Matteo O. Ciantia, Prof. Gioacchino Viggiani and Prof. Itai Einav for many fruitful discussions on different aspects of this work. K.O. gratefully acknowledge the financial support of the grant “Constitutive modeling of mechanical and chemical degradation processes in cemented soils and weak rocks in the framework of the theory of hyperplasticity in finite deformations” of the Dept. of Civil and Environmental

Engineering of the University of Perugia. C.T. gratefully acknowledge the financial support of the Project Tec21 (2017) “Multiscale investigation and modeling of coupled chemo–hydro–mechanical degradation processes in carbonatic soft rocks”. The complete review history is available online.

References

- Airey, D. W. (1993). Triaxial testing of naturally cemented carbonate soil. *J. Geotech. Engng., ASCE*, 119(9):1379–1398.
- Aversa, S. and Evangelista, A. (1998). The mechanical behaviour of a pyroclastic rock: yield strength and “destruction” effects. *Rock Mechanics and Rock Engineering*, 31(1):25–42.
- Bianchi Fasani, G., Bozzano, F., and Cercato, M. (2011). The underground cavity network of south-eastern Rome (Italy): an evolutionary geological model oriented to hazard assessment. *Bulletin of Engineering Geology and the Environment*, 70(4):533–542.
- Borja, R. I. (2013). *Plasticity: Modeling & Computation*. Springer Science & Business.
- Borja, R. I., Sama, K. M., and Sanz, P. F. (2003). On the numerical integration of three-invariant elastoplastic constitutive models. *Comp. Meth. Appl. Mech. Engng.*, 192(9–10):1227–1258.
- Borja, R. I. and Tamagnini, C. (1998). Cam–clay plasticity, part III: Extension of the infinitesimal model to include finite strains. *Comp. Meth. Appl. Mech. Engng.*, 155:73–95.
- Callari, C., Auricchio, E., and Sacco, E. (1998). A finite-strain cam-clay model in the framework of multiplicative elastoplasticity. *Int. J. of Plasticity*, 14(12):1155–1187.
- Cecconi, M., DeSimone, A., Tamagnini, C., and Viggiani, G. M. B. (2002). A constitutive model for granular materials with grain crushing and its application to a pyroclastic soil. *Int. J. Num. Anal. Meth. Geomech.*, 26(15):1531–1560.
- Cecconi, M. and Viggiani, G. M. B. (2001). Structural features and mechanical behaviour of a pyroclastic weak rock. *Int. J. Num. Anal. Meth. Geomech.*, 25(15):1525–1557.
- Ciantia, M., Castellanza, R., and di Prisco, C. (2014). Experimental study on the water-induced weakening of calcarenites. *Rock Mechanics and Rock Engineering*, 48(2):441–461.
- Ciantia, M. O., Castellanza, R., Crosta, G. B., and Hueckel, T. (2015). Effects of mineral suspension and dissolution on strength and compressibility of soft carbonate rocks. *Engineering Geology*, 184:1–18.
- Ciantia, M. O. and di Prisco, C. (2016). Extension of plasticity theory to debonding, grain dissolution, and chemical damage of calcarenites. *Int. J. Num. Anal. Meth. Geomech.*, 40(3):315–343.
- Ciantia, M. O. and Hueckel, T. (2013). Weathering of stressed submerged calcarenites. *Géotechnique*, 63:768–785.
- Collins, I. and Housby, G. T. (1997). Application of thermomechanical principles to the modeling of geotechnical materials. *Proc. Royal Soc. London Series A*, 453:1975–2000.
- Collins, I. and Muhunthan, B. (2003). On the relationship between stress–dilatancy, anisotropy, and plastic dissipation for granular materials. *Geotechnique*, 53(7):611–618.

- Collins, I. F. (2003). A systematic procedure for constructing critical state models in three dimensions. *Int. Journal of Solids and Structures*, 40(17):4379–4397.
- Collins, I. F. and Hilder, T. (2002). A theoretical framework for constructing elastic/plastic constitutive models of triaxial tests. *Int. J. Num. Anal. Meth. Geomech.*, 26(13):1313–1347.
- Collins, I. F. and Kelly, P. A. (2002). A thermomechanical analysis of a family of soil models. *Géotechnique*, 52(7):507–518.
- Coop, M. and Atkinson, J. (1993). The mechanics of cemented carbonate sands. *Geotechnique*, 43(1):53–67.
- Coop, M. R. (1990). The mechanics of uncemented carbonate sands. *Géotechnique*, 40(4):607–626.
- Cuccovillo, T. and Coop, M. R. (1999). On the mechanics of structured sands. *Géotechnique*, 49(6):741–760.
- Das, A., Tengattini, A., Nguyen, G. D., Viggiani, G., Hall, S. A., and Einav, I. (2014). A thermomechanical constitutive model for cemented granular materials with quantifiable internal variables. Part II – Validation and localization analysis. *Journal of the Mechanics and Physics of Solids*, 70:382–405.
- de Souza Neto, E. A., Peric, D., and Owen, D. R. J. (2011). *Computational methods for plasticity: theory and applications*. John Wiley & Sons.
- DeSimone, A. and Tamagnini, C. (2005). Stress–dilatancy based modelling of granular materials and extensions to soils with crushable grains. *Int. J. Num. Anal. Meth. Geomech.*, 29(1):73–101.
- Einav, I. (2007a). Breakage mechanics – Part I: theory. *JMPS*, 55(6):1274–1297.
- Einav, I. (2007b). Breakage mechanics – Part II: Modelling granular materials. *JMPS*, 55(6):1298–1320.
- Einav, I., Houlsby, G. T., and Nguyen, G. D. (2007). Coupled damage and plasticity models derived from energy and dissipation potentials. *Int. Journal of Solids and Structures*, 44(7-8):2487–2508.
- Einav, I. and Puzrin, A. M. (2004). Continuous hyperplastic critical state (chcs) model: derivation. *Int. Journal of Solids and Structures*, 41(1):199–226.
- Evangelista, A., Aversa, S., Pescatore, T. S., and Pinto, F. (2000). Soft rocks in southern italy and role of volcanic tuffs in the urbanization of naples. In *Proceedings of the II International Symposium on The Geotechnics of Hard Soils and Soft Rocks*, volume 3, pages 1243–1267, Naples, Italy.
- Finno, R. J., Harris, W. W., Mooney, M. A., and Viggiani, G. (1997). Shear bands in plane strain compression of loose sand. *Géotechnique*, 47(1):149–165.
- Fish, J. (2014). *Practical multiscale*. John Wiley & Sons.
- Gajo, A. and Wood, D. M. (1999). A kinematic hardening constitutive model for sands: the multiaxial formulation. *Int. J. Num. Anal. Meth. Geomech.*, 23:925–965.
- Gens, A. and Nova, R. (1993). Conceptual bases for a constitutive model for bonded soils and weak rocks. In Anagnostopoulos, A., Schlosser, F., Kalteziotis, N., and Frank, R., editors, *Geotechnical Engineering of Hard Soils–Soft Rocks*, Athens, Greece. Balkema, Rotterdam.
- Germain, P., Nguyen, Q. S., and Suquet, P. (1983). Continuum thermodynamics. *J. Appl. Mechanics, ASME*, 50:1010–1020.
- Halphen, B. and Nguyen, Q. S. (1975). Sur les matériaux standards généralisés. *Journal de Mécanique*, 14:39–63.
- Han, W. and Reddy, B. D. (1999). *Plasticity: Mathematical Theory and Numerical Analysis*. Springer Verlag, New York.
- Houlsby, G. T. (1981). *A study of plasticity theories and their applicability to soils*. PhD thesis, Cambridge University.
- Houlsby, G. T. (2019). Frictional plasticity in a convex analytical setting. *Open Geomechanics*, 1:1–10.
- Houlsby, G. T. and Puzrin, A. M. (2000). A thermomechanical framework for constitutive models for rate-independent dissipative materials. *Int. J. of Plasticity*, 16(9):1017–1047.
- Houlsby, G. T. and Puzrin, A. M. (2007). *Principles of hyperplasticity: an approach to plasticity theory based on thermodynamic principles*. Springer Science & Business Media.
- Hughes, T. J. R. (1984). Numerical implementation of constitutive models: rate-independent deviatoric plasticity. In Nemat-Nasser, S., Asaro, R., and Hegemier, G., editors, *Theoretical Foundations for Large Scale computations of Non Linear Material Behavior*, pages 29–57, Horton, Greece. Martinus Nijhoff Publisher, Dordrecht.
- Jardine, R. J., Buckley, R. M., Kontoe, S., Barbosa, P., and Schroeder, F. C. (2018). Behaviour of piles driven in chalk. *Engineering in chalk*, pages 33–51.
- Kavvas, M. (1994). On the mechanical behavior of bonded soils. In *Proc. COMETT Seminar on Large Excavations*, Bruxelles, Belgium.
- Kavvas, M., Anagnostopoulos, A., and Kalteziotis, N. (1993). A framework for the mechanical behavior of cemented corinth marl. In Anagnostopoulos, A., Schlosser, F., Kalteziotis, N., and Frank, R., editors, *Geotechnical Engineering of Hard Soils–Soft Rocks*, volume 1, pages 577–583, Athens, Greece. Balkema, Rotterdam.
- Kikumoto, M., Wood, D. M., and Russell, A. (2010). Particle crushing and deformation behaviour. *Soils and foundations*, 50(4):547–563.
- King, R. and Lodge, M. (1988). North west shelf development-the foundation engineering challenge. In *International conference on calcareous sediments*, pages 333–341.
- Lagioia, R. and Nova, R. (1995). An experimental and theoretical study of the behavior of a calcarenite in triaxial compression. *Géotechnique*, 45(4):633–648.
- Lee, E. H. (1968). Elastic-plastic deformation at finite strains. *J. Appl. Mechanics, ASME*, 36:1–6.
- Liu, M. D. and Carter, J. P. (2002). A structured cam clay model. *Can. Geotech. J.*, 39(6):1313–1332.
- Maugin, G. A. (1992). *Thermomechanics of plasticity and fracture*. Cambridge University Press.
- McLelland, B. (1988). Calcareous sediments: an engineering enigma. In *International conference on calcareous sediments*, pages 777–784.
- Modaresi, L., Laloui, L., and Aubry, D. (1994). Thermodynamical approach for camclay–family models with

- roscoe-type dilatancy rules. *Int. J. Num. Anal. Meth. Geomech.*, 18:133–138.
- Monforte, L., Ciantia, M. O., Carbonell, J. M., Arroyo, M., and Gens, A. (2019). A stable mesh-independent approach for numerical modelling of structured soils at large strains. *Comp. & Geotechnics*, 116:103215.
- Moreau, J. J. (1970). Sur les lois de frottement, de viscosité et de plasticité. *C. R. Acad. Sci.*, 271:608–611.
- Nguyen, G. D. and Einav, I. (2009). The energetics of catclasis based on breakage mechanics. *Pure and Applied Geophysics*, 166(10–11):1693–1724.
- Nova, R. (1992). Mathematical modelling of natural and engineered geomaterials. *European J. of Mechanics, A/Solids*, 11(special issue):135–154.
- Nova, R., Castellanza, R., and Tamagnini, C. (2003). A constitutive model for bonded geomaterials subject to mechanical and/or chemical degradation. *Int. J. Num. Anal. Meth. Geomech.*, 27(9):705–732.
- Ogden, R. (1984). *Nonlinear Elastic Deformations*. Ellis Horwood, Chichester.
- Potts, D., Jones, M., and Berget, O. (1988). Subsidence above the ekofisk oil reservoirs. In *Proceedings of the International Congress on behaviour of offshore structures*, pages 113–128, Trondheim, Norway.
- Puzrin, A. M. and Houlsby, G. T. (2001). Fundamentals of kinematic hardening hyperplasticity. *International journal of solids and structures*, 38(21):3771–3794.
- Reddy, B. and Martin, J. (1993). Internal variable formulations of problems in elastoplasticity: constitutive and algorithmic aspects. *Appl. Mech. Reviews*, 47:429–456.
- Rouainia, M. and Wood, D. M. (2000). A kinematic hardening constitutive model for natural clays with loss of structure. *Géotechnique*, 50(2):153–164.
- Rubin, M. B. and Einav, I. (2011). A large deformation breakage model of granular materials including porosity and inelastic distortional deformation rate. *International Journal of Engineering Science*, 49(10):1151–1169.
- Sanavia, L., Schrefler, B. A., and Steinmann, P. (2002). A formulation for an unsaturated porous medium undergoing large inelastic strains. *Computational Mechanics*, 28(2):137–151.
- Simo, J. (1998). Numerical analysis and simulation of plasticity. *Handbook of numerical analysis*, 6:183–499.
- Simo, J. C. (1992). Algorithms for static and dynamic multiplicative plasticity that preserve the classical return mapping schemes of the infinitesimal theory. *Comp. Meth. Appl. Mech. Engng.*, 99(1):61–112.
- Simo, J. C. and Hughes, T. J. R. (1998). *Computational inelasticity*, volume 7. Springer Science & Business Media.
- Simpson, D. G. (2009). M66INV: Fortran 90 subroutine to compute the inverse of a 6×6 matrix. NASA Goddard Space Flight Center.
- Tamagnini, C., Castellanza, R., and Nova, R. (2002). A Generalized Backward Euler algorithm for the numerical integration of an isotropic hardening elastoplastic model for mechanical and chemical degradation of bonded geomaterials. *Int. J. Num. Anal. Meth. Geomech.*, 26:963–1004.
- Tamagnini, C. and Ciantia, M. O. (2016). Plasticity with generalized hardening: constitutive modeling and computational aspects. *Acta Geotechnica*, 11(3):595–623.
- Tengattini, A. (2015). *A micro-mechanical study of cemented granular materials*. PhD thesis, University of Sydney.
- Tengattini, A., Das, A., and Einav, I. (2016). A constitutive modelling framework predicting critical state in sand undergoing crushing and dilation. *Géotechnique*, 66(9):695–710.
- Tengattini, A., Das, A., Nguyen, G. D., Viggiani, G., Hall, S. A., and Einav, I. (2014). A thermomechanical constitutive model for cemented granular materials with quantifiable internal variables. Part I: Theory. *Journal of the Mechanics and Physics of Solids*, 70:281–296.
- Uriel, S. and Serrano, A. (1975). Geotechnical properties of two collapsible volcanic soils of low bulk density at the site of two dams in canary islands (spain). In *Proc. VIII Conf. on Soil Mech. Found. Engng.*, volume 2, pages 257–264, Moscow, USSR.
- Viggiani, G. and Hall, S. A. (2012). Full-field measurements in experimental geomechanics: historical perspective, current trends and recent results. In Viggiani, G., Hall, S. A., and Romero, E., editors, *Advanced experimental techniques in geomechanics*, pages 3–67. ALERT Geomaterials.
- Ziegler, H. (1983). *An introduction to thermomechanics*. North Holland.
- Ziegler, H. and Wehrli, C. (1987). The derivation of constitutive relations from the free energy and the dissipation function. *Advances in applied mechanics*, page 183.

Appendix A. Spectral representation of Kirchhoff stress

Due to assumptions (55a),(55b) and the definition of principal elastic logarithmic strain (54), the derivative of the free energy function with respect to \mathbf{b}^e takes the following form:

$$\frac{\partial \psi}{\partial \mathbf{b}^e} = \sum_{A=1}^3 \frac{\partial \psi}{\partial \varepsilon_A^e} \frac{\partial \varepsilon_A^e}{\partial b_A^e} \frac{\partial b_A^e}{\partial \mathbf{b}^e} = \sum_{A=1}^3 \frac{1}{2b_A^e} \frac{\partial \psi}{\partial \varepsilon_A^e} \mathbf{n}^{(A)} \otimes \mathbf{n}^{(A)} \quad (123)$$

since:

$$\varepsilon_A^e = \frac{1}{2} \ln(b_A^e) \quad \text{and} \quad \frac{\partial b_A^e}{\partial \mathbf{b}^e} = \mathbf{n}^{(A)} \otimes \mathbf{n}^{(A)}$$

in which $\mathbf{n}^{(A)}$ is the A -th unit eigenvector of \mathbf{b}^e , see, e.g., [Simo, 1998, Ch. 33].

As \mathbf{b}^e and $\partial \psi / \partial \mathbf{b}^e$ are coaxial, the quantity on the RHS of eq. (41) admits the following spectral representation:

$$2 \frac{\partial \psi}{\partial \mathbf{b}^e} \mathbf{b}^e = \sum_{A=1}^3 \frac{\partial \psi}{\partial \varepsilon_A^e} \mathbf{n}^{(A)} \otimes \mathbf{n}^{(A)} \quad (124)$$

comparing this result with the spectral decomposition of Kirchhoff stress:

$$\boldsymbol{\tau} = \sum_{A=1}^3 \tau_A \mathbf{n}_\tau^{(A)} \otimes \mathbf{n}_\tau^{(A)}$$

where $\mathbf{n}_\tau^{(A)}$ ($A = 1, 2, 3$) are the unit eigenvectors of $\boldsymbol{\tau}$, from the hyperelastic constitutive equation (41) we deduce that:

$$\mathbf{n}_\tau^{(A)} = \mathbf{n}^{(A)} \quad \tau_A = \frac{\partial \psi}{\partial \varepsilon_A^e} \quad (A = 1, 2, 3) \quad (125)$$

Appendix B. Yield surface and dilatancy in Kirchhoff stress invariants space

Taking into account the elastic constitutive equation (62), the generalized stresses $\bar{\chi}_B$ and $\bar{\chi}_D$ can be expressed as functions of (p, q, B, D) as follows:

$$\bar{\chi}_B = \xi_B p^2 + \eta_B q^2 \quad \bar{\chi}_D = \xi_D p^2 + \eta_D q^2 \quad (126)$$

where:

$$\xi_B(B, D) := \frac{n_g \theta_g}{2} \frac{K^g}{(\bar{K}^{gb})^2} \quad \xi_D(B, D) := \frac{n_b}{2} \frac{K^b}{(\bar{K}^{gb})^2} \quad (127a)$$

$$\eta_B(B, D) := \frac{n_g \theta_g}{6} \frac{G^g}{(\bar{G}^{gb})^2} \quad \eta_D(B, D) := \frac{n_b}{6} \frac{G^b}{(\bar{G}^{gb})^2} \quad (127b)$$

Setting:

$$f_{Bs}(B) := \frac{(1-B)^2 \sin^2 \omega_B}{E_{BC}} \quad (128a)$$

$$f_{Bc}(B) := \frac{(1-B)^2 \cos^2 \omega_B}{E_{BC}} \quad (128b)$$

$$f_D(D) := \frac{(1-D)^2}{E_{DC}} \quad (128c)$$

and taking into account eqs. (127), eq. (84) provides the yield surface in Kirchhoff stress invariants space:

$$y^* = q^2 \Xi_1(p, B, D) - M^2 (p^*)^2 \Xi_2(p, B, D) = 0 \quad (129)$$

in which $p^* := p + p_t(1-D)$, and:

$$\Xi_1 := 1 + M^2 (p^*)^2 \left\{ f_{Bs} \eta_B \left(\frac{p}{p + p_t} \right)^2 + f_{Bc} \eta_B + f_D \eta_D \right\} \quad (130a)$$

$$\Xi_2 := 1 - p^2 \left\{ f_{Bs} \xi_B \left(\frac{p}{p + p_t} \right)^2 + f_{Bc} \xi_B + f_D \xi_D \right\} \quad (130b)$$

From eq. (129) it is possible to express the deviatoric stress at yield as a function of the mean effective stress p and the internal variables B and D :

$$q = M p^* \sqrt{\frac{\Xi_2}{\Xi_1}} \quad (131)$$

Note that this relation holds only as long as the scalar function Ξ_2 is non-negative, a situation which, depending on the choice made for the material constants, may occur at very low values of B and D in the tensile mean stress range, as p approaches the limiting value $-p_t(1-D)$.

In the low mean stress range, the yield surface is approximately linear, with an intercept on the q axis (apparent cohesion intercept c_{app}) given by:

$$c_{app} := q(B, D)|_{p=0} = M p_t (1-D) \sqrt{\frac{1}{1 + \mu^2}} \quad (132)$$

where:

$$\mu^2 = M^2 p_t^2 (1-D)^2 (f_{Bc} \eta_B + f_D \eta_D)$$

When $D = 0$ (fully bonded material), $\mu^2 = 0$ and $c = M p_t$. For relatively low values of D , the quantity μ^2 is generally negligible with respect to 1 and $c \approx M p_t (1-D)$. Thus, the apparent cohesion decreases almost linearly with increasing D .

The slope of the yield surface at $p = 0$ is given by:

$$M_{app} := \left. \frac{\partial q}{\partial p} \right|_{p=0} = M \left(\frac{1}{1 + \mu^2} \right)^{3/2} \quad (133)$$

which is equal to M when $D = 0$ and not too different from M as long as μ^2 remains negligible respect to 1. The yield surface in the region of small p values can be replaced by the apparent Drucker–Prager cone of equation:

$$q = c_{app} + M_{app} p \quad (134)$$

which intersects the p axis at $p = -p_{t,app} = -p_t(1-D)(1 + \mu^2)$.

The expressions of the volumetric and deviatoric invariants of the logarithmic plastic strain rate are obtained from eqs. (81) and (83) as:

$$d_v^p = \dot{\gamma} Q_v^* \quad \text{with:} \quad Q_v^* = \text{tr}(\mathbf{Q}_\tau^*) = \frac{2p}{(p + p_t)^2} f_{Bs} (\xi_B p^2 + \eta_B q^2) \quad (135a)$$

$$d_s^p = \dot{\gamma} Q_s^* \quad \text{with:} \quad Q_s^* = \sqrt{\frac{2}{3}} \|\text{dev}(\mathbf{Q}_\tau^*)\| = \frac{2q}{M^2 (p^*)^2} \quad (135b)$$

In the above equations, the expressions (126) have been used for $\bar{\chi}_B$ and $\bar{\chi}_D$. The dilatancy can then be determined as a function of the current stress, breakage and bond damage as:

$$\mathfrak{D} := -\frac{d_v^p}{d_s^p} = -M^2 \left(\frac{p}{q} \right) \left(\frac{p^*}{p + p_t} \right)^2 f_{Bs} (\xi_B p^2 + \eta_B q^2) \quad (136)$$

In the expression on the RHS, the functions of the state variables B and D are all positive. Therefore, the sign of \mathfrak{D} is provided by the mean stress p appearing in the first fraction. The material contracts ($\mathfrak{D} < 0$) when $p > 0$ and dilates ($\mathfrak{D} > 0$) otherwise, with a critical state line ($\mathfrak{D} = 0$) coinciding with the q axis.

Appendix C. Iterative solution of the plastic corrector problem

C.1. Newton's method

The governing equations of the plastic corrector problem can be recast in the following format:

$$\mathbf{R}_{n+1}(\mathbf{x}_{n+1}) = 0 \quad (137)$$

where:

$$\mathbf{x}_{n+1} = \begin{Bmatrix} \hat{\boldsymbol{\varepsilon}}_{n+1}^e \\ B_{n+1} \\ D_{n+1} \\ \Delta\gamma_{n+1} \end{Bmatrix} \quad \mathbf{R}_{n+1} = \begin{Bmatrix} r_{n+1}^e \\ r_{n+1}^B \\ r_{n+1}^D \\ r_{n+1}^y \end{Bmatrix} \quad (138)$$

\mathbf{x}_{n+1} is a vector collecting all the unknowns of the problem and \mathbf{R}_{n+1} is the residual vector, defined as:

$$\mathbf{r}_{n+1}^e = -\hat{\boldsymbol{\varepsilon}}_{n+1}^e + \hat{\boldsymbol{\varepsilon}}_{n+1}^{e, \text{tr}} - \Delta\gamma_{n+1} \hat{\mathbf{Q}}^*(\hat{\boldsymbol{\varepsilon}}_{n+1}^e, B_{n+1}, D_{n+1}) \quad (139a)$$

$$r_{n+1}^B = -B_{n+1} + B_{n+1}^{\text{tr}} + \Delta\gamma_{n+1} Q_B^*(\hat{\boldsymbol{\varepsilon}}_{n+1}^e, B_{n+1}, D_{n+1}) \quad (139b)$$

$$r_{n+1}^D = -D_{n+1} + D_{n+1}^{\text{tr}} + \Delta\gamma_{n+1} Q_D^*(\hat{\boldsymbol{\varepsilon}}_{n+1}^e, B_{n+1}, D_{n+1}) \quad (139c)$$

$$r_{n+1}^y = -\hat{y}^*(\hat{\boldsymbol{\varepsilon}}_{n+1}^e, B_{n+1}, D_{n+1}) \quad (139d)$$

Using Newton's method, the solution is obtained with the following iterative procedure:

(1) Initialization:

$$\mathbf{x}_{n+1}^{(0)} = \mathbf{x}_{n+1}^{e, \text{tr}} \quad \mathbf{x}_{n+1}^{e, \text{tr}} := \{\hat{\boldsymbol{\varepsilon}}_{n+1}^{e, \text{tr}}, B_n, D_n, 0\}^T \quad (140)$$

(2) At the iteration (k), with $k \geq 1$, compute the variation of \mathbf{x}_{n+1} by linearization of eq. (137):

$$\delta \mathbf{x}_{n+1}^{(k)} = -\left\{ \mathbf{J}_{n+1}^{(k)} \right\}^{-1} \mathbf{R}_{n+1}^{(k)} \quad (141)$$

where $\mathbf{J}_{n+1}^{(k)}$ is the (6×6) Jacobian matrix defined as:

$$\mathbf{J}_{n+1}^{(k)} = \left(\frac{\partial \mathbf{R}}{\partial \mathbf{x}} \right)_{n+1}^{(k)} = \begin{bmatrix} \mathbf{A} & \mathbf{U} \\ \mathbf{V} & \mathbf{0} \end{bmatrix}_{n+1}^{(k)} \quad (142)$$

and:

$$\mathbf{A}_{n+1}^{(k)} := \begin{bmatrix} \partial r^e / \partial \hat{\boldsymbol{\varepsilon}}^e & \partial r^e / \partial B & \partial r^e / \partial D \\ \partial r^B / \partial \hat{\boldsymbol{\varepsilon}}^e & \partial r^B / \partial B & \partial r^B / \partial D \\ \partial r^D / \partial \hat{\boldsymbol{\varepsilon}}^e & \partial r^D / \partial B & \partial r^D / \partial D \end{bmatrix}_{n+1}^{(k)}$$

$$\mathbf{U}_{n+1}^{(k)} := \begin{Bmatrix} \partial r^e / \partial \Delta\gamma \\ \partial r^B / \partial \Delta\gamma \\ \partial r^D / \partial \Delta\gamma \end{Bmatrix}_{n+1}^{(k)} \quad \left(\mathbf{V}_{n+1}^{(k)} \right)^T := \begin{Bmatrix} \partial r^y / \partial \hat{\boldsymbol{\varepsilon}}^e \\ \partial r^y / \partial B \\ \partial r^y / \partial D \end{Bmatrix}_{n+1}^{(k)}$$

(3) Update of the solution vector and of residual vector:

$$\mathbf{x}_{n+1}^{(k+1)} = \mathbf{x}_{n+1}^{(k)} + \delta \mathbf{x}_{n+1}^{(k)} \quad \mathbf{R}_{n+1}^{(k+1)} = \mathbf{R}(\mathbf{x}_{n+1}^{(k+1)}) \quad (143)$$

(4) Check for convergence: if

$$\left(\left\| \mathbf{r}_{n+1}^{e, (k+1)} \right\| < \text{TOL}_e \right) \quad \& \quad \left(\left| r_{n+1}^{B, (k+1)} \right| < \text{TOL}_B \right) \\ \& \quad \left(\left| r_{n+1}^{D, (k+1)} \right| < \text{TOL}_D \right) \quad \& \quad \left(\left| r_{n+1}^{y, (k+1)} \right| < \text{TOL}_y \right)$$

then:

$$\mathbf{x}_{n+1} = \mathbf{x}_{n+1}^{(k+1)} \quad \text{then exit.}$$

else:

$$\mathbf{x}_{n+1}^{(k)} \leftarrow \mathbf{x}_{n+1}^{(k+1)} \quad \text{then go to step (2).}$$

In step (2), the inverse of the Jacobian matrix is computed in closed form, using the Fortran 90 library `m66inv` by Simpson [2009]. An alternative possibility is to exploit the zero diagonal term in the (6,6) component and reduce the problem dimension by 1 via static condensation. The expressions of the various components of matrix $\mathbf{A}_{n+1}^{(k)}$ and vectors $\mathbf{U}_{n+1}^{(k)}$ and $\mathbf{V}_{n+1}^{(k)}$ for the model described in Sect. 4 are provided in Sects. C.2–C.4. To ease the notation, the superscript (k) and the subscript ($n+1$) are omitted; in addition, the following scalar quantities are introduced to make more compact the algebraic expressions of the components of $\mathbf{A}_{n+1}^{(k)}$, $\mathbf{U}_{n+1}^{(k)}$ and $\mathbf{V}_{n+1}^{(k)}$:

$$\begin{aligned} \bar{p} &:= p + p_t & p^* &:= p + p_t(1-D) \\ C_1 &:= \frac{2(1-B)^2 \sin^2 \omega_B}{3 E_{BC}} & C_2 &:= \frac{6}{M^2 (p^*)^2} \\ C_3 &:= \frac{4(1-B) \sin^2 \omega_B}{3 E_{BC}} & C_4 &:= \frac{(1-B)^2 \cos^2 \omega_B}{E_{BC}} \\ C_5 &:= \frac{(1-D)^2}{E_{DC}} & C_6 &:= \frac{2(1-B) \cos^2 \omega_B}{E_{BC}} \\ C_7 &:= \frac{2(1-D)}{E_{DC}} \end{aligned}$$

C.2. Components of (5×5) matrix \mathbf{A}

Matrix \mathbf{A} can be considered composed of 9 sub-matrices which represent the derivatives of the 3 residuals r^e , r^B and r^D with respect to the unknowns $\hat{\boldsymbol{\varepsilon}}^e$, B and D . Each of these sub-matrices is provided in the following.

Matrix \mathbf{A}_{11}

From eqs. (139) and (83a), we have:

$$\mathbf{A}_{11} := \frac{\partial \mathbf{r}^e}{\partial \hat{\boldsymbol{\varepsilon}}^e} = -\mathbf{I}_3 - \Delta\gamma \frac{\partial \hat{\mathbf{Q}}^*}{\partial \hat{\boldsymbol{\varepsilon}}^e} \quad (144)$$

where, from eq. (83a):

$$\begin{aligned} \frac{\partial \hat{\mathbf{Q}}^*}{\partial \hat{\boldsymbol{\varepsilon}}^e} &= \frac{C_1}{\bar{p}^2} \left\{ n_g \theta^g p (K^g \varepsilon_v^e) + \bar{\chi}_B \bar{K}^{gb} \left(1 - \frac{2p}{\bar{p}} \right) \right\} \boldsymbol{\delta} \otimes \boldsymbol{\delta} \\ &+ \left(2C_1 n_g \theta^g G^g \frac{p}{\bar{p}^2} \right) \boldsymbol{\delta} \otimes \hat{\boldsymbol{\varepsilon}}^e \\ &- \left(2C_2 \frac{\bar{G}^{gb} \bar{K}^{gb}}{p^*} \right) \hat{\boldsymbol{\varepsilon}}^e \otimes \boldsymbol{\delta} + C_2 \bar{G}^{gb} \mathbf{I}_3^{\text{dev}} \end{aligned} \quad (145)$$

and

$$\mathbf{I}_3^{\text{dev}} := \mathbf{I}_3 - \frac{1}{3} \boldsymbol{\delta} \otimes \boldsymbol{\delta}$$

Column vector \mathbf{A}_{12}

From eqs. (139) and (83a), we have:

$$\mathbf{A}_{12} := \frac{\partial \mathbf{r}^e}{\partial B} = -\Delta\gamma \frac{\partial \hat{\mathbf{Q}}^*}{\partial B} \quad (146)$$

where, from eq. (83a):

$$\frac{\partial \hat{Q}^*}{\partial B} = -\frac{\bar{\chi}_B}{\bar{p}^2} \left\{ C_3 p + C_1 n_g \theta^g (K^g \varepsilon_v^e) \left(1 - \frac{2p}{\bar{p}} \right) \right\} \delta + C_2 n_g \theta^g \left\{ \frac{2K^g \varepsilon_v^e}{p^*} \bar{G}^{gb} - G^g \right\} \hat{e}^e \quad (147)$$

Column vector A_{13}

From eqs. (139) and (83a), we have:

$$A_{13} := \frac{\partial r^e}{\partial D} = -\Delta\gamma \frac{\partial \hat{Q}^*}{\partial D} \quad (148)$$

where, from eq. (83a):

$$\frac{\partial \hat{Q}^*}{\partial D} = -\frac{\bar{\chi}_B}{\bar{p}^2} \left\{ C_1 n_b (K^b \varepsilon_v^e) \left(1 - \frac{2p}{\bar{p}} \right) \right\} \delta + C_2 \left\{ \frac{2(n_b K^b \varepsilon_v^e + p_t)}{p^*} \bar{G}^{gb} - n_b G^b \right\} \hat{e}^e \quad (149)$$

Row vector A_{21}

As the scalar function Q_B^* provided by eq. (83b) is independent of \hat{e}^e , we have:

$$A_{21} := \left(\frac{\partial r^B}{\partial \hat{e}^e} \right)^T = 0_{(1 \times 3)} \quad (150)$$

Scalar A_{22}

From eqs. (139) and (83b), we have:

$$A_{22} := \frac{\partial r^B}{\partial B} = -1 + \Delta\gamma \frac{\partial Q_B^*}{\partial B} = -1 - 2\Delta\gamma C_6 \quad (151)$$

Scalar A_{23}

As the scalar function Q_B^* provided by eq. (83b) is independent of D , we have:

$$A_{23} := \frac{\partial r^B}{\partial D} = 0 \quad (152)$$

Row vector A_{31}

As the scalar function Q_D^* provided by eq. (83c) is independent of \hat{e}^e , we have:

$$A_{31} := \left(\frac{\partial r^D}{\partial \hat{e}^e} \right)^T = 0_{(1 \times 3)} \quad (153)$$

Scalar A_{32}

As the scalar function Q_D^* provided by eq. (83c) is independent of B , we have:

$$A_{32} := \frac{\partial r^D}{\partial B} = 0 \quad (154)$$

Scalar A_{33}

From eqs. (139) and (83c), we have:

$$A_{33} := \frac{\partial r^D}{\partial D} = -1 + \Delta\gamma \frac{\partial Q_D^*}{\partial D} = -1 - 2\Delta\gamma C_7 \quad (155)$$

C.3. Components of (5×1) column vector U

Column vector U can be considered composed of 3 sub-vectors which represent the derivatives of the 3 residuals r^e , r^B and r^D with respect to the unknown $\Delta\gamma$. From eqs. (139) and (83) we have:

$$U = \begin{Bmatrix} -\hat{Q}^* \\ Q_B^* \\ Q_D^* \end{Bmatrix} = \begin{Bmatrix} -C_1 \bar{\chi}_B (p/\bar{p}^2) \delta - C_2 \bar{G}^{gb} \hat{e}^e \\ 2C_4 \\ 2C_5 \end{Bmatrix} \quad (156)$$

C.4. Components of (1×5) row vector V

Row vector V can be considered composed of 3 sub-vectors which represent the derivatives of the residual r^y with respect to the unknowns \hat{e}^e , B and D . Each of these sub-vectors is provided in the following.

Row vector V_1

From eqs. (139) and (84), we have:

$$V_1 := \left(\frac{\partial r^y}{\partial \hat{e}^e} \right)^T = - \left(\frac{\partial y^*}{\partial \hat{e}^e} \right)^T \quad (157)$$

where:

$$\begin{aligned} \frac{\partial y^*}{\partial \hat{e}^e} = & \left\{ \frac{3p}{2\bar{p}^2} C_1 \left[n_g \theta_g p (K^g \varepsilon_v^e) + 2\bar{\chi}_B \bar{K}^{gb} \left(1 - \frac{p}{\bar{p}} \right) \right] \right. \\ & + \left. \left(C_4 n_g \theta^g K^g + C_5 n_b K^b \right) \varepsilon_v^e - \frac{3C_2}{p^*} \bar{K}^{gb} \left(\bar{G}^{gb} \varepsilon_s^e \right)^2 \right\} \delta \\ & + \left\{ n_g \theta^g G^g \left[3C_1 \left(\frac{p}{\bar{p}} \right)^2 + 2C_4 \right] + 2C_5 n_b G^b \right. \\ & \left. + 2C_2 \left(\bar{G}^{gb} \right)^2 \right\} \hat{e}^e \quad (158) \end{aligned}$$

Scalar V_2

From eqs. (139) and (84), we have:

$$V_2 := \frac{\partial r^y}{\partial B} = -\frac{\partial y^*}{\partial B} \quad (159)$$

where:

$$\begin{aligned} \frac{\partial y^*}{\partial B} = & -3\bar{\chi}_B \frac{p}{\bar{p}^2} \left\{ \frac{1}{2} C_3 p + C_1 n_g \theta^g (K^g \varepsilon_v^e) \left(1 - \frac{p}{\bar{p}} \right) \right\} \\ & - C_6 \bar{\chi}_B - 3C_2 n_g \theta^g \bar{G}^{gb} \left\{ G^g - \frac{(K^g \varepsilon_v^e)}{p^*} \bar{G}^{gb} \right\} (\varepsilon_s^e)^2 \quad (160) \end{aligned}$$

Scalar V_3

From eqs. (139) and (84), we have:

$$V_3 := \frac{\partial r^y}{\partial D} = -\frac{\partial y^*}{\partial D} \quad (161)$$

where:

$$\begin{aligned} \frac{\partial y^*}{\partial D} = & -3\bar{\chi}_B \frac{p}{\bar{p}^2} \left\{ C_1 n_b (K^b \varepsilon_v^e) \left(1 - \frac{p}{\bar{p}} \right) \right\} - C_7 \bar{\chi}_D \\ & - 3C_2 \bar{G}^{gb} \left\{ n_b G^b - \frac{(n_b K^b \varepsilon_v^e + p_t)}{p^*} \bar{G}^{gb} \right\} (\varepsilon_s^e)^2 \quad (162) \end{aligned}$$

Manuscript received 24th May 2020, revised 7th August 2020, accepted 28th September 2020.